esa

Semiconductor Detectors

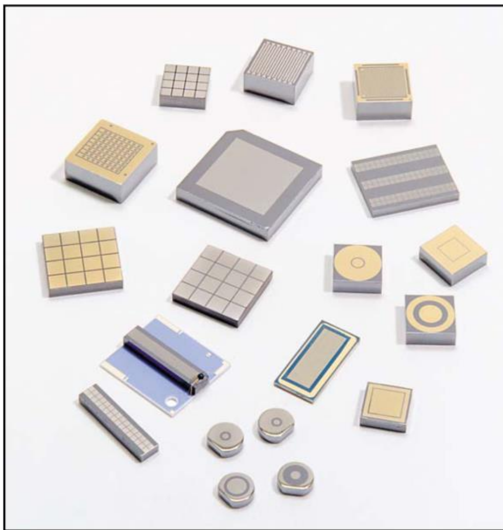

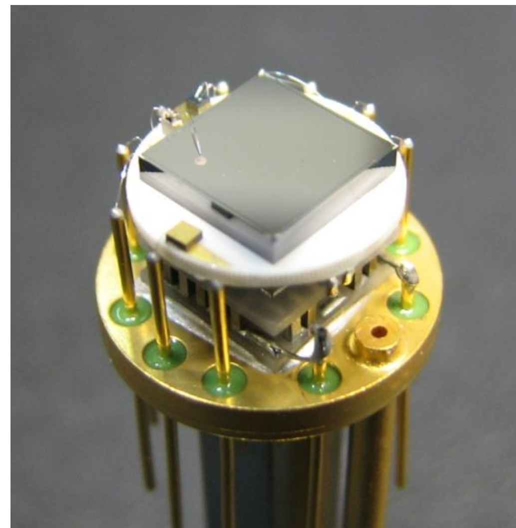

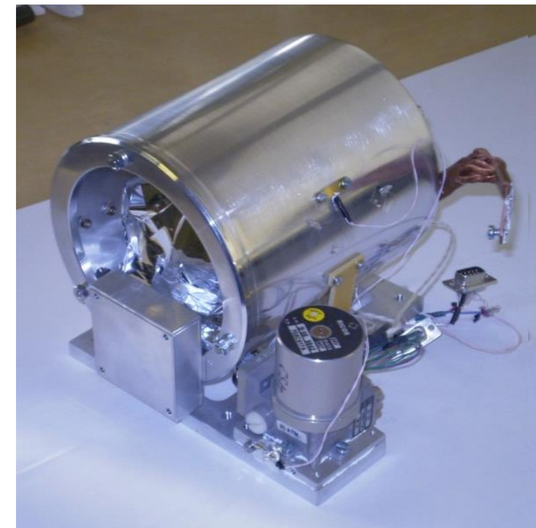

Alan Owens
European Space Agency
Noordwijk, The Netherlands

Outline

- Semiconductors
- Material production and growth
- Detectors fabrication and characterization
- Detection systems
- Performance limitations
- Improving performance
- New detection techniques

esa

Advantages of semiconductors

- Wide variety of compounds available
- Compounds can be selected for specific environments
- Materials can be engineered for specific applications
- Electronics can be integrated – e.g. DEPFET
- Ability to match response and energy resolution to an application
- Wide range of stopping powers
- Can have a wide dynamic range in a single detector

Disadvantages

- Requires hyperpure material - expensive
- Usually requires cooling for best performance
- Difficult to grow in large sizes
- Radiation damage issues

An example - advantages of semiconductors

- Compounds can be selected for specific environments or applications
  e.g., high temperature operation

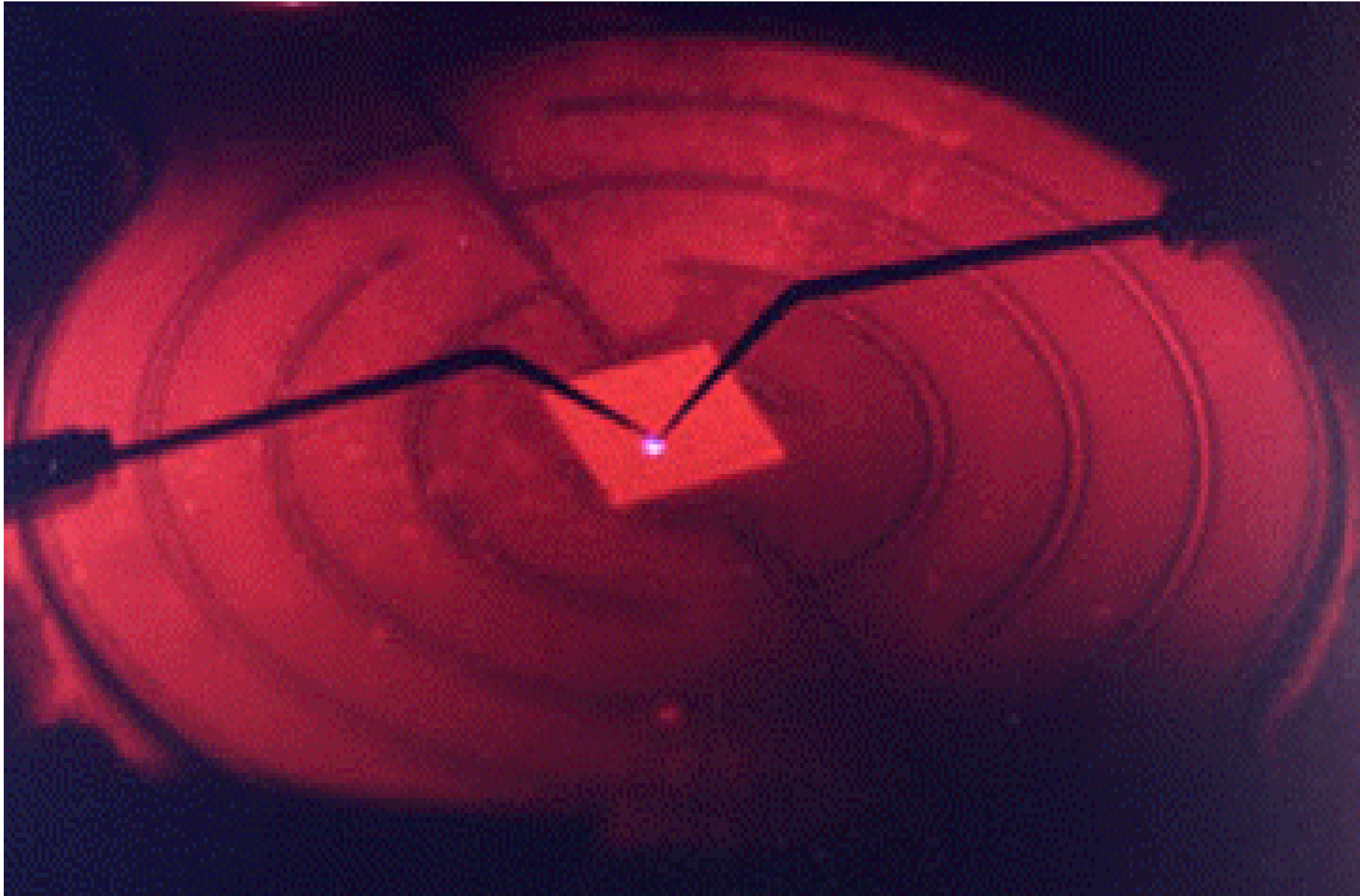

6H-SiC blue LED + front end J-FET operating at 650° C

Image: NASA Glenn Research Center, OH, USA

Energy band formation

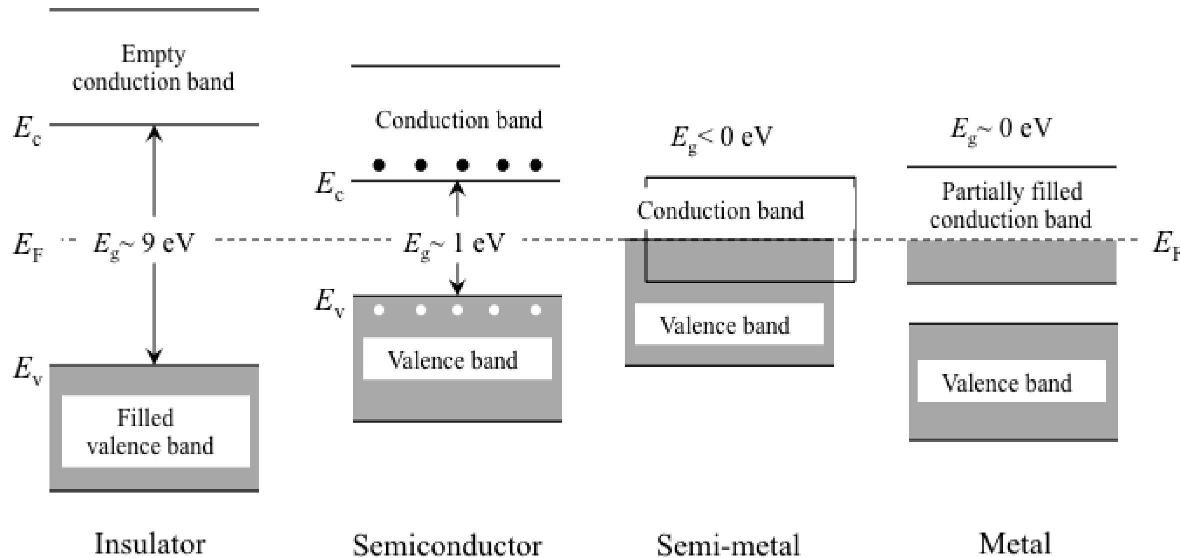

Schematic energy band diagrams for an insulator, a semiconductor and a metal.

Material	E_g(eV)	n (cm^{-3})
Metal	no energy gap	10^{22}
Semimetal	$E_g \leq 0$	10^{17} - 10^{21}
Semiconductor	$0 < E_g < 4$	$< 10^{17}$
Insulator	$E_g \geq 4$	<<1

Classification of materials according to their energy gap, E_g, and carrier density, n, at room temperature. Values are given for pure, that is, intrinsic, materials. We arbitrarily choose a bandgap of 4 eV as the dividing line between insulators and semiconductors, since the actual distinction between the two is somewhat blurred and depends on the temperature in practice, as that determines the number of free carriers in the conduction band.

Energy band formation

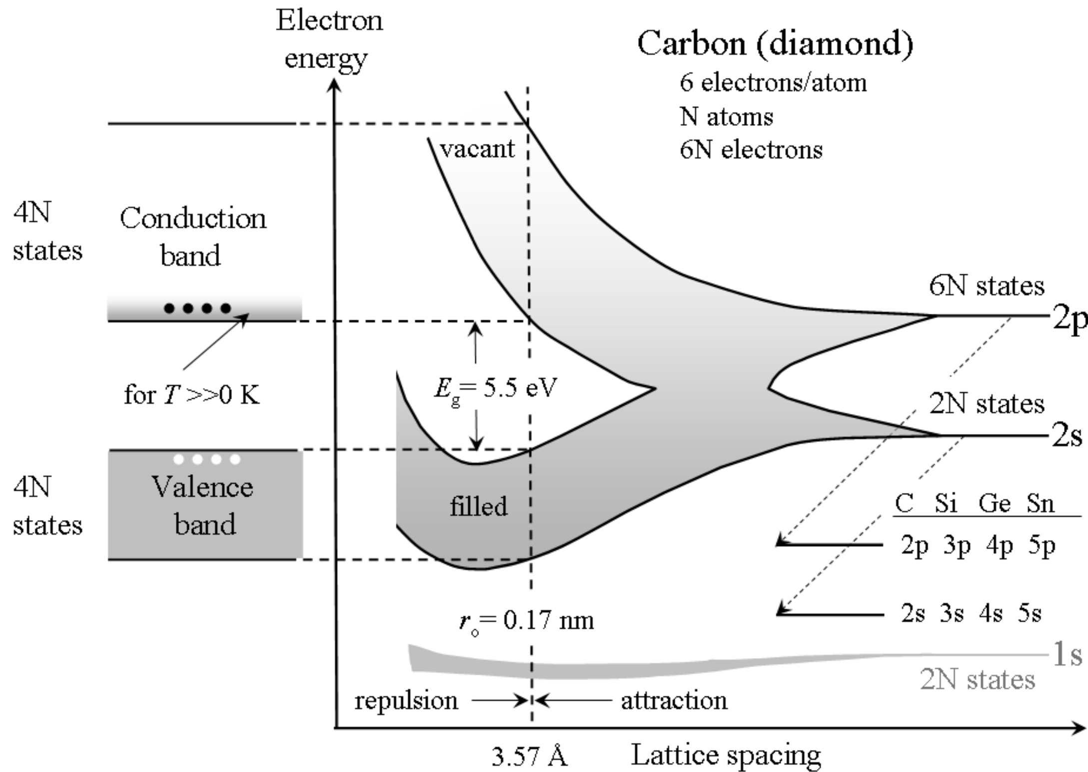

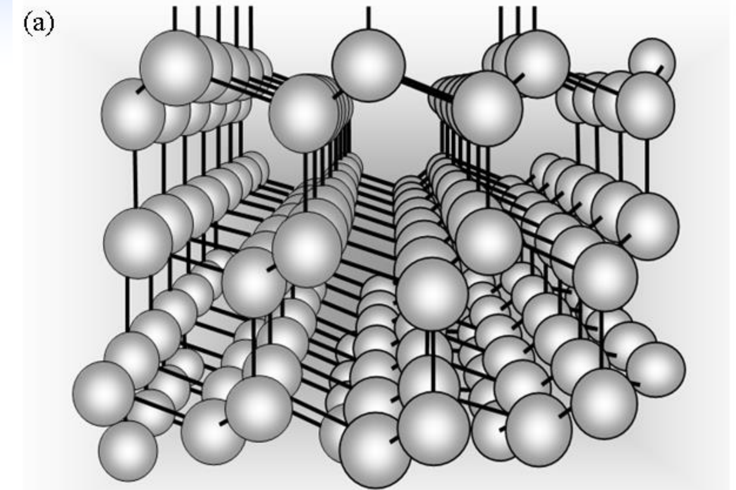

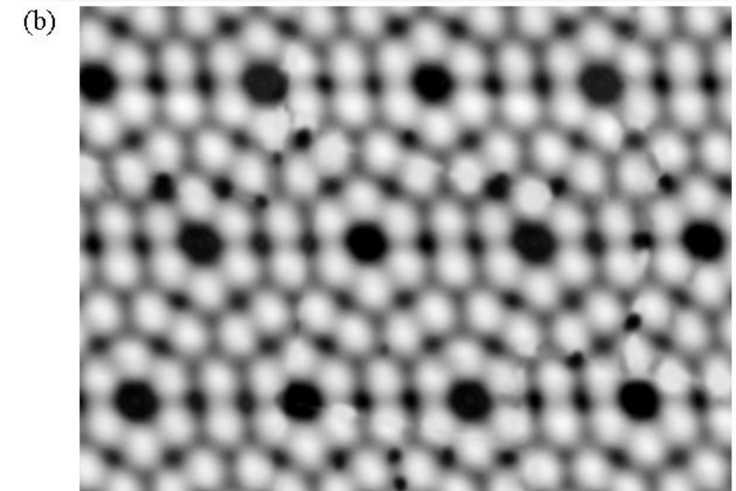

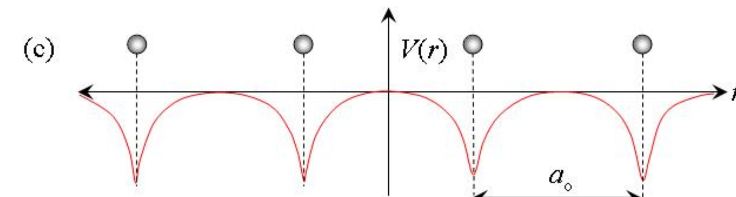

When two atoms approach one another, the electron wave functions begin to overlap and these energy levels split into two, as a consequence of Pauli's exclusion principle. When *N* atoms come together to form a solid, each energy level now splits into *N* separate but closely spaced levels, thereby resulting in a continuous band of energy levels for each quantum number, *n*. As the atoms approach, the discrete *2s* and *2p* levels begin to split, into *N* closely spaced energy levels, where *N* is the number of atoms. As $N \rightarrow \infty$ these levels merge to form a continuous band. As the atoms approach their equilibrium interatomic spacing, this band separates into two, becoming the conduction band and the valence band. At the equilibrium position the total energy of the electrons and the lattice is minimized. The region separating the conduction and valence bands is termed the forbidden gap, or bandgap, and is characterized by a bandgap energy, E_g.

esa

Common crystal structures at the microscopic level

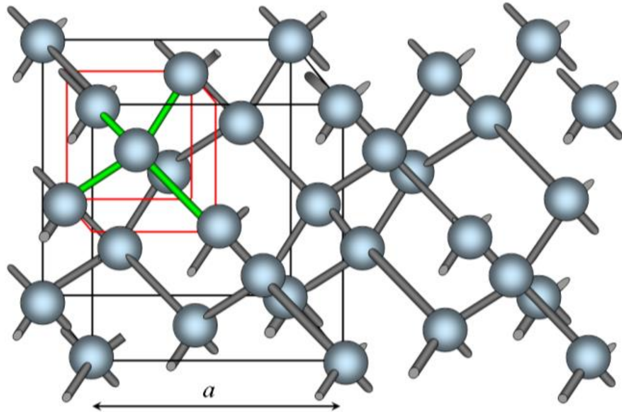

The diamond lattice structure. Each atom has four equidistant, tetrahedrally coordinated, nearest neighbours. The unit cell is outlined by the cube of dimension (lattice parameter), ***a***. Examples: Si, Ge, Diamond.

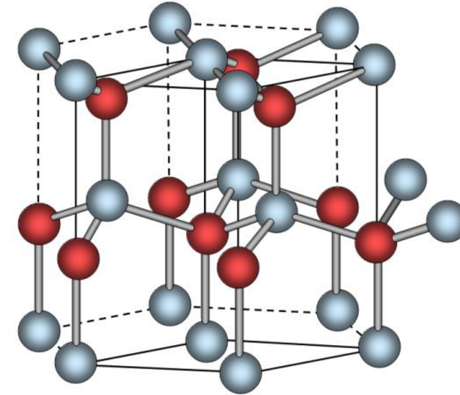

The wurtzite lattice structure which is the second most common structure (~30%) for binary compound semiconductors. Examples: AlN, InN, CdS

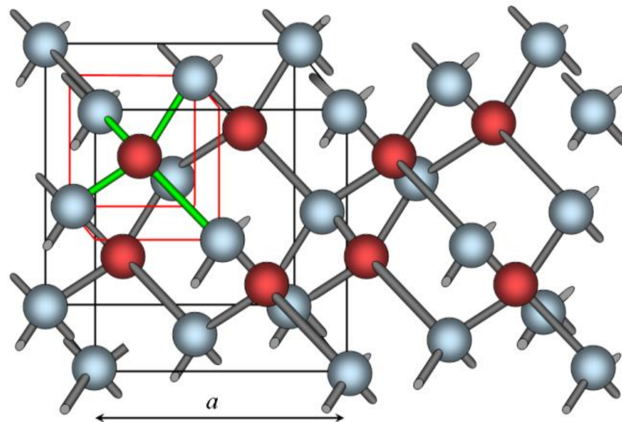

The Zinc-Blende lattice structure which is most common structure for binary compound semiconductors. The unit cell is outlined by the cube of dimension (lattice parameter), ***a***. Examples: GaAs, GaP, InAs, CdTe

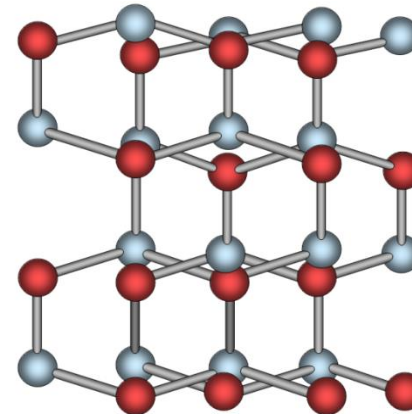

The hexagonal lattice structure.
Examples: SiC, PbI_2

Forming compounds

Follow the Hume-Rothery rules

• The ***atomic radii*** of the different atoms involved must ***differ by less than 15%***

• The components must have the ***same crystal structure***

• The species must have ***similar valences***

• The components must ***have similar electronegativities***

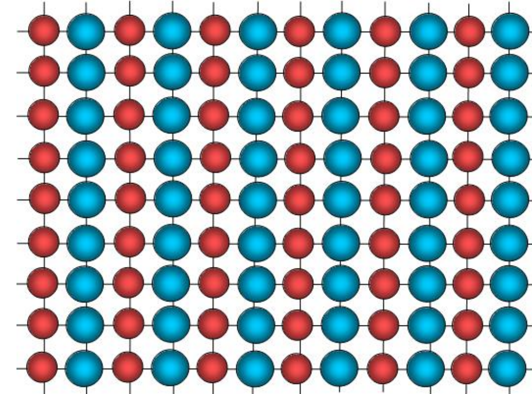

Rational

• Atomic radii must be similar because if substituted atom is too large, considerable strain will develop in crystal lattice

• The components must have similar crystal structure if solubility is to occur over all proportions, e.g., the CdTe-ZnTe system. However, this is less important if small proportions of solute being added - such as in the doping of semiconductors.

• Similar valences and electronegativities indicates that components have similar bonding properties.

W. Hume-Rothery, *The Structure of Metals and Alloys,* The Institute of Metals, London (1969).

Is the compound semiconducting?

Mooser-Pearson laws

Materials will show semiconducting properties if they obey the following rules:

1) The bonds are predominantly covalent.

2) The bonds are formed by a process of electron sharing which leads to completely filled ***s*** and ***p*** sub-shells on all atoms in elemental semiconductors. For compound semiconductors, the condition has to apply for each constituent element.

3) The presence of vacant "metallic" orbital's on some atoms in a compound will not prevent semiconductivity *provided* that these atoms are not bonded together.

4) The bonds form a continuous array in one, two or three dimensions throughout the crystal.

Elements from groups IV to group VII will satisfy conditions 1 and 2. Compounds which follow the second condition can be represented by the following expression †.

$$n_e / n_a + b = 8$$

Here, n_e is the number of valence electrons per molecule, n_a is the number of group IV to VII atoms per molecule and b is the average number of covalent bonds formed by one of these atoms with other atoms of groups IV to VII. Thus, for GaAs, n_e=8, n_a=1 and b=0 – which equals 8.

Bottom line for binaries, the group numbers should add up to 8 – i.e., group I-VII, III-V, IV-IV, II-VI and I-VII

†Equivalent to the 8-N rule

E. Mooser, W.B.Pearson, "*The Chemical Bond in Semiconductors*", J. Electron., Vol.**1** (1956) pp. 629-645

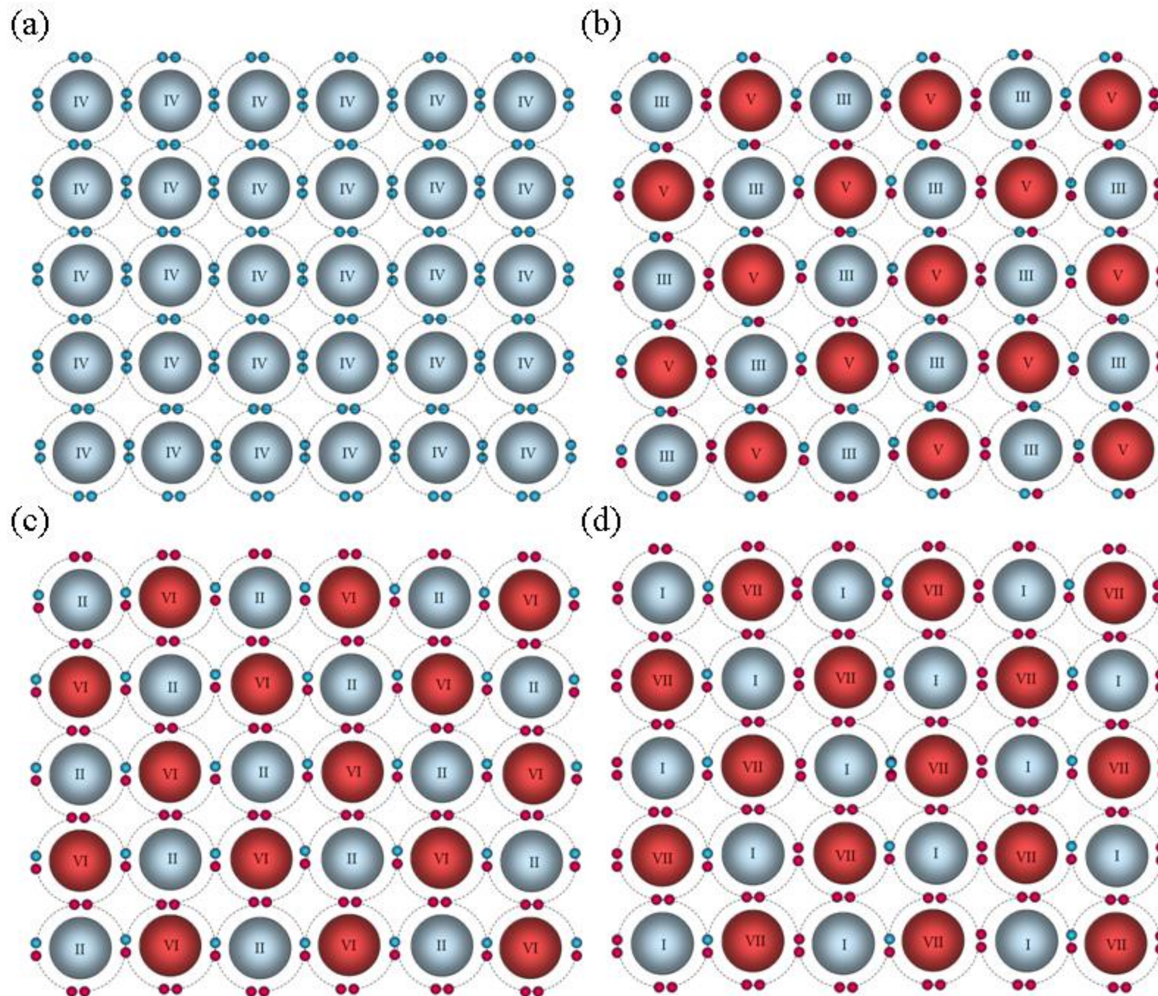

Illustration showing how semiconductors bond to form closed valence shells. Examples are given for the four most common semiconductor groups; (a) group IV elemental semiconductors, such as Si and Ge (b) group III-V semiconductors, such as GaAs and InP, (c) group II-VI compounds, such as ZnS and CdTe, and (d) group I-VII compounds such AgCl and AgBr.

Deriving new semiconductors

Class		Group		Examples
elemental	—	IVB	—	Ge, Si, C
binary	—	IV-IV	—	SiGe, SiC
binary	—	III-V	—	InP, GaAs, GaN
binary	—	II-VI	—	HgTe, CdSe, ZnS
binary	—	I-VII	—	AgCl, AgBr, CuCl
ternary	—	all	—	HgCdTe, AlGaAs
quaternary	—	all	—	InGaAsP, InGaAlP

Group

InSb — AlN (ε_g →, ← λg)

Elemental semiconductors essentially limited to C, Si and Ge

Semiconductors -classification

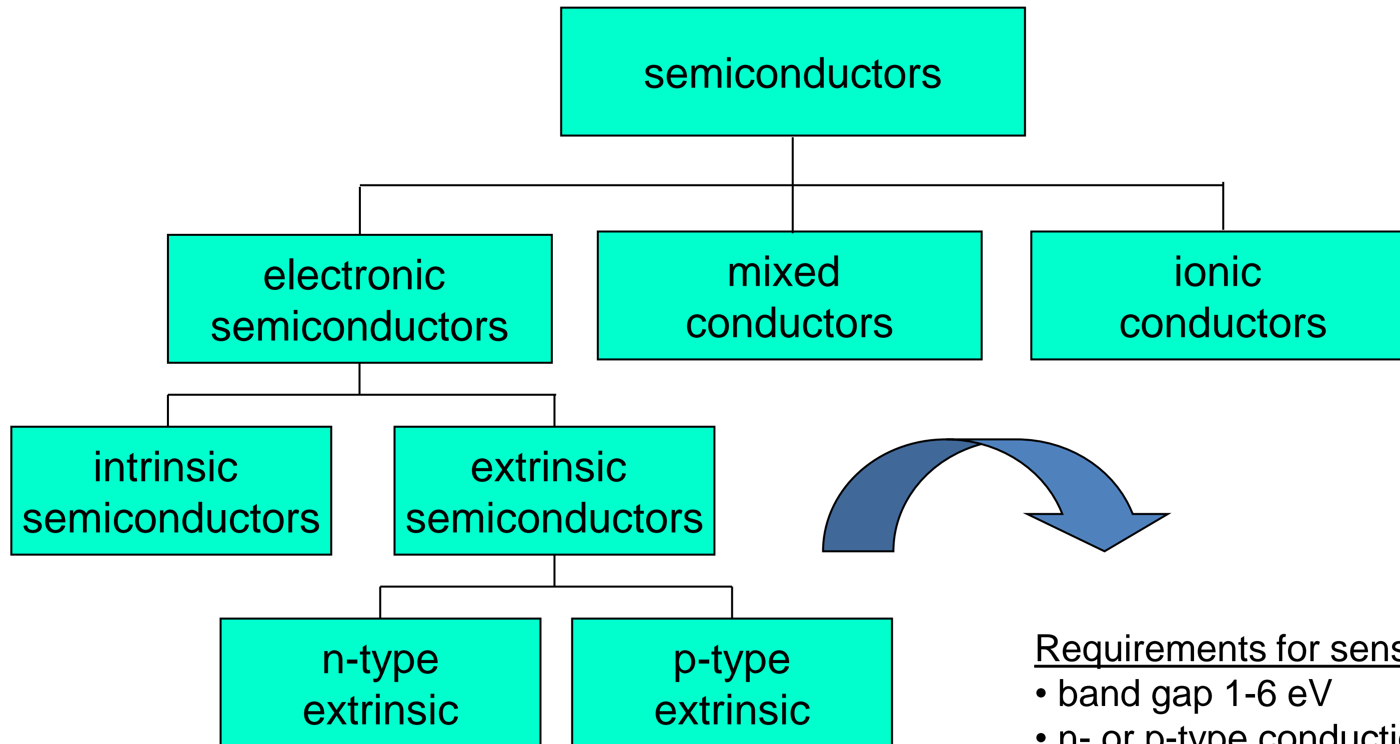

Requirements for sensors:

- band gap 1-6 eV
- n- or p-type conduction
- no ionic conduction
- chemical and thermal stability
- solubility of dopants in host lattice

covalent bonding

esa

Which compounds to choose?

Over three decades ago Armantrout *et al*. (IEEE Trans. Nucl. Sci, NS-24 (1977) 121) produced a rank ordered list of binary materials based on calculated material properties, assuming RT operation, Zmax >50, a photopeak detection efficiency of 2% at 662 keV and an energy resolution of 2% at 662 keV.

Binary	Z_{max}	bandgap	μ_e	μ_h	τ_{min}	
~~AlSb~~	~~51~~	~~1.62~~	~~1200~~	~~700~~	~~1~~	growth - large O_2 affinity, Sb volatility
~~InP~~	~~49~~	~~1.35~~	~~4700~~	~~150~~	~~3~~	no suitable contacting system
~~ZnTe~~	~~52~~	~~2.25~~	~~340~~	~~110~~	~~4~~	trapping and polarization issues
CdTe	52	1.5	1050	80	6	
~~WSe_2~~	~~74~~	~~1.36~~	~~100~~	~~80~~	~~1~~	layered structure
~~CdSe~~	~~48~~	~~1.74~~	~~650~~	~~50~~	~~10~~	polarization, low mobilities
~~BiI_3~~	~~83~~	~~1.7~~	~~680~~	~~20~~	~~5~~	layered structure
~~Ce_3Sb~~	~~55~~	~~1.6~~	~~500~~	~~10~~	~~40~~	stoichiometry issues
HgI_2	89	2.2	94	4	25	

Armantrout: Q *"What can be expected from high-Z semiconductor detectors"*

A "Not much more than we have now?"

Which compounds to choose?

Similarly Abyzon *et al.* (11th Internat. workshop on room temp. seconductor detectors, Vienna 1999) attempted to quantify the approach of Armantrout et al. by assigning a weight to key physical and electronic properties in an attempt to derive a figure of merit. They propose a correlative analysis based on the quantities:

$R\mu_e\tau_e$ and $\rho Z_{eff}^5 / M$

Material	Z_{max}	E_g	μ_e	μ_h	$\mu_e\tau_e$	$\mu_h\tau_h$
CdZnTe	52	2.25	340	110	1×10^{-2}	2×10^{-4}
CdTe	52	1.5	1050	80	3×10^{-3}	2×10^{-4}
HgI_2	89	2.2	94	4	1×10^{-4}	4×10^{-5}
GaAs	33	1.4	4000	700	1×10^{-4}	4×10^{-6}

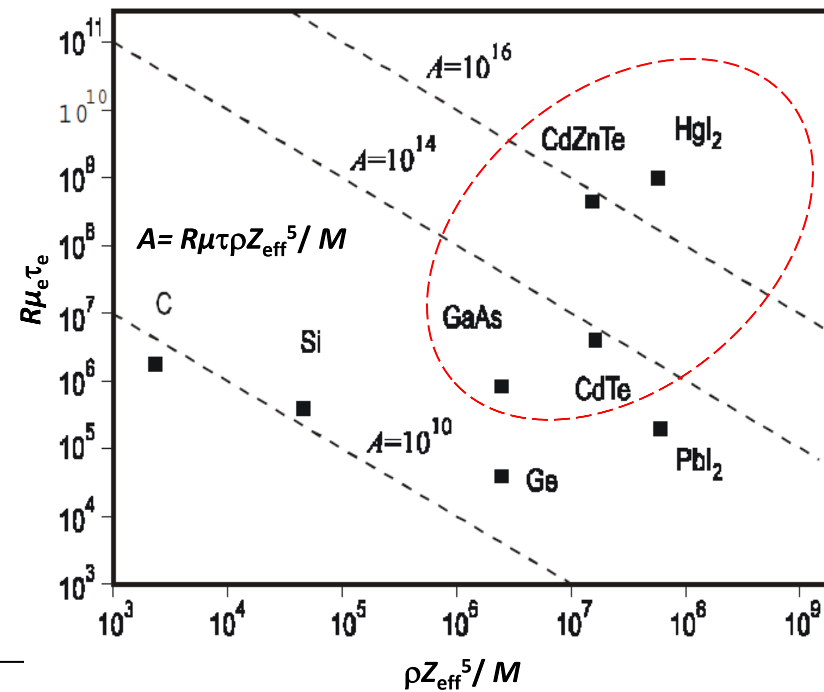

They conclude *"a lack of theoretical and experimental data and discrepancies in existing data do not permit a critical comparison of compounds"*

Group III-V Materials

Physical Properties – Group III-V Materials

Material	Crystal Structure	Pearson symbols/ Space /Point group	Lattice constants a or a, c (nm)	Atomic numbers	Av. Mol. weight	Density (g cm^{-3})	Melting point (K)	Iconicity f_i	KH (kg mm^{-2})
InSb	ZB	cF8, $F\bar{4}3m(T_d^2)$	0.648	49, 51	236.6	4.78	797	0.321	220
InAs	ZB	cF8, $F\bar{4}3m(T_d^2)$	0.606	49, 33	189.7	4.68	1210	0.357	430
InP	ZB	cF8, $F\bar{4}3m(T_d^2)$	0.587	49, 15	145.8	4.79	1335	0.421	460
InN	W	hP4, $P6_3mc(C_{6v}^4)$	0.354, 0.870	49, 7	128.8	6.81	2146	0.578	1140
GaSb	ZB	cF8, $F\bar{4}3m(T_d^2)$	0.610	31, 51	191.5	5.61	991	0.261	450
GaAs	ZB	cF8, $F\bar{4}3m(T_d^2)$	0.564	31, 33	144.6	5.32	1513	0.310	750
GaP	ZB	cF8, $F\bar{4}3m(T_d^2)$	0.545	31, 15	100.7	4.14	1730	0.327	964
β-GaN	ZB	cF8, $F\bar{4}3m(T_d^2)$	0.451	31, 7	83.7	6.15	3246[2]	0.500	1830
α-GaN	W	hP4, $P6_3mc(C_{6v}^4)$	0.319, 0.518	31, 7	83.7	6.07	2791	0.500	1200-1700
BAs	ZB	cF8, $F\bar{4}3m(T_d^2)$	0.478	5, 33	85.7	5.22	2027	0.044	1937
BP	ZB	cF8, $F\bar{4}3m(T_d^2)$	0.4538	5, 15	41.8	2.97	3300	0.032	3263
β-BN	ZB	cF8, $F\bar{4}3m(T_d^2)$	0.362	5, 7	24.8	3.48	3246	0.256	6730-7648
α-BN	H	hP4, $P6_3/mmc(D_{6h})$	0.250, 0.666	5, 7	24.8	3.28	2873[2]	0.221	1489
AlSb	ZB	cF8, $F\bar{4}3m(T_d^2)$	0.614	13, 51	148.7	4.22	1338	0.250	408
AlAs	ZB	cF8, $F\bar{4}3m(T_d^2)$	0.566	13, 33	101.9	3.76	1710	0.274	510
AlP	ZB	cF8, $F\bar{4}3m(T_d^2)$	0.546	13, 15	58.0	2.36	2823	0.307	561
AlN	W	hP4, $P6_3mc(C_{6v}^4)$	0.311, 0.498	13, 7	41.0	3.26	3487	0.449	1020-1427

[1](∥) = parallel to c axis, (⊥) perpendicular to c axis
[2]sublimes/decomposes

Electronic Properties – Group III-V Materials

Material	Type	Bandgap (eV)	Pair Energy (eV)	$\varepsilon_r(0)$[1]	Resistivity (Ω-cm)	Electron Mobility (cm^{2}V^{-1}s^{-1})	Hole Mobility (cm^{2}V^{-1}s^{-1})	$\mu_e\tau_e$ (cm^{2}V^{-1})	$\mu_h\tau_h$ (cm^{2}V^{-1})
InSb	D	0.18	1.2	17.7	~100 @ 4K	80000	1250	7×10^{-5}	
InAs	D	0.354	2.0	15.1	0.03	33000	460		
InP	D	1.34	4.2	12.4	10^{8}	4600	150	2×10^{-5}	1×10^{-5}
InN	D	1.89*		13.1(⊥), 14.4(∥)		3200	<80		
GaSb	D	0.75		15.7	0.04	4000	700	1.4×10^{-5}	
GaAs	D	1.425	4.35	13.1	10^{10}	8500	400	1×10^{-4}	4×10^{-6}
GaP	I	2.27	6.5	11.1	10^{8}-10^{11}	110	75	1.4×10^{-6}	
β-GaN	D	3.23		8.9	10^{6}	760	250		
α-GaN	D	3.42		10.4(⊥), 9.5(∥)	>10^{10}	1500	30		
BAs	I	1.85**		9.9					
BP	I	2.4	6.5	11.0	20	30-120	285-500		
BN (c)	I	6.4		7.1	10^{5}	<200	<500		
BN (h)	I	5.2		7.04(⊥), 5.1(∥)	10^{14}				
AlSb	I	1.62	6.58	14.4	0.04-10^{7}	200	420		
AlAs	I	2.15		10.9	0.2	200	100		
AlP	I	2.42		9.8	1×10^{-5}	60	450		
AlN (h)	D	6.19		8.3(⊥), 8.9(∥)	10^{13}	300	14		

* Early studies showed 1.9-2.05. A recent study claims a value of 0.7-0.8 [33] and is supported by measurement [34].
**Calculated value [35]. Optical absorption measurements suggest a bandgap energy of 0.67 eV [36].

Group II-VI Materials

Physical Properties – Group II-VI Materials

Material	Crystal Structure	Pearson symbols/ Space /Point group	Lattice Constants a or a, c (nm)	Atomic Numbers	Av. Mol. Weight	Density (g cm^{-3})	Melting point (K)	Iconicity f_i	KH (kg mm^{-2})
HgTe	ZB	cF8, $F\bar{4}3m(T_d^2)$	0.646	80, 52	328.2	8.12	943	0.650	23.5-37.7
HgSe	ZB	cF8, $F\bar{4}3m(T_d^2)$	0.609	80, 34	279.6	8.22	1270	0.680	23.5
α-HgS	W	hP6, $P6_3mc(C_{6v}^4)$	0.415, 0.950	80, 16	232.7	8.19	1093	0.790	91
β-HgS	ZB	cF8, $F\bar{4}3m(T_d^2)$	0.585	80, 16	232.7	7.73	857	0.790	138[a]
CdTe	ZB	cF8, $F\bar{4}3m(T_d^2)$	0.648	48, 52	240.0	5.85	1366	0.675	45.9-61.2
CdSe (c)	ZB	cF8, $F\bar{4}3m(T_d^2)$	0.607	48, 34	191.4	5.67	1512	0.699	130
CdSe	W	hP4, $P6_3mc(C_{6v}^4)$	0.430, 0.701	48, 34	191.4	5.81	2023	0.699	91.8
CdS (c)	ZB	cF8, $F\bar{4}3m(T_d^2)$	0.582	48, 16	144.5	4.87	1748	0.685	125
CdS (h)	W	hp4, $P6_3mc(C_{6v}^4)$	0.414, 0.671	48, 16	144.5	4.83	1748	0.685	123-235
ZnTe	ZB	cF8, $F\bar{4}3m(T_d^2)$	0.610	30, 52	193.0	6.34	1568	0.609	61.2-91.8
ZnSe (c)	ZB	cF8, $F\bar{4}3m(T_d^2)$	0.567	30, 34	144.3	5.26	1799	0.630	139.7-186.6
β-ZnS	ZB	cF8, $F\bar{4}3m(T_d^2)$	0.541	30, 16	97.5	4.08	1991[b]	0.623	178
α-ZnS	W	hP4, $P6_3mc(C_{6v}^4)$	0.382, 0.626	30, 16	97.5	4.08	2196	0.623	178
ZnO	ZB	cF8, $F\bar{4}3m(T_d^2)$	0.463	30, 8	81.4	5.68	2248	0.616	5.0 (M[c])
ZnO	W	hP4, $P6_3mc(C_{6v}^4)$	0.3250, 0.5204	30, 8	81.4	5.61	1975[b]	0.616	407.9[d]
β-MgTe	W	hp4, $P6_3mc(C_{6v}^4)$	0.4530, 0.7406	25, 52	151.9	3.81	1360	0.554	143
β-MgSe	NaCl	cF8, $Fm\bar{3}m(O_h^5)$	0.589	12, 34	103.3	4.20	1560	0.790	152
β-MgS	NaCl	cF8, $Fm\bar{3}m(O_h^5)$	0.520	12, 16	56.4	2.86	2783	0.786	3.5 (M[c])[e]

[a]estimated
[b]decomposes/sublimes
[c]Mohs scale
[d]hardest of the II-VI compounds
[e]value given for its mineral form, niningerite

Electronic Properties – Group II-VI Materials

Material	Type	Bandgap (eV)	Pair Energy (eV)	Dielectric Constant $\varepsilon_r(0)$[a]	Resistivity (Ω-cm)	Electron Mobility (cm^{2}V^{-1}s^{-1})	Hole Mobility (cm^{2}V^{-1}s^{-1})	$\mu_e\tau_e$ (cm^{2}V^{-1})	$\mu_h\tau_h$ (cm^{2}V^{-1})
HgTe	SM	-0.14		20.8	10^{-2}-10^{-3}	25000	350		
HgSe	SM	-0.06		25.6		20000	2		
α-HgS	D	2.03		23.5(∥), 18.2(⊥)	3450 (∥), 11080 (⊥)	30(∥), 10(⊥)			
β-HgS	SM	0.54		18.2		250			
CdTe	D	1.48	4.43	10.4	10^{9}	1050	100	3.3×10^{-3}	2×10^{-4}
CdSe (c)	D	1.74	5.5	10.0	10^{5}	800	50	7.2×10^{-4}	7.5×10^{-5}
CdSe (h)	D	1.75	5.5	9.3(⊥), 10.2(∥)	10^{8}	840	75	6×10^{-5}	7.5×10^{-5}
CdS (c)	D	2.42	6.3	5.4		340	50		
CdS (h)	D	2.51	7.8	8.3(⊥), 8.7(∥)	10^{10}	330	48	10^{-7}	
ZnTe	D	2.28	7.0	10.4	10^{10}	340	100	1.4×10^{-6}	7×10^{-5}
ZnSe (c)	D	2.63	8.0	9.2	2×10^{9}	540	28	4×10^{-5}	
β-ZnS (c)	D	3.58	8.2	8.9	10^{10}	165	10		
α-ZnS (w)	D	3.91		8.6(⊥), 8.4(∥)	10^{8}-10^{12}	280(∥), 165(⊥)	100-800		
ZnO (c)	D	3.35	7.5	9.0		200	180		
ZnO (w)	D	3.37		7.8(⊥), 8.8(∥)	10^{9}	250(∥), 280(⊥)	125		
β-MgTe	D	3.49		6.1					
β-MgSe	D	4.05		5.2					
β-MgS	D	4.5 (77K)		4.5					

esa

Group III-V Materials

Physical Properties – Group III-V Materials

Material	Crystal Structure	Pearson symbols/ Space /Point group	Lattice constants *a* or *a, c* (nm)	Atomic numbers	Av. Mol. weight	Density (g cm^{-3})	Melting point (K)	Iconicity f_i	KH (kg mm^{-2})
InSb	ZB	cF8, $F\bar{4}3m(T_d^2)$	0.648	49, 51	236.6	4.78	797	0.321	220
InAs	ZB	cF8, $F\bar{4}3m(T_d^2)$	0.606	49, 33	189.7	4.68	1210	0.357	430
InP	ZB	cF8, $F\bar{4}3m(T_d^2)$	0.587	49, 15	145.8	4.79	1335	0.421	460
InN	W	hP4, $P6_3mc(C_{6v}^4)$	0.354, 0.870	49, 7	128.8	6.81	2146	0.578	1140
GaSb	ZB	cF8, $F\bar{4}3m(T_d^2)$	0.610	31, 51	191.5	5.61	991	0.261	450
GaAs	ZB	cF8, $F\bar{4}3m(T_d^2)$	0.564	31, 33	144.6	5.32	1513	0.310	750
GaP	ZB	cF8, $F\bar{4}3m(T_d^2)$	0.545	31, 15	100.7	4.14	1730	0.327	964
β-GaN	ZB	cF8, $F\bar{4}3m(T_d^2)$	0.451	31, 7	83.7	6.15	3246[2]	0.500	1830
α-GaN	W	hP4, $P6_3mc(C_{6v}^4)$	0.319, 0.518	31, 7	83.7	6.07	2791	0.500	1200-1700
BAs	ZB	cF8, $F\bar{4}3m(T_d^2)$	0.478	5, 33	85.7	5.22	2027	0.044	1937
BP	ZB	cF8, $F\bar{4}3m(T_d^2)$	0.4538	5, 15	41.8	2.97	3300	0.032	3263
β-BN	ZB	cF8, $F\bar{4}3m(T_d^2)$	0.362	5, 7	24.8	3.48	3246	0.256	6730-7648
α-BN	H	hP4, $P6_3/mmc(D_{6h})$	0.250, 0.666	5, 7	24.8	3.28	2873[2]	0.221	1489
AlSb	ZB	cF8, $F\bar{4}3m(T_d^2)$	0.614	13, 51	148.7	4.22	1338	0.250	408
AlAs	ZB	cF8, $F\bar{4}3m(T_d^2)$	0.566	13, 33	101.9	3.76	1710	0.274	510
AlP	ZB	cF8, $F\bar{4}3m(T_d^2)$	0.546	13, 15	58.0	2.36	2823	0.307	561
AlN	W	hP4, $P6_3mc(C_{6v}^4)$	0.311, 0.498	13, 7	41.0	3.26	3487	0.449	1020-1427

[1](∥) = parallel to c axis, (⊥) perpendicular to c axis
[2]sublimes/decomposes

Electronic Properties – Group III-V Materials

Material	Type	Bandgap (eV)	Pair Energy (eV)	$\varepsilon_r(0)$[1]	Resistivity (Ω-cm)	Electron Mobility (cm^{2}V^{-1}s^{-1})	Hole Mobility (cm^{2}V^{-1}s^{-1})	$\mu_e\tau_e$ (cm^{2}V^{-1})	$\mu_h\tau_h$ (cm^{2}V^{-1})
InSb	D	0.18	1.2	17.7	~100 @ 4K	80000	1250	7×10^{-5}	
InAs	D	0.354	2.0	15.1	0.03	33000	460		
InP	D	1.34	4.2	12.4	10^8	4600	150	2×10^{-5}	1×10^{-5}
InN	D	1.89*		13.1(⊥), 14.4(∥)		3200	<80		
GaSb	D	0.75		15.7	0.04	4000	700	1.4×10^{-5}	
GaAs	D	1.425	4.35	13.1	10^{10}	8500	400	1×10^{-4}	4×10^{-6}
GaP	I	2.27	6.5	11.1	10^8-10^{11}	110	75	1.4×10^{-6}	
β-GaN	D	3.23		8.9	10^6	760	250		
α-GaN	D	3.42		10.4(⊥), 9.5(∥)	>10^{10}	1500	30		
BAs	I	1.85**		9.9					
BP	I	2.4	6.5	11.0	20	30-120	285-500		
BN (c)	I	6.4		7.1	10^5	<200	<500		
BN (h)	I	5.2		7.04(⊥), 5.1(∥)	10^{14}				
AlSb	I	1.62	6.58	14.4	0.04-10^7	200	420		
AlAs	I	2.15		10.9	0.2	200	100		
AlP	I	2.42		9.8	1×10^{-5}	60	450		
AlN (h)	D	6.19		8.3(⊥), 8.9(∥)	10^{13}	300	14		

* Early studies showed 1.9-2.05. A recent study claims a value of 0.7-0.8 [33] and is supported by measurement [34].
**Calculated value [35]. Optical absorption measurements suggest a bandgap energy of 0.67 eV [36].

Group II-VI Materials

Physical Properties – Group II-VI Materials

Material	Crystal Structure	Pearson symbols/ Space /Point group	Lattice Constants *a* or *a, c* (nm)	Atomic Numbers	Av. Mol. Weight	Density (g cm^{-3})	Melting point (K)	Iconicity f_i	KH (kg mm^{-2})
HgTe	ZB	cF8, $F\bar{4}3m(T_d^2)$	0.646	80, 52	328.2	8.12	943	0.650	23.5-37.7
HgSe	ZB	cF8, $F\bar{4}3m(T_d^2)$	0.609	80, 34	279.6	8.22	1270	0.680	23.5
α-HgS	W	hP6, $P6_3mc(C_{6v}^4)$	0.415, 0.950	80, 16	232.7	8.19	1093	0.790	91
β-HgS	ZB	cF8, $F\bar{4}3m(T_d^2)$	0.585	80, 16	232.7	7.73	857	0.790	138[a]
CdTe	ZB	cF8, $F\bar{4}3m(T_d^2)$	0.648	48, 52	240.0	5.85	1366	0.675	45.9-61.2
CdSe (c)	ZB	cF8, $F\bar{4}3m(T_d^2)$	0.607	48, 34	191.4	5.67	1512	0.699	130
CdSe	W	hP4, $P6_3mc(C_{6v}^4)$	0.430, 0.701	48, 34	191.4	5.81	2023	0.699	91.8
CdS (c)	ZB	cF8, $F\bar{4}3m(T_d^2)$	0.582	48, 16	144.5	4.87	1748	0.685	125
CdS (h)	W	hp4, $P6_3mc(C_{6v}^4)$	0.414, 0.671	48, 16	144.5	4.83	1748	0.685	123-235
ZnTe	ZB	cF8, $F\bar{4}3m(T_d^2)$	0.610	30, 52	193.0	6.34	1568	0.609	61.2-91.8
ZnSe (c)	ZB	cF8, $F\bar{4}3m(T_d^2)$	0.567	30, 34	144.3	5.26	1799	0.630	139.7-186.6
β-ZnS	ZB	cF8, $F\bar{4}3m(T_d^2)$	0.541	30, 16	97.5	4.08	1991[b]	0.623	178
α-ZnS	W	hP4, $P6_3mc(C_{6v}^4)$	0.382, 0.626	30, 16	97.5	4.08	2196	0.623	178
ZnO	ZB	cF8, $F\bar{4}3m(T_d^2)$	0.463	30, 8	81.4	5.68	2248	0.616	5.0 (M[c])
ZnO	W	hP4, $P6_3mc(C_{6v}^4)$	0.3250, 0.5204	30, 8	81.4	5.61	1975[b]	0.616	407.9[d]
β-MgTe	W	hp4, $P6_3mc(C_{6v}^4)$	0.4530, 0.7406	25, 52	151.9	3.81	1360	0.554	143
β-MgSe	NaCl	cF8, $Fm\bar{3}m(O_h^5)$	0.589	12, 34	103.3	4.20	1560	0.790	152
β-MgS	NaCl	cF8, $Fm\bar{3}m(O_h^5)$	0.520	12, 16	56.4	2.86	2783	0.786	3.5 (M[c])[e]

[a]estimated
[b]decomposes/sublimes
[c]Mohs scale
[d]hardest of the II-VI compounds
[e]value given for its mineral form, niningerite

Electronic Properties – Group II-VI Materials

Material	Type	Bandgap (eV)	Pair Energy (eV)	Dielectric Constant $\varepsilon_r(0)$[a]	Resistivity (Ω-cm)	Electron Mobility (cm^{2}V^{-1}s^{-1})	Hole Mobility (cm^{2}V^{-1}s^{-1})	$\mu_e\tau_e$ (cm^{2}V^{-1})	$\mu_h\tau_h$ (cm^{2}V^{-1})
HgTe	SM	-0.14		20.8	10^{-2}-10^{-3}	25000	350		
HgSe	SM	-0.06		25.6		20000	2		
α-HgS	D	2.03		23.5(∥), 18.2(⊥)	3450 (∥), 11080 (⊥)	30(∥), 10(⊥)			
β-HgS	SM	0.54		18.2		250			
CdTe	D	1.48	4.43	10.4	10^9	1050	100	3.3×10^{-3}	2×10^{-4}
CdSe (c)	D	1.74	5.5	10.0	10^5	800	50	7.2×10^{-4}	7.5×10^{-5}
CdSe (h)	D	1.75	5.5	9.3(⊥), 10.2(∥)	10^8	840	75	6×10^{-5}	7.5×10^{-5}
CdS (c)	D	2.42	6.3	5.4		340	50		
CdS (h)	D	2.51	7.8	8.3(⊥), 8.7(∥)	10^{10}	330	48	10^{-7}	
ZnTe	D	2.28	7.0	10.4	10^{10}	340	100	1.4×10^{-6}	7×10^{-5}
ZnSe (c)	D	2.63	8.0	9.2	2×10^9	540	28	4×10^{-5}	
β-ZnS (c)	D	3.58	8.2	8.9	10^{10}	165	10		
α-ZnS (w)	D	3.91		8.6(⊥), 8.4(∥)	10^8-10^{12}	280(∥), 165(⊥)	100-800		
ZnO (c)	D	3.35	7.5	9.0		200	180		
ZnO (w)	D	3.37		7.8(⊥), 8.8(∥)	10^9	250(∥), 280(⊥)	125		
β-MgTe	D	3.49		6.1					
β-MgSe	D	4.05		5.2					
β-MgS	D	4.5 (77K)		4.5					

Producing semiconductor materials - 1

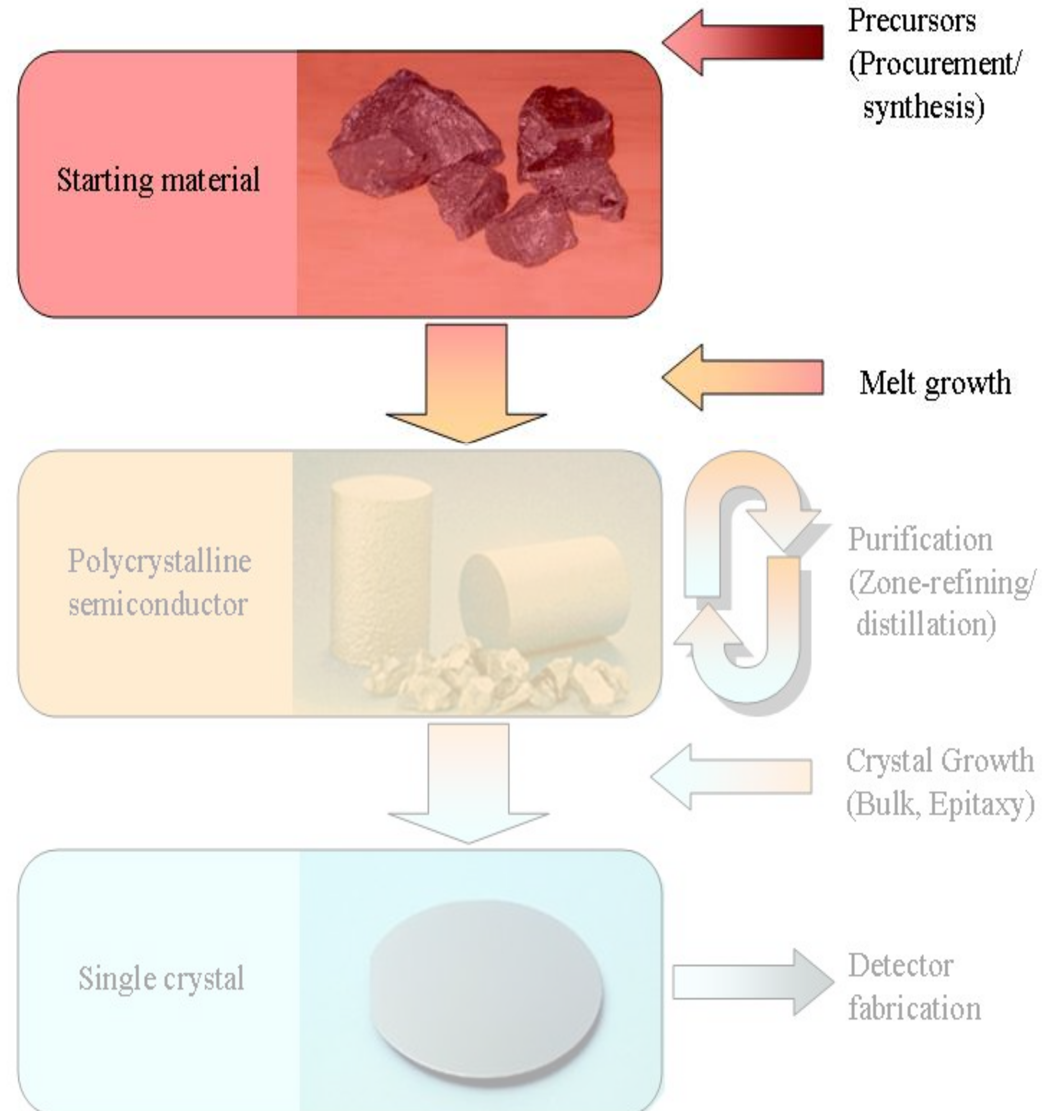

Precursors – raw stock

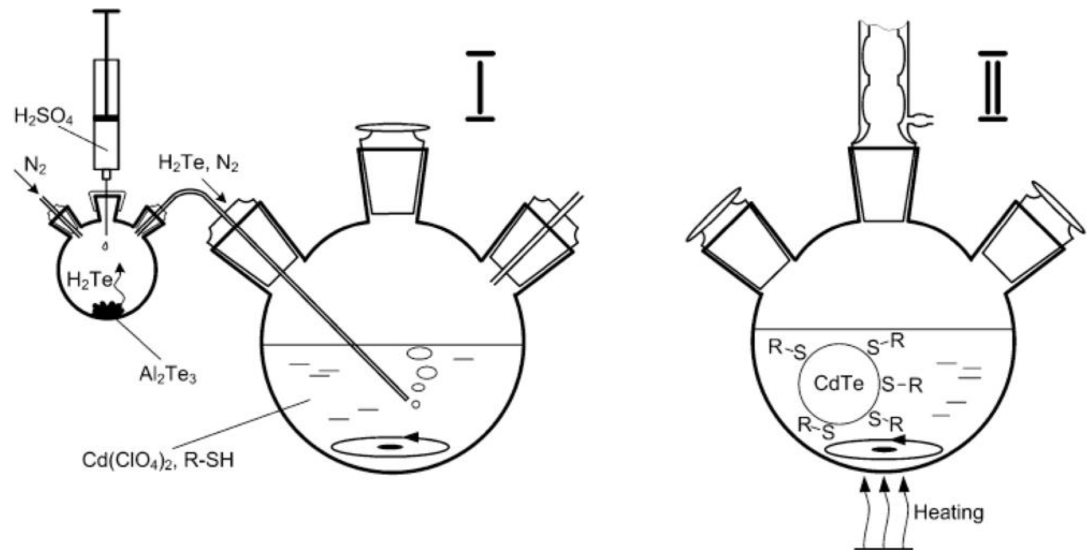

Scrap

Synthesis

Producing semiconductor materials - 2

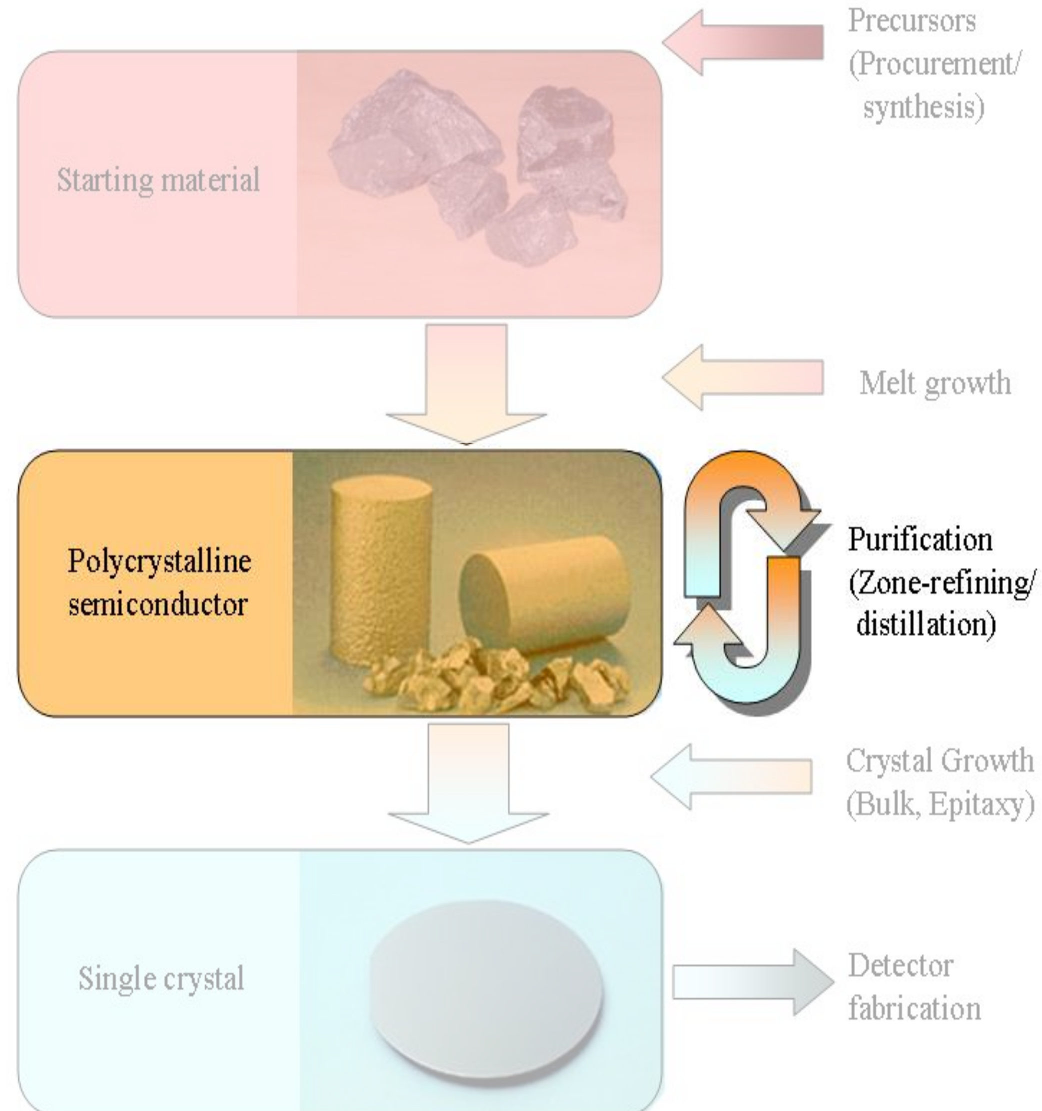

Growth/ purification

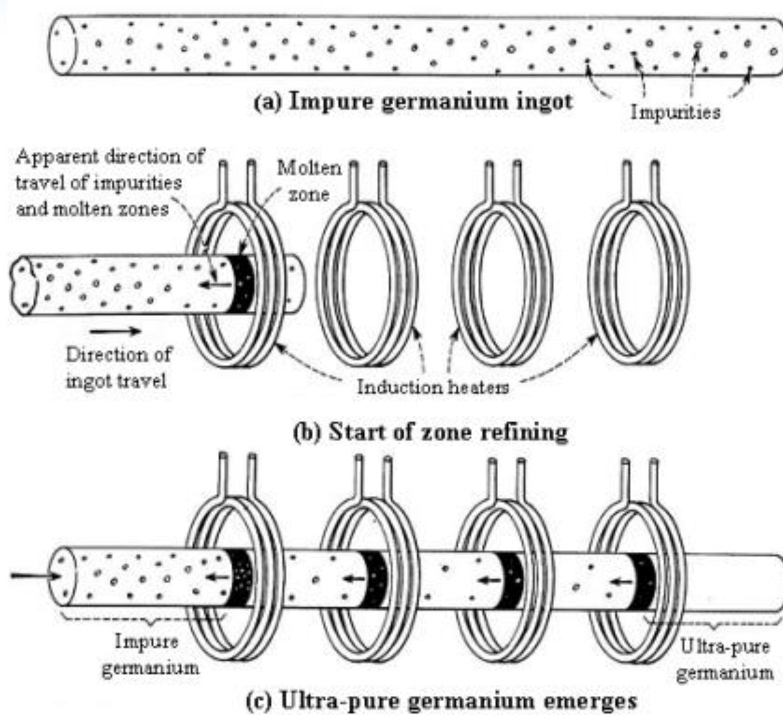

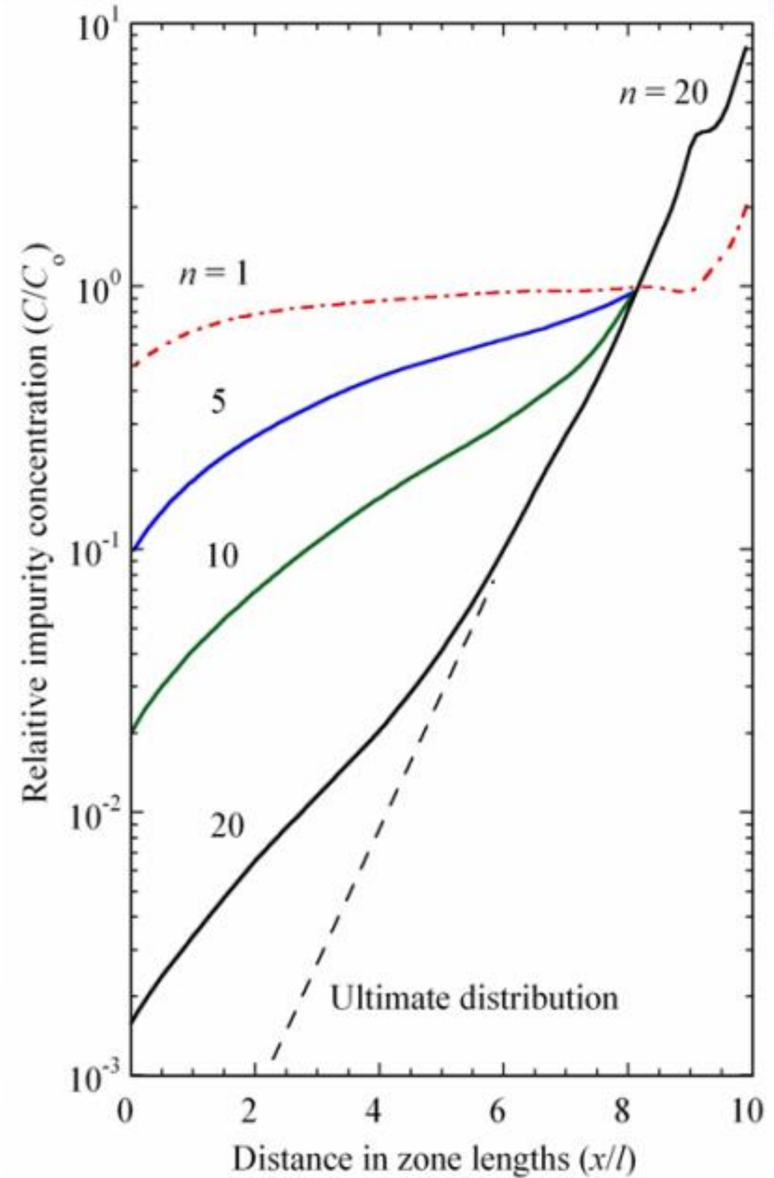

Producing semiconductor materials - 3

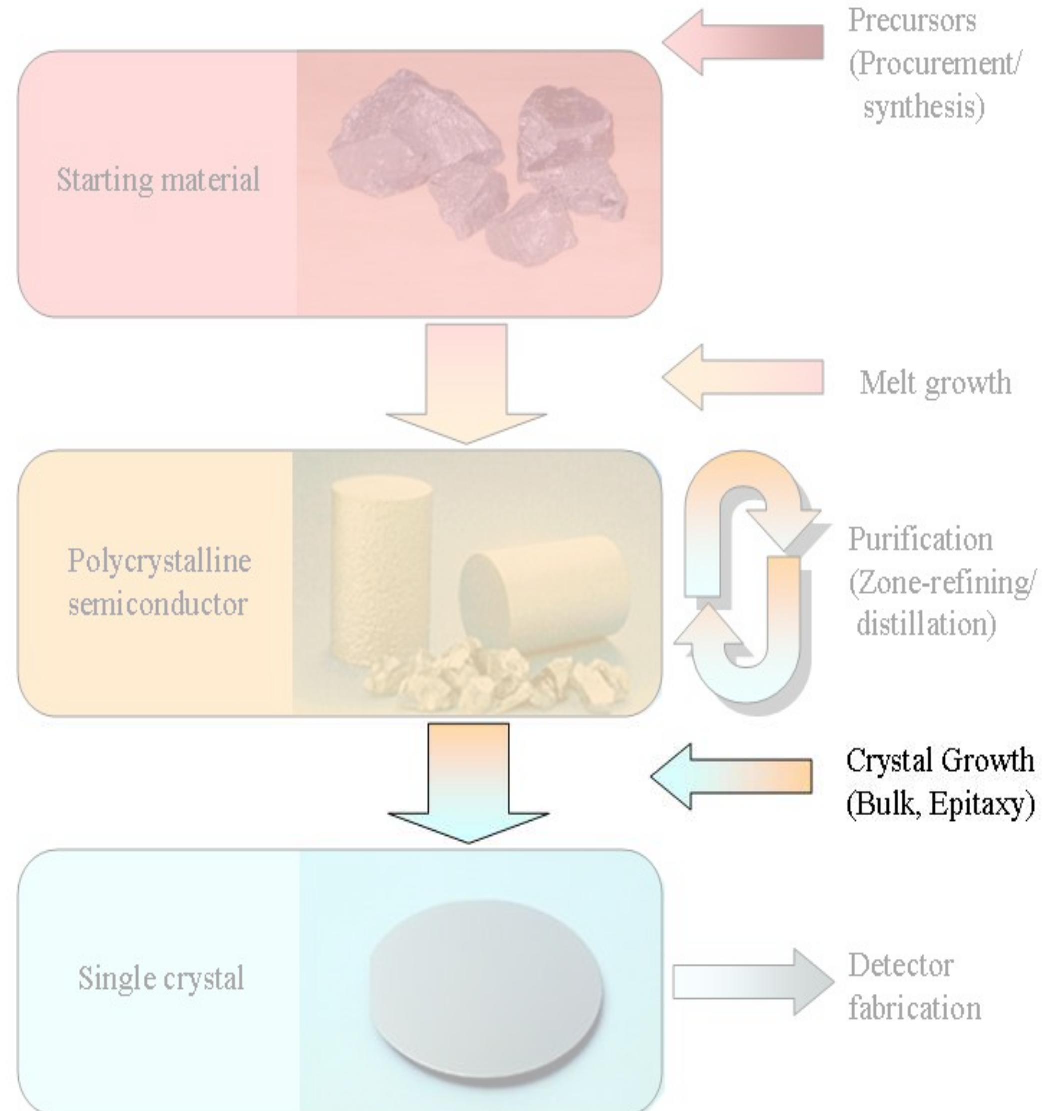

Crystal growth

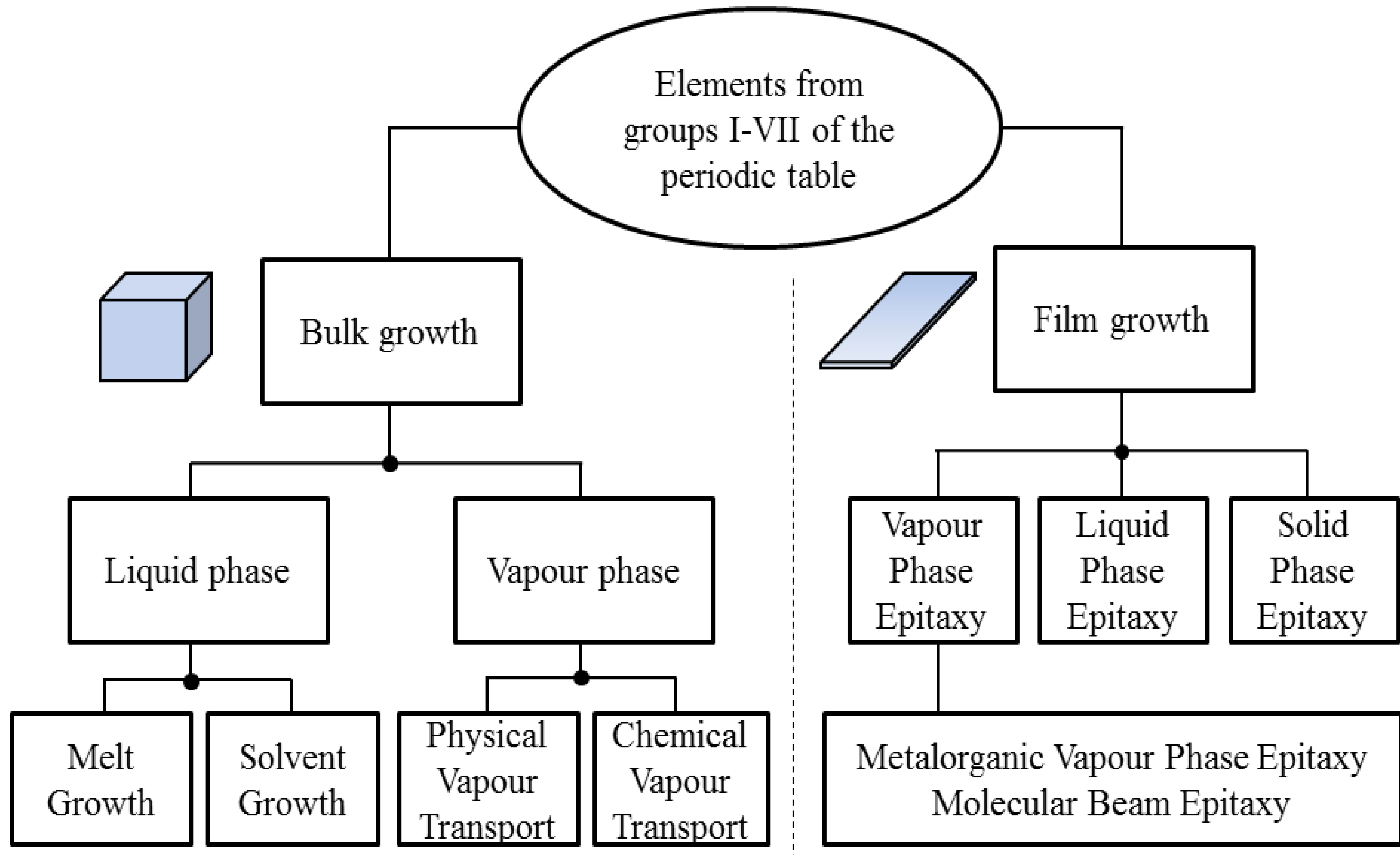

Bulk growth (Czochralski)

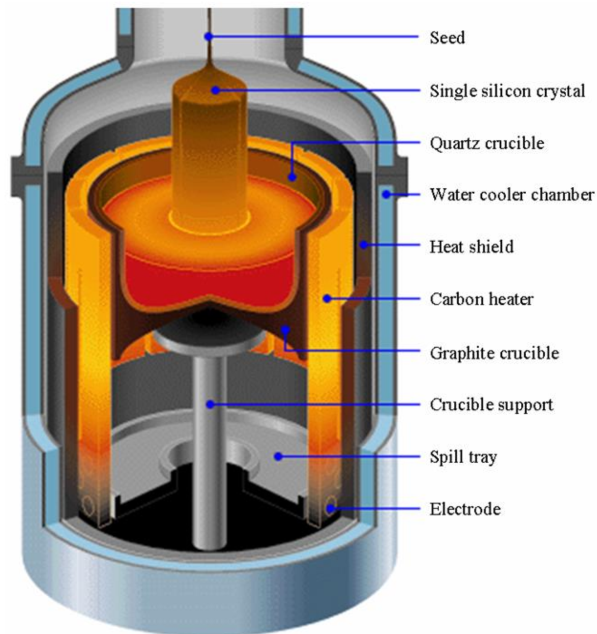

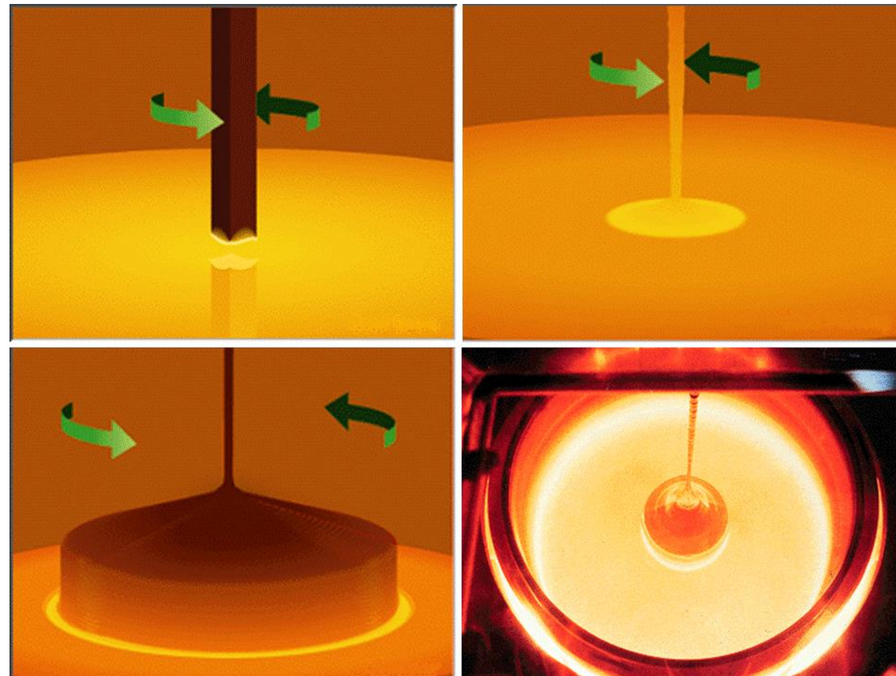

Vapour phase growth (Epitaxy)

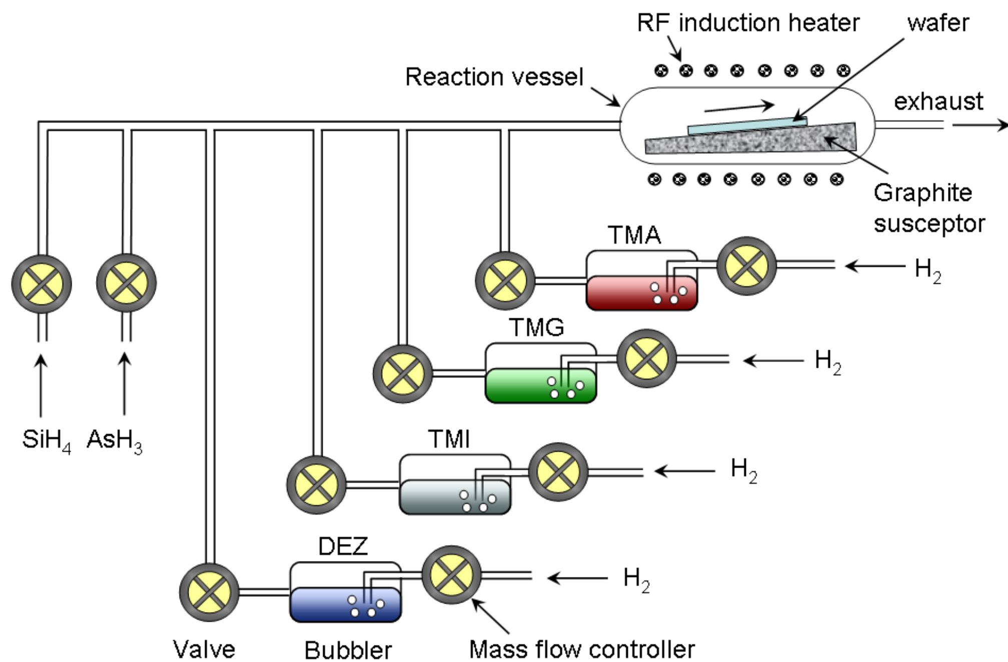

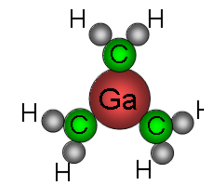

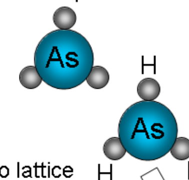

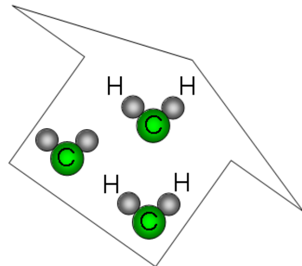

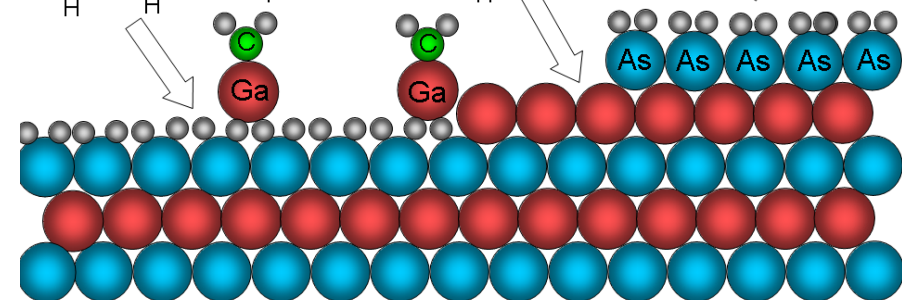

MOCVD Metal-Organic Chemical Vapour Deposition.

Vapour phase growth (common reactors)

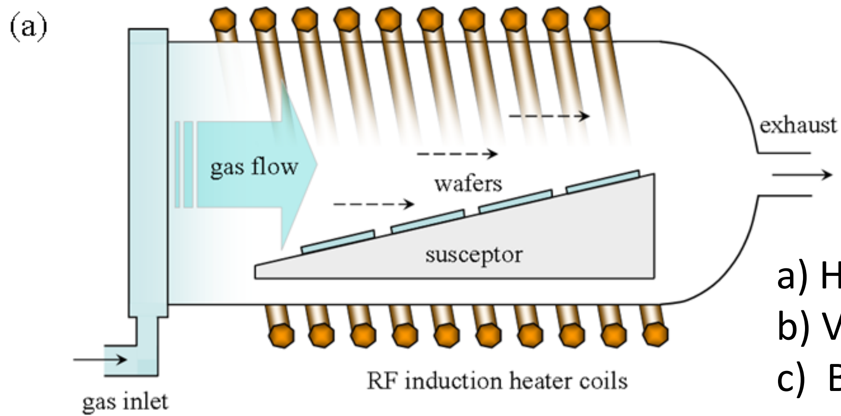

a) Horizontal
b) Vertical
c) Barrel

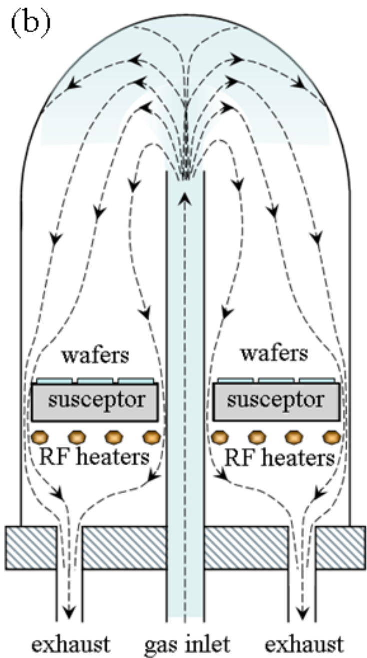

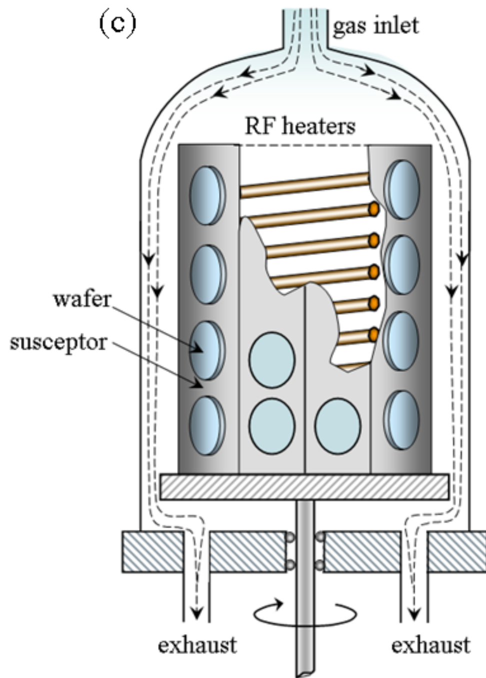

MBE

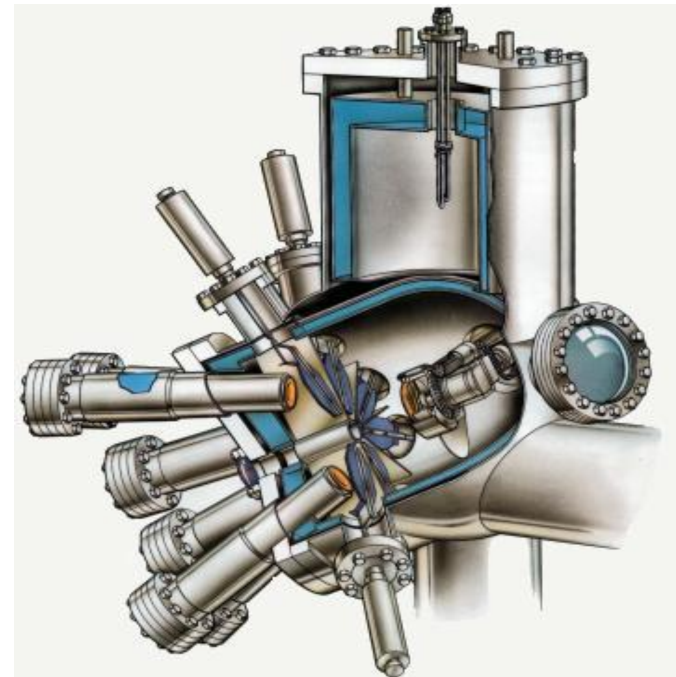

Ternary compounds - phase diagram III-V materials

Solutions can be soluble within each other

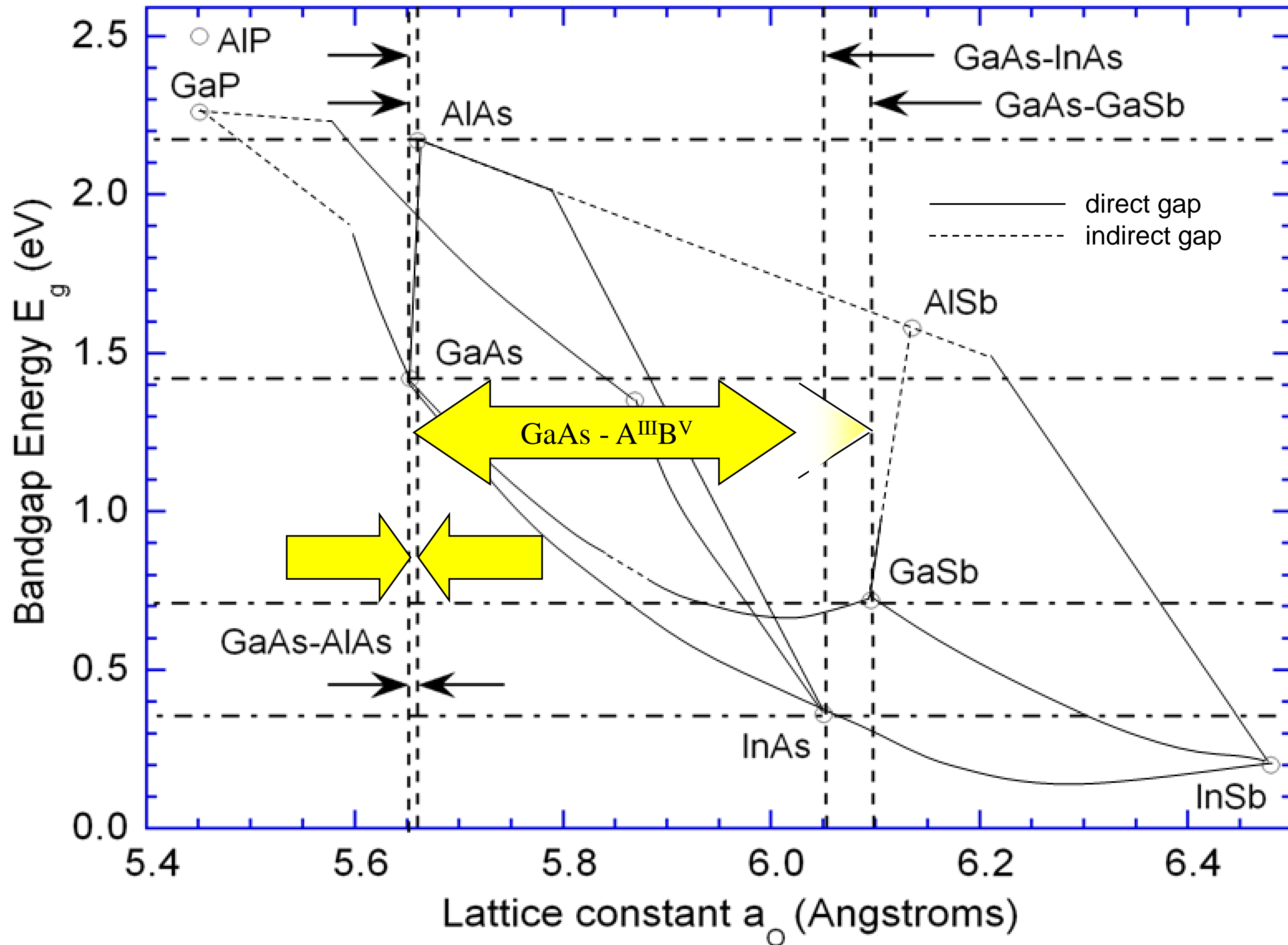

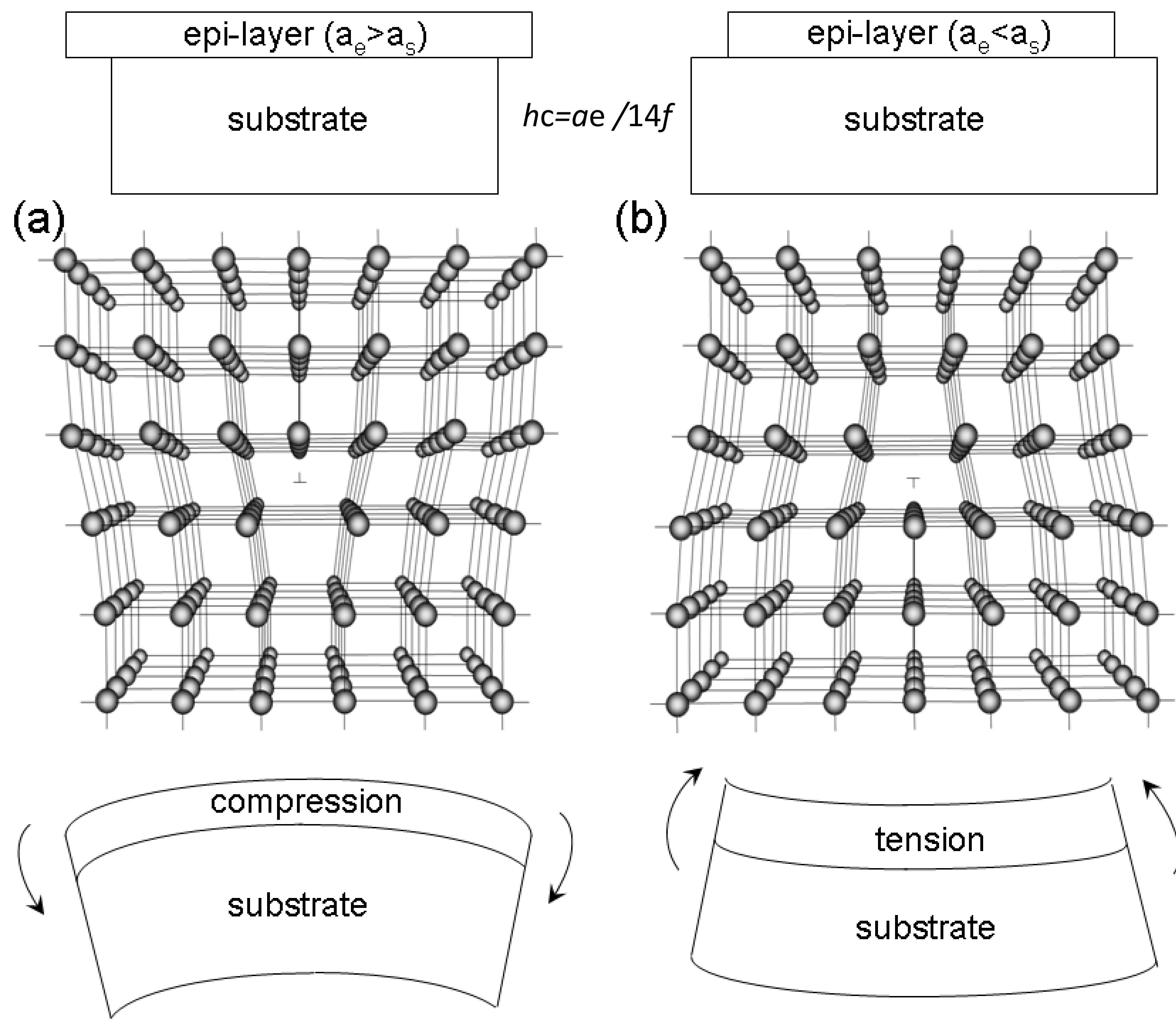
epi-layer (a_e>a_s)
substrate
hc=ae /14f
epi-layer (a_e<a_s)
substrate
(a)
(b)
compression
substrate
tension
substrate

Advantages and disadvantages of the main epitaxial growth techniques

Growth Method	Features	Advantages	Disadvantages
Liquid Phase Epitaxy (LPE)	Growth from supersaturated solution on to substrate	Simple low cost equipment and high throughput. Very high quality material. No toxic gases and easily handled solids Good control of impurities. High growth rates (0.1-1 micron/min). Suitable for selective growth	Difficult to grow abrupt heterostructures. Limited substrate areas. Poor control over the growth of very thin layers. Re-dissolution of the grown material. Poor uniformity over large areas. High growth temperatures for some compounds (e.g., 900ºC for InP)
Chemical Vapour Deposition (CVD)	Solid material is deposited from the vapor phase onto a heated substrate. Similar in many respects to VPE	Can produce very high purity conformal films. Can be used to process any metallic or ceramic compound. Relatively high deposition rate, few hundred microns hr^{-1}	Frequently highly volatile and toxic precursors are used. Films are deposited at high temperature which may limit the substrate selection and/or introduce stresses into the grown film
Vapor Phase Epitaxy (VPE)	Uses metal halides as transport agents to grow	Relatively simple reactors. Extremely high purity material	No Al compounds, thick layers. Toxic precursor gases.
Multi-Tube Physical Vapour Transport (MTPVT)	Controlled growth of high volatility II-VI compounds directly from the vapour phase	Simple, low temperature process. In-situ compounding High quality material. Reusable quartz ware. Low cost	Lattice matched substrates difficult to find for some compounds
Metal Organic Chemical Vapor Deposition (MOCVD)	Uses metal-organic compounds as the sources.	High quality material. Atomically abrupt interfaces. Low temp growth High vapour pressure material growth possible In-situ monitoring with (RAS)	Expensive and slow (~3 monolayer /sec= 3 µm/hr). Some sources very toxic. Tendency for C contamination. Several growth parameters to control.
Molecular Beam Epitaxy (MBE)	Deposit epi-layer in ultrahigh vacuum, in-situ characterization. Low temperature operation.	High quality material. Most precise epi-growth technique. Atomically abrupt interfaces. Less sensitive than other techniques to outdiffusion and autodoping. No toxic gases. Easily handled solids. Relatively simple chemistry. In-situ monitoring (RHEED).	Expensive and slower (~1 monolayer /sec = 1 µm/hr). UHV required. Hard to grow materials with high vapor pressure. Run-to-run reproducibility of layer thickness and composition. Surface "oval defects" Memory effect for P species

esa

Detector fabrication and characterization

Producing semiconductor materials - 4

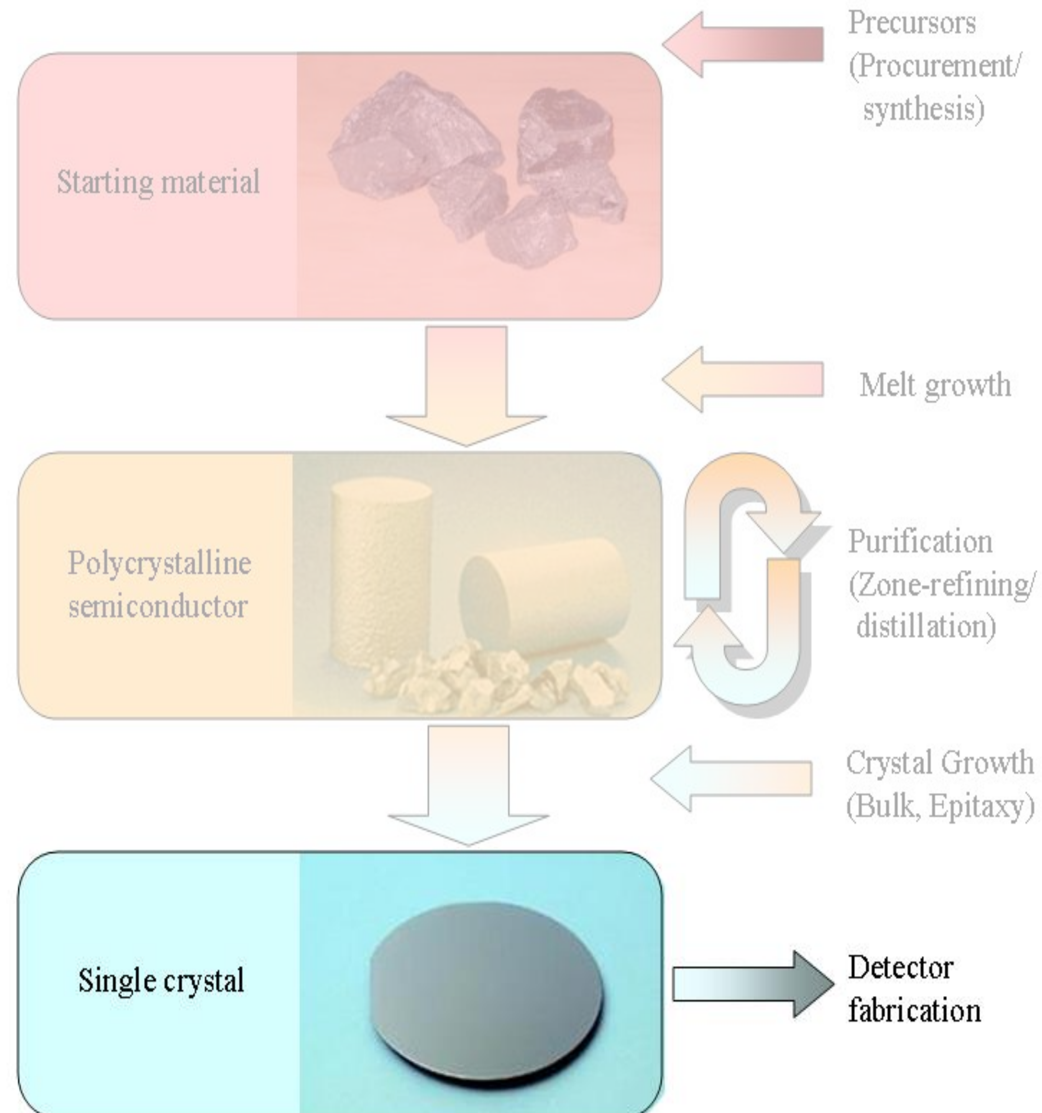

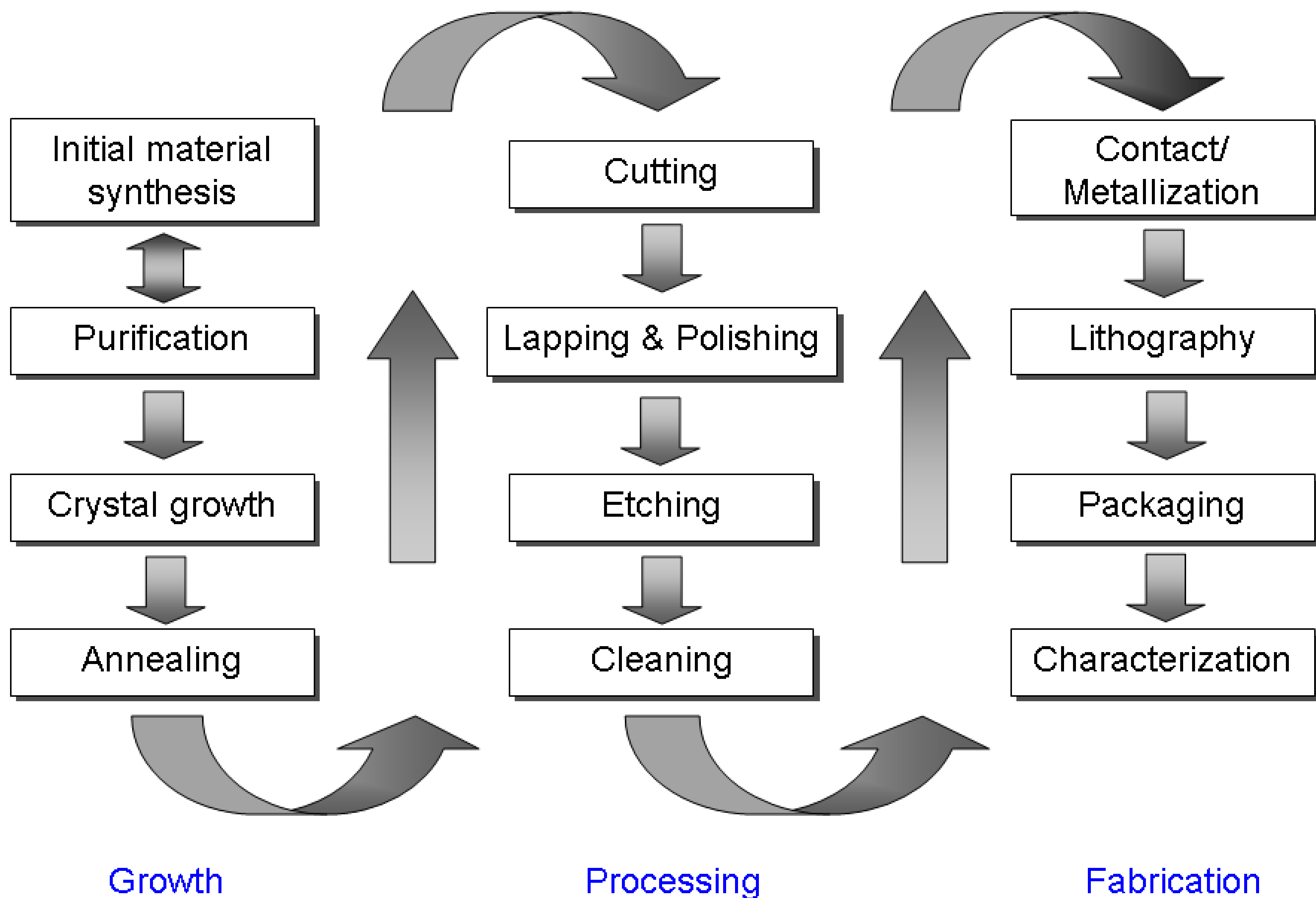
Detector production sequence
Initial material synthesis
Purification
Crystal growth
Annealing
Cutting
Lapping & Polishing
Etching
Cleaning
Contact/ Metallization
Lithography
Packaging
Characterization
Growth
Processing
Fabrication

Lithography – chip production

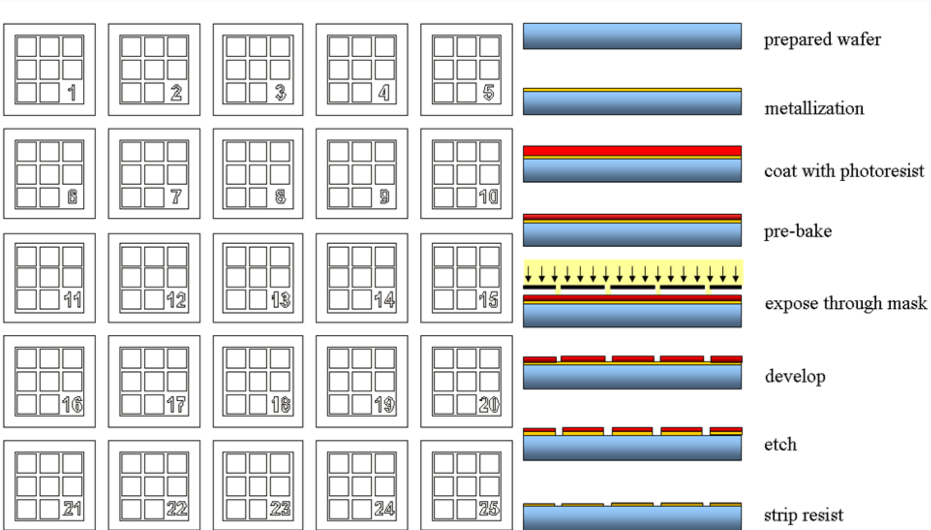

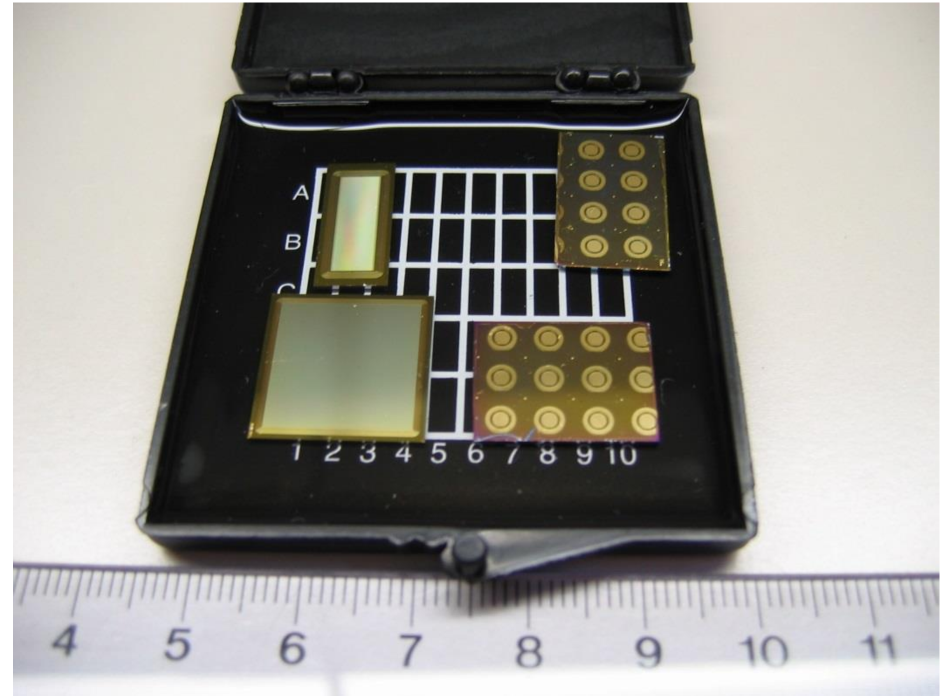

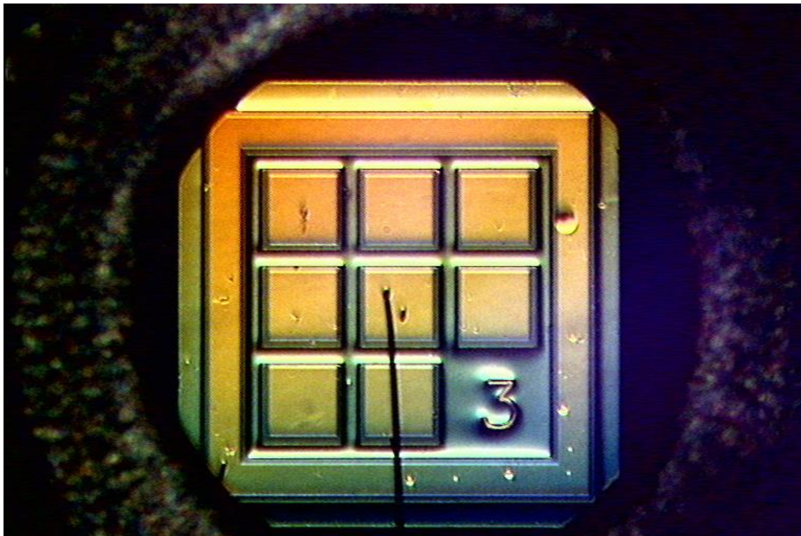

Detector fabrication and packaging

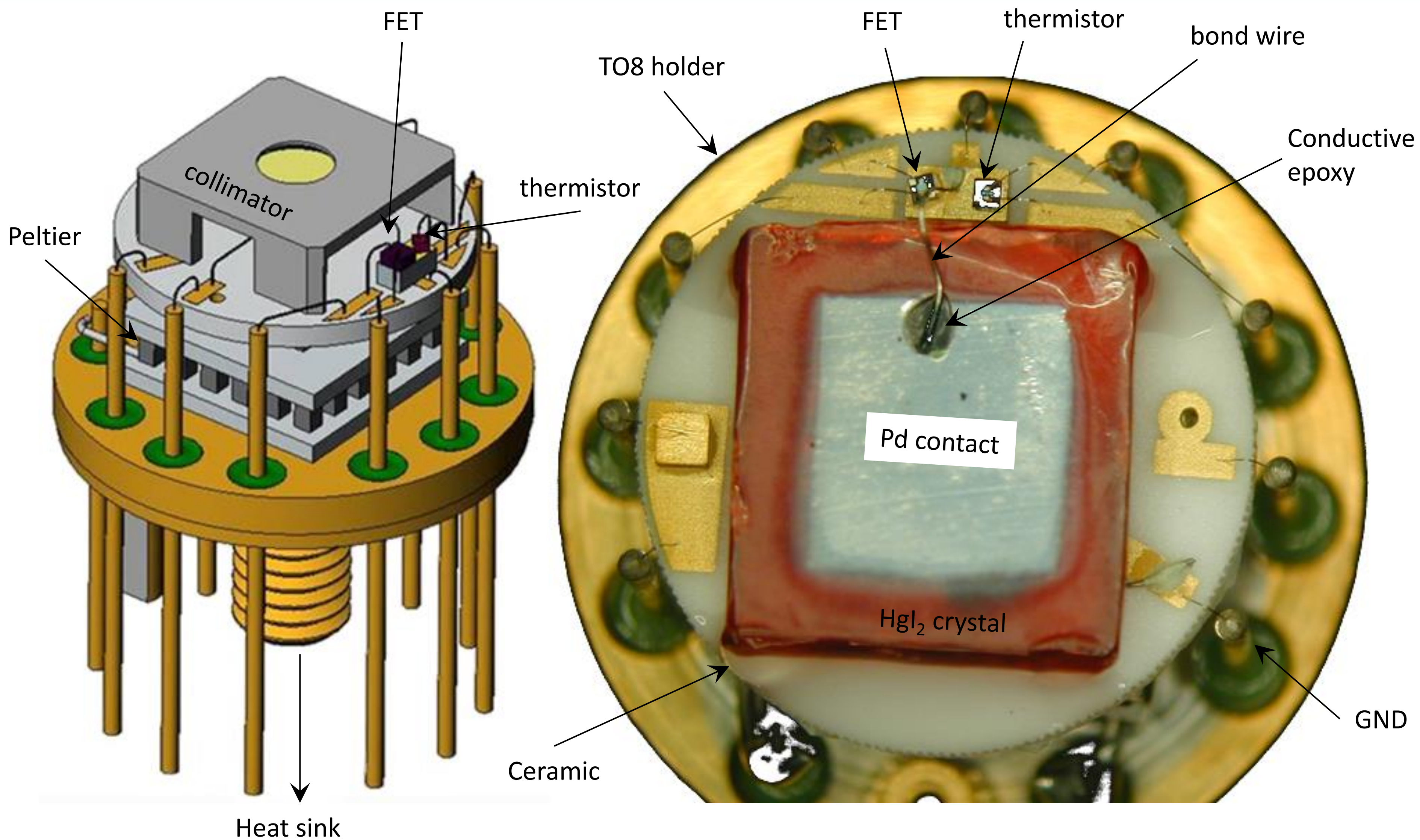

Detector configuration can be optimized for a given application

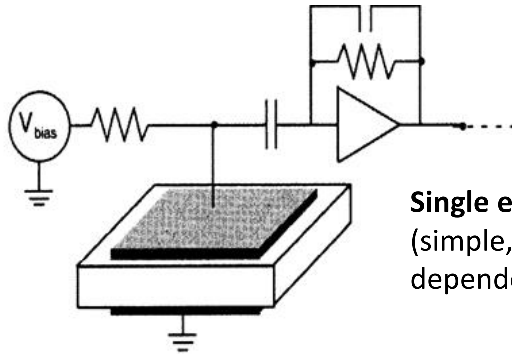

Single element planar structure
(simple, thickness limited, ΔE heavily dependent on transport properties.)

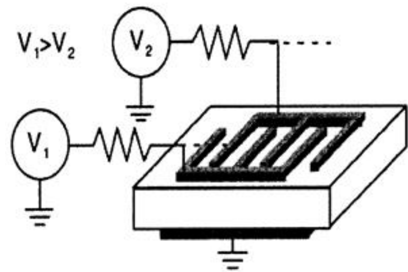

Co-planar grid structure
(good resolution, large volumes possible, complicated photolith.

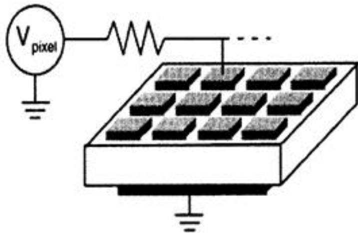

Pixel detector structure
Simple, small pixel effect – very good energy resolution, charge sharing complicated electronics/readout.

Summary of the salient properties of the various single charge sensing/ correction schemes. For the purposes of comparison, we only list only room temperature results for CdZnTe detectors. Better energy resolution can generally be achieved with cooling.

Technique	ΔE@ 662 keV, size	Advantages	Disadvantages
Planar [40]	8%, 18 × 18 × 2 mm^3	Simple	Thickness limited to a few mm Resolution heavily dependent on carrier transport properties – particularly holes.
RTD [40]	1.4%, 18 × 18 × 2 mm^3	Good resolution	Loss of counts in photopeaks (~60%) Thickness limited to a few mm Improvement limited to particular energy window. Additional electronics
Bi-parametric [41]	1%, 4 × 4 × 5 mm^3	High resolution Little loss of photopeak events	Complicated electronics Complicated calibration Depth correction limited to ~1 cm Expensive
Stack [11]	1%, 5 × 5 × 2.25 mm^3	Relatively simple Good resolution	Volume limited by complexity of stack fabrication
Hemispherical [13]	1.6%, 10 × 10 × 5 mm^3	Simple, good resolution Similar performance to planar + RTD	Fabrication difficulties Volume limited to ~ 1 cm^3
Drift-strip [29]	0.6%, 10 × 10 × 3 mm^3	Very high resolution	Thickness limited to ~ few mm
Small Pixel [42]	1.2%, 20×20×10.5 mm^3 2.46 mm pixel size	Simple High resolution	Large number of pixels to achieve large area leading to complex electronics. Charge sharing between pixels.
+ steering grids and 3D sensing [39]	0.8%, 15×15 ×10mm^3, 11×11 pixels	Very high resolution	More complicated electronics than above
Virtual Frisch-grid [43]	1.4%, 5 × 5 × 14 mm^3	Simple construction High resolution Large thickness possible	Essentially pixel device Small area without applying other techniques
+"mixed" electrode and bi-parametric [38]	0.7%, 10 × 10 × 10 mm^3	Very high resolution	More complicated electronics than above
Coplanar grid [32]	1.8%, 15 × 15 × 10 mm^3	Good performance. Insensitive to hole trapping. Large volumes ~few cm^3	Complicated photolithography Max volume limited by crystal availability
Ring-drift [34]	0.7%, 5 × 5 × 1 mm^3	Simple Very high resolution	Complicated spatial response Only small volumes demonstrated

Radiation detection

In order to detect radiation - it must interact with the material of the detector and transfer energy in some recognizable form, *e.g.* energy loss *via* ionization and excitation

The detection of particles is possible *via* their energy loss in the material it traverses

Radiation	Most probable interaction
Charged particles	Ionization, Bremsstrahlung,
Hadrons	Nuclear interactions
Photons	Photoelectric, Compton effect, pair production
Neutrinos	Weak interactions

Total energy loss can be *via* single a interaction or energy loss by multiple reactions ➛ in either case, detection is made possible by the energy deposition of the secondary charged particles produced ultimately ending up with ionization

Typical signal chain

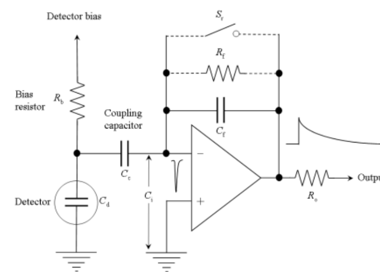

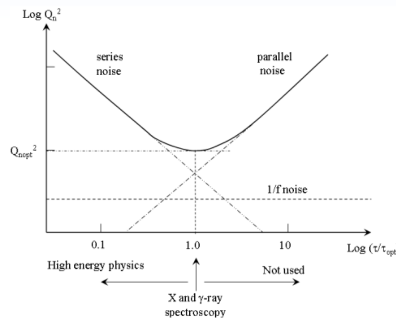

Bias supply

V_b

Discriminator

Scalar

Gate

Charge sensitive pre-amp

Shaping amplifier

Multi-Channel Analyzer

Detector

i

V

V

Time

Time

Time

What has been looked at?

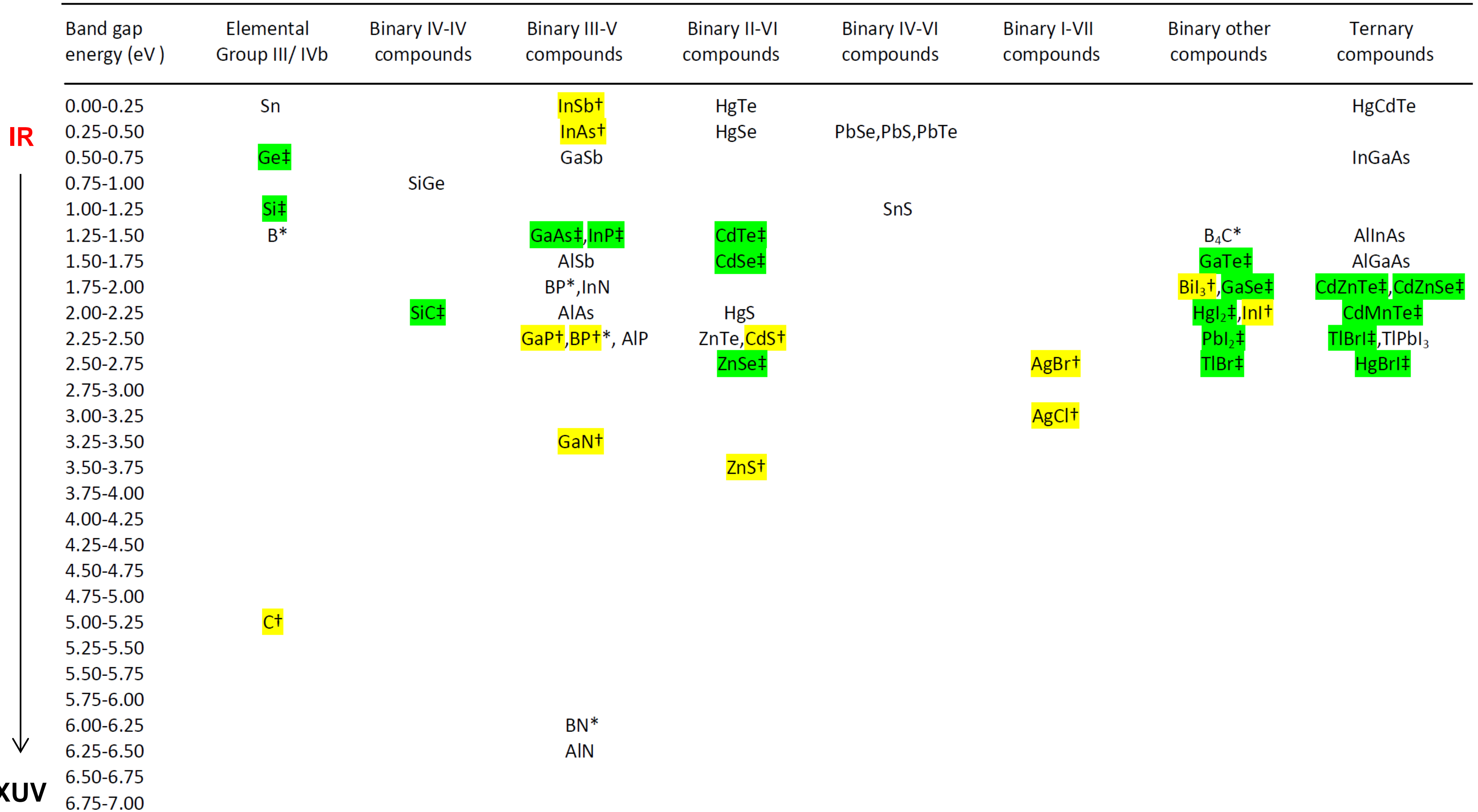

Compound semiconductor material listed by group and in order of increasing band-gap energy ranging from near IR to XUV wavelengths

Band gap energy (eV)	Elemental Group III/ IVb	Binary IV-IV compounds	Binary III-V compounds	Binary II-VI compounds	Binary IV-VI compounds	Binary I-VII compounds	Binary other compounds	Ternary compounds
0.00-0.25	Sn		InSb†	HgTe				HgCdTe
0.25-0.50			InAs†	HgSe	PbSe,PbS,PbTe			
0.50-0.75	Ge‡		GaSb					InGaAs
0.75-1.00		SiGe						
1.00-1.25	Si‡				SnS			
1.25-1.50	B*		GaAs‡,InP‡	CdTe‡			B_4C*	AlInAs
1.50-1.75			AlSb	CdSe‡			GaTe‡	AlGaAs
1.75-2.00			BP*,InN				BiI_3†,GaSe‡	CdZnTe‡,CdZnSe‡
2.00-2.25		SiC‡	AlAs	HgS			HgI_2‡,InI†	CdMnTe‡
2.25-2.50			GaP†,BP†*, AlP	ZnTe,CdS†			PbI_2‡	TlBr‡,$TlPbI_3$
2.50-2.75				ZnSe‡		AgBr†	TlBr‡	HgBrI‡
2.75-3.00								
3.00-3.25						AgCl†		
3.25-3.50			GaN†					
3.50-3.75				ZnS†				
3.75-4.00								
4.00-4.25								
4.25-4.50								
4.50-4.75								
4.75-5.00								
5.00-5.25	C†							
5.25-5.50								
5.50-5.75								
5.75-6.00								
6.00-6.25			BN*					
6.25-6.50			AlN					
6.50-6.75								
6.75-7.00								

†Compounds which have shown a response to energetic radiation. ‡Materials for which spectroscopic measurements (i.e. ΔE/E>1) have been made at X-ray wavelengths.*Investigated for n detection.

The usual suspects

Room temperature properties of wide band gap compound semiconductor materials suitable for hard X- and γ-ray detectors. The abbreviations are: C = Czochralski, LEC = Liquid Encapsulated Czochralski, THM = Traveller Heater Method, BM = Bridgman Method, HPB = High Pressure Bridgman and VA=Vertical Ampoule Method.

Material	Growth method	Atomic Number	Density (g/cm^3)	Band gap (eV)	Epair (eV)	Resist-ivity (Ω-cm)	$\mu\tau$(e) Product (cm^2/V)	$\mu\tau$ (h) Product (cm^2/V)
Si	C	14	2.33	1.12	3.6	10^4	4×10^{-1}	2×10^{-1}
Ge	C	32	5.33	1.57	4.6	50	1	1
GaAs	CVPE	31,33	5.32	1.43	4.2	10^{11}	10^{-2}	5×10^{-4}
InP	LEC	15.49	4.78	1.43	4.2	10^6	5×10^{-6}	$< 2\times10^{-5}$
CdTe	THM	48,52	6.2	1.44	4.4	10^9	3×10^{-3}	2.6×10^{-4}
$Cd_{0.9}Zn_{0.1}Te$	HPB	48,30,5 2	5.78	1.57	4.6	10^{11}	7×10^{-3}	9×10^{-5}
PbI_2	BM	82,53	6.2	2.3-2.6	4.9	10^{12}	8×10^{-6}	9×10^{-7}
HgI_2	VAM	80,53	6.4	2.13	4.2	10^{13}	10^{-4}	4×10^{-5}
TlBr	BM	81,35	7.56	2.68	6.5	10^{12}	3×10^{-5}	1.5×10^{-6}

For compounds, hole $\mu\tau$ is usually 10 times less than electron $\mu\tau$

Some of the best spectroscopic results

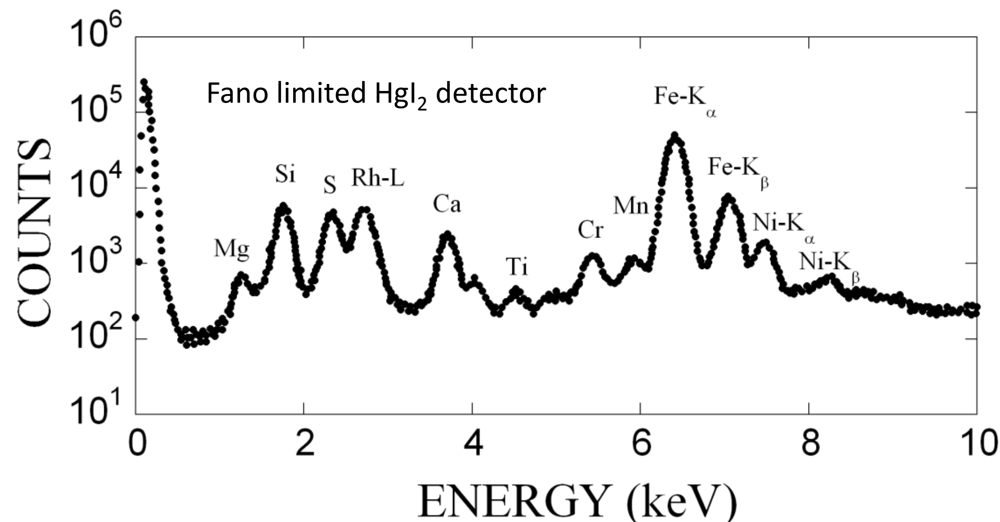

HgI_2 5 mm^2, 200 μm thick detector at 0°C. ΔE at 5.9 keV =198 eV (Iwanczyk *et al.* 1989)

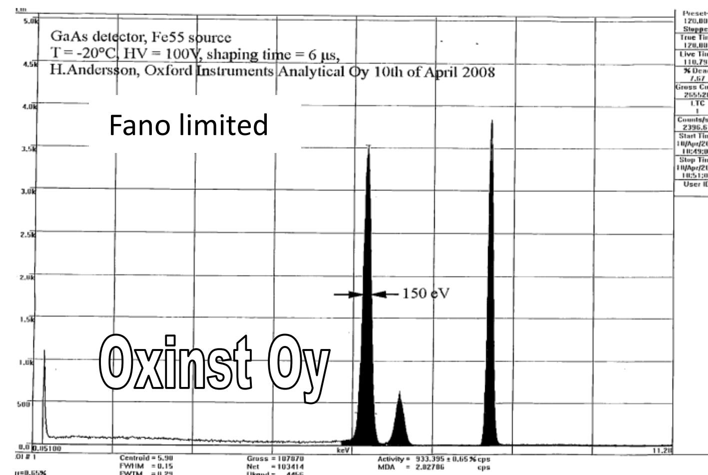

GaAs 0.5 x 0.5 x 0.2mm³ detector at -20°C. ΔE at 5.9 keV =150 eV (courtesy S. Nennonen)

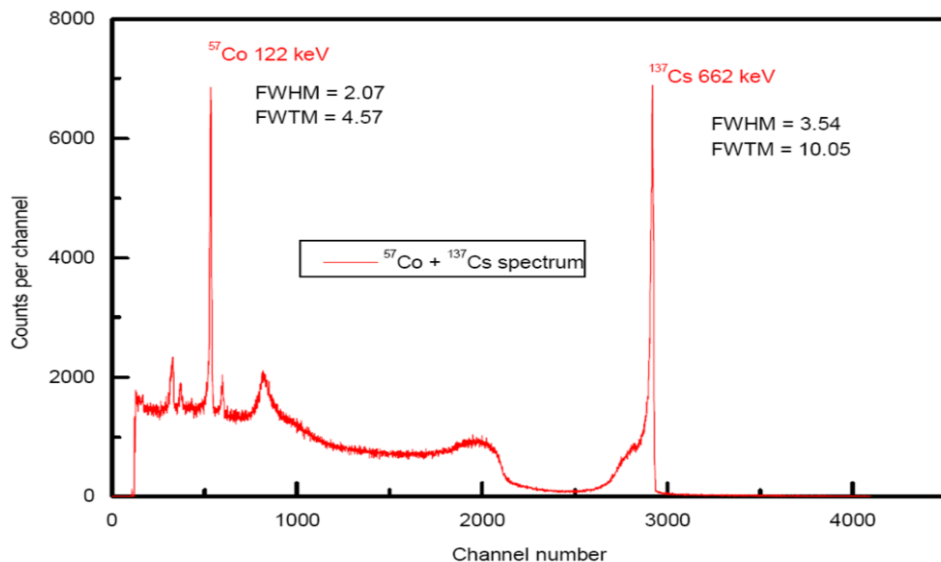

CdTe 1cm^2, 2.1 mm thick detector cooled to –35°C. ΔE at 662 keV was 3.5 keV (Khusainov et al. 1999).

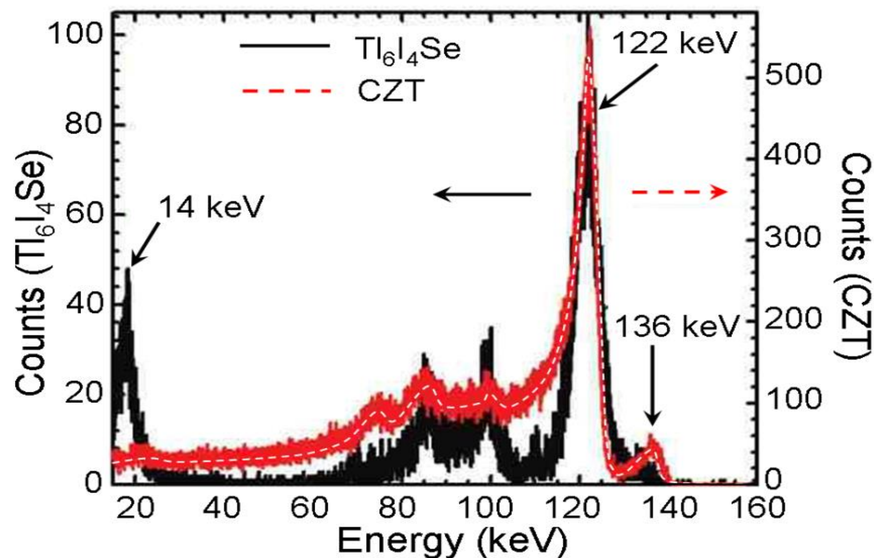

Tl_6I_4Se, 6×4×2 mm^3 detector. ΔE at 122 keV = 5.7 keV (Johnsen *et al.* 2011)

These results only apply to small thin detectors, because.....

Charge transport described by the Hecht relation

$$CCE = \frac{Q}{Q_o} = \frac{\lambda_e}{L}\left[1-\exp\left(-\frac{L-x_o}{\lambda_e}\right)\right] + \frac{\lambda_h}{L}\left[1-\exp\left(-\frac{x_o}{\lambda_h}\right)\right]$$

$\lambda_e = \mu_e \tau_e E$ $\quad \lambda_h = \mu_h \tau_h E$ but $\mu\tau$'s rarely over 10^{-4}cm^{2}V^{-1} and E usually < 10^4 Vcm^{-1}

For λ/L <1 there will be a position dependence in the collected charge and spectral broadening

For the general case of $\lambda_e \neq \lambda_h$, the relative broadening is given by

$$\left(\frac{\sigma_c^2}{E}\right)^2 = \frac{2\lambda_e^2\lambda_h^2}{L^3(\lambda_e-\lambda_h)}\left(e^{-L/\lambda_e} - e^{-L/\lambda_h}\right) - \frac{1}{L^4}\left[\lambda_e^2\left(e^{-L/\lambda_e}-1\right) + \lambda_h^2\left(e^{-L/\lambda_h}-1\right)\right]^2$$

$$-\frac{\lambda_e^3}{2L^3}\left(e^{-2L/\lambda_e}-1\right) - \frac{\lambda_h^3}{2L^3}\left(e^{-2L/\lambda_h}-1\right)$$

Bottom line - spectroscopy dominated by the carrier with the poorest transport properties

Iwanczyk et al., Nucl. Instr. and Meth., Vol., **A322** (1992) 421

CCE and spectral broadening

Three main noise components comprise the resolution function ΔE

Fano noise

$$F = \frac{\sigma^2_{\mathrm{exp}}}{var_{\mathrm{poisson}}} \Rightarrow \sigma^2_{\mathrm{F}} = FE\varepsilon$$

Electronic noise

$$\Delta e = \frac{2.355\,\varepsilon\,\mathrm{ENC}}{e}$$

For RC-RC shaping

$$ENC^2 = \left(\frac{\varepsilon^2}{8}\right)\left[\left(2eI + \frac{4kT}{R_b}\right)\tau + \left(4kTR_s + v_{na}^2\right)C_d^2\frac{1}{\tau} + 4A_f C_d^2\right]$$

current noise, voltage noise, 1/f noise

Charge trapping noise

$$\left(\frac{\sigma_{\mathrm{c}}^2}{E}\right)^2 = \frac{2\lambda_e^2\lambda_h^2}{L^3(\lambda_{\mathrm{e}}-\lambda_{\mathrm{h}})}\left(\mathrm{e}^{-L/\lambda_{\mathrm{e}}}-\mathrm{e}^{-L/\lambda_{\mathrm{h}}}\right) - \frac{1}{L^4}\left[\lambda_{\mathrm{e}}^2\left(\mathrm{e}^{-L/\lambda_{\mathrm{e}}}-1\right)+\lambda_{\mathrm{h}}^2\left(\mathrm{e}^{-L/\lambda_{\mathrm{h}}}-1\right)\right]^2 - \frac{\lambda_{\mathrm{e}}^3}{2L^3}\left(\mathrm{e}^{-2L/\lambda_{\mathrm{e}}}-1\right)+\frac{\lambda_{\mathrm{h}}^3}{2L^3}\left(\mathrm{e}^{-2L/\lambda_{\mathrm{h}}}-1\right)$$

$$\Delta E = f(\sigma_{\mathrm{F}}^2, \sigma_{\mathrm{e}}^2, \sigma_{\mathrm{c}}^2)$$

$$\Delta E = 2.355\sqrt{F\varepsilon E_{\mathrm{o}} + \left(\Delta e/2.355\right) + a_1 E_{\mathrm{o}}^{a2}}$$

assuming all components are normally distributed

CCE and spectral broadening

but $\mu\tau$'s rarely over $10^{-4} cm^2V^{-1}$

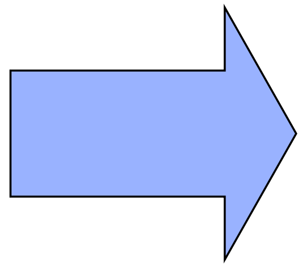

$\mu\tau_e = 10^{-4}\ cm^2V^{-1}$, $\mu\tau_h = 4x10^{-4}\ cm^2V^{-1}$

- ● Lab (296.2 K)
- ○ HASYLAB (296.0 K)
- △ BESSY (297.1 K)

Δc dominates

ΔF

Δe

7 mm^2, HgI_2

Energy resolution (keV)

10.0
1.0
0.1

0 20 40 60 80 100

Energy (keV)

Effect of $\mu\tau$ on performance – smaller the $\mu\tau$ the poorer the performance or thinner the detector

$\mu\tau \sim 10^{-2} \Rightarrow$ Fano limited

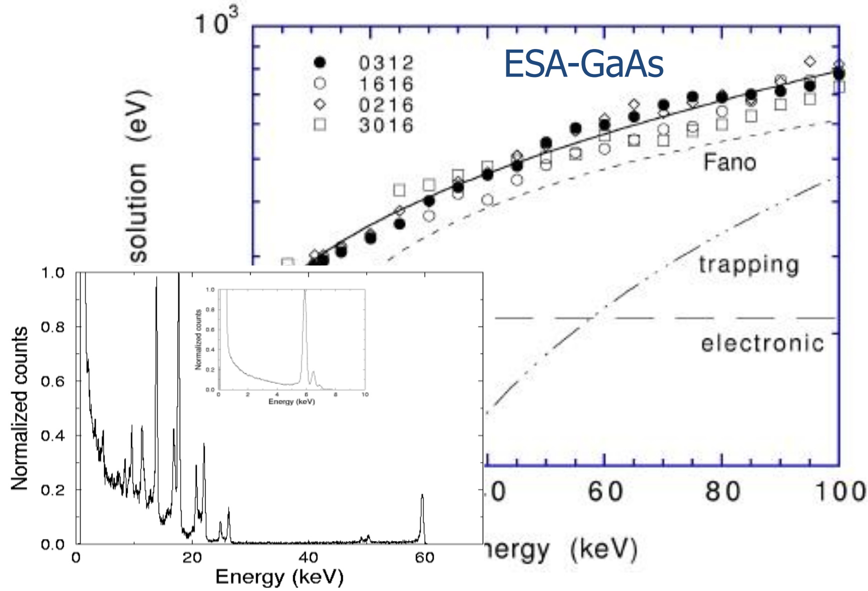

$\mu\tau \sim 10^{-3} \Rightarrow$ partially Fano limited

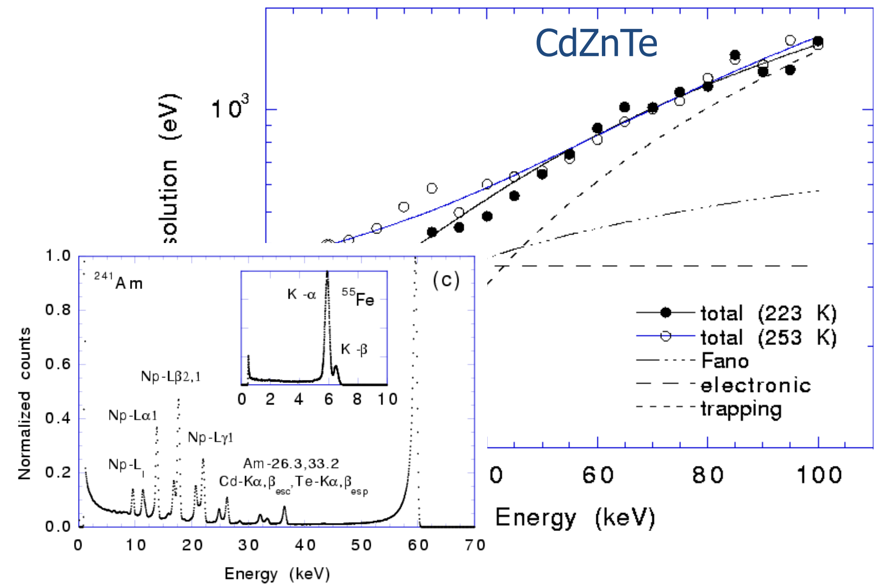

$\mu\tau \sim 10^{-4} \Rightarrow$ not Fano limited

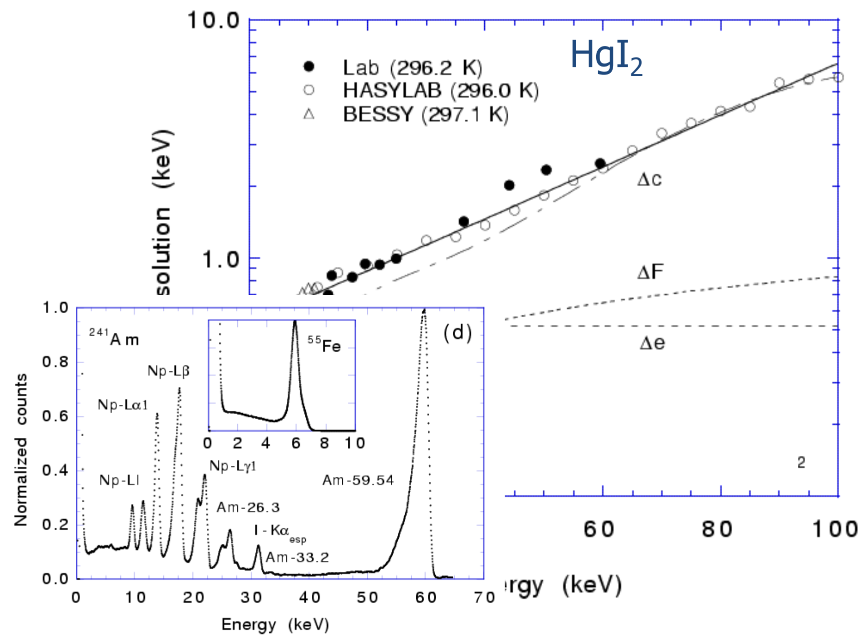

$\mu\tau \sim 10^{-5} \Rightarrow$ what's Fano limited ?

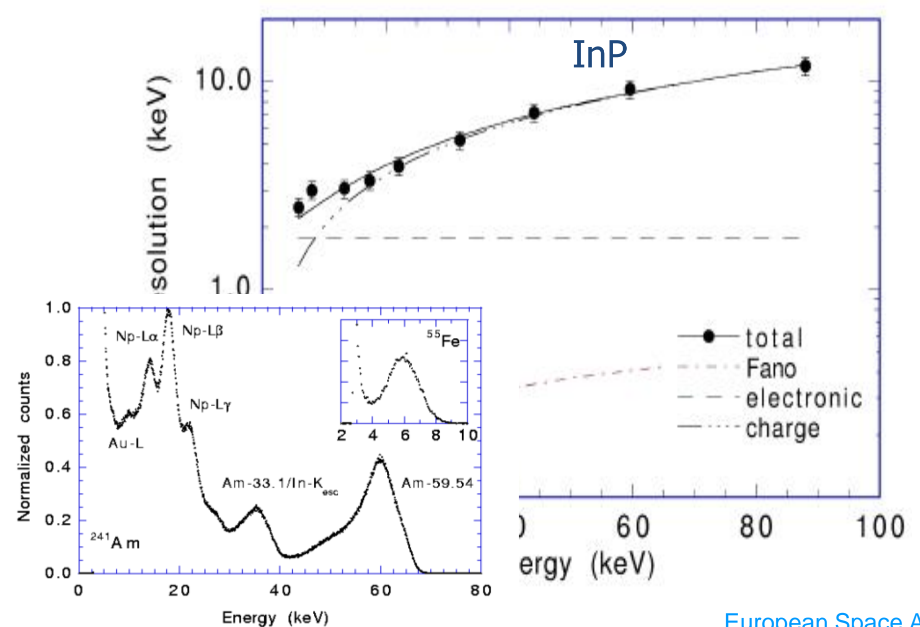

Neutron detection

Detection either by collisions (*e.g.*, n,p scattering) or capture reactions (n,α) etc.). In a conventional neutron capture reaction, >100,000 electrons and holes produced per event (~2.4×10^{-13} C)

- This can be detected directly without further amplification
- But . . . standard semiconductors do not contain enough neutron-absorbing nuclei to give reasonable neutron detection efficiency

1) put neutron absorber on surface of semiconductor?

2) develop boron-based compound semiconductor devices

Indirect detection

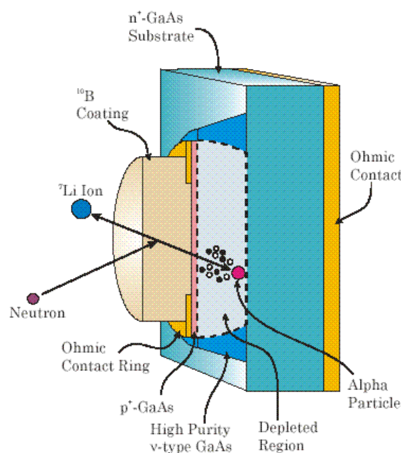

Coatings ^{6}LiF
^{10}B (3840 b)
^{6}Li (940 b)

ε_n ~ 4%
film only 2μm thick !

Direct detection

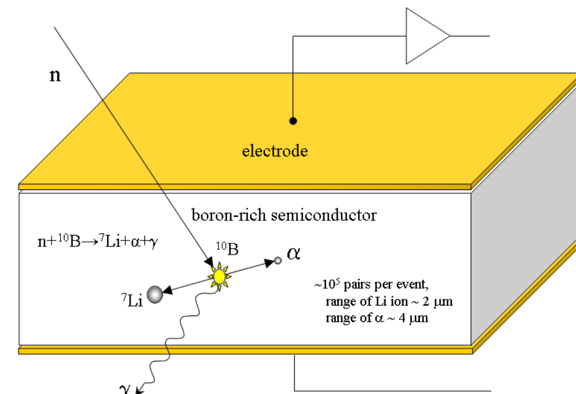

D.S. McGregor et al., Nucl. Instr. and Meth., A466 (2001) 126.

Neutron detection

High cross section neutron capture reactions

Reaction	Products	Reaction Q Value (MeV)	X-section [13,14] (barns)
$^{3}He + {}^{1}n \Rightarrow$	^{3}H(0.191 MeV) + ^{1}p(0.573 MeV),	0.764	5333
$^{10}B + {}^{1}n \Rightarrow$	^{7}Li (1.015 MeV) + $^{4}\alpha$(1.777 MeV),	2.792 (to ground state)	3837
	^{7}Li*(0.840 MeV) + $^{4}\alpha$(1.470 MeV),	2.310 (1st excited state)	
$^{6}Li + {}^{1}n \Rightarrow$	^{3}H(2.73 MeV) + $^{4}\alpha$(2.05 MeV),	4.780	940
$^{113}Cd + {}^{1}n \Rightarrow$	^{114}Cd + γ(0.56 MeV) + *conv. electrons*		20600
$^{155}Gd + {}^{1}n \Rightarrow$	^{156}Gd + γ(0.09 0.20,0.30 MeV) + *conv. electrons*		60900
$^{157}Gd + {}^{1}n \Rightarrow$	^{158}Gd + γ(0.08,0.18,0.28 MeV) + *conv. electrons*		254000
$^{235}U + {}^{1}n \Rightarrow$	fission fragments	201	583
$^{239}Pu + {}^{1}n \Rightarrow$	fission fragments	160	748

Suitable materials for direct neutron detection

Material	Advantages	Disadvantages
Boron (B)	Simple, 100% ^{10}B composition possible	Difficult to grow, slow growth, no obvious substrate
Boron nitride (BN)	Benign process.	Difficult to grow, slow growth, diamond substrate required
Boron phosphide (BP, $B_{12}P_2$)	Simple CVD, reasonable growth rates, cubic and rhombohedral forms look promising	Phosphine gas precursor, no obvious substrate, high temperature growth
Boron carbide (B_4C, B_5C)	Low temperature deposition, single, solid precursor, no lattice–matching required, neutron detection claimed	Expensive precursor, many polytypes, heterostructure may be required
Doped diamond C:B	Neutron detection claimed	Expensive, single uninterested vendor, low detection efficiency

PECVD reactor

Boron detector and preamp

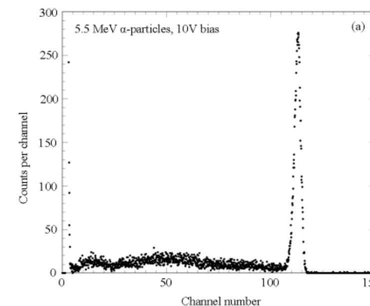

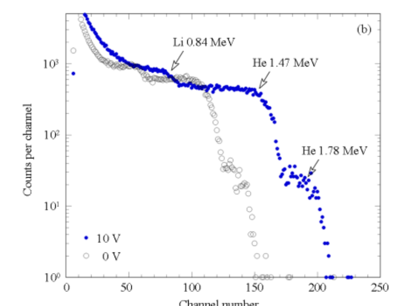

(a) The response of a 12.6 mm², 1.7 µm thick diode to a 5.5 MeV alpha particles. The bias was 10V. (b): the response to thermal neutrons from the Delft 2MW nuclear reactor. Even under zero bias the diode shows a response

esa

Performance limiting effects

1) Crystal purity/stoichiometry

2) Thermal effects

3) Polarization

4) Radiation effects

Crystal purity/stoichiometry - crystal defects

Twins	– grain boundary defect, in which a crystal is joined to its mirror image – size up to ~ mm
Dislocation	– line defect that may run the length of the crystal – size up to ~mm
Grain boundaries	– boundary between two crystals in a polycrystalline solid size up to ~mm
Voids	– macroscopic holes in the lattice - size up to ~mm
Inclusions	– regions of a different phase, size 1-10's of micron
Precipitates	– small regions of a different phase, size up to ~micron

Transport issues related to crystal purity/stoichiometry

Must also be considered when doping and alloying

Actual mobility given by Matthiessen's rule $\Rightarrow 1/\mu = 1/\mu_{lattice} + 1/\mu_{impurities}$

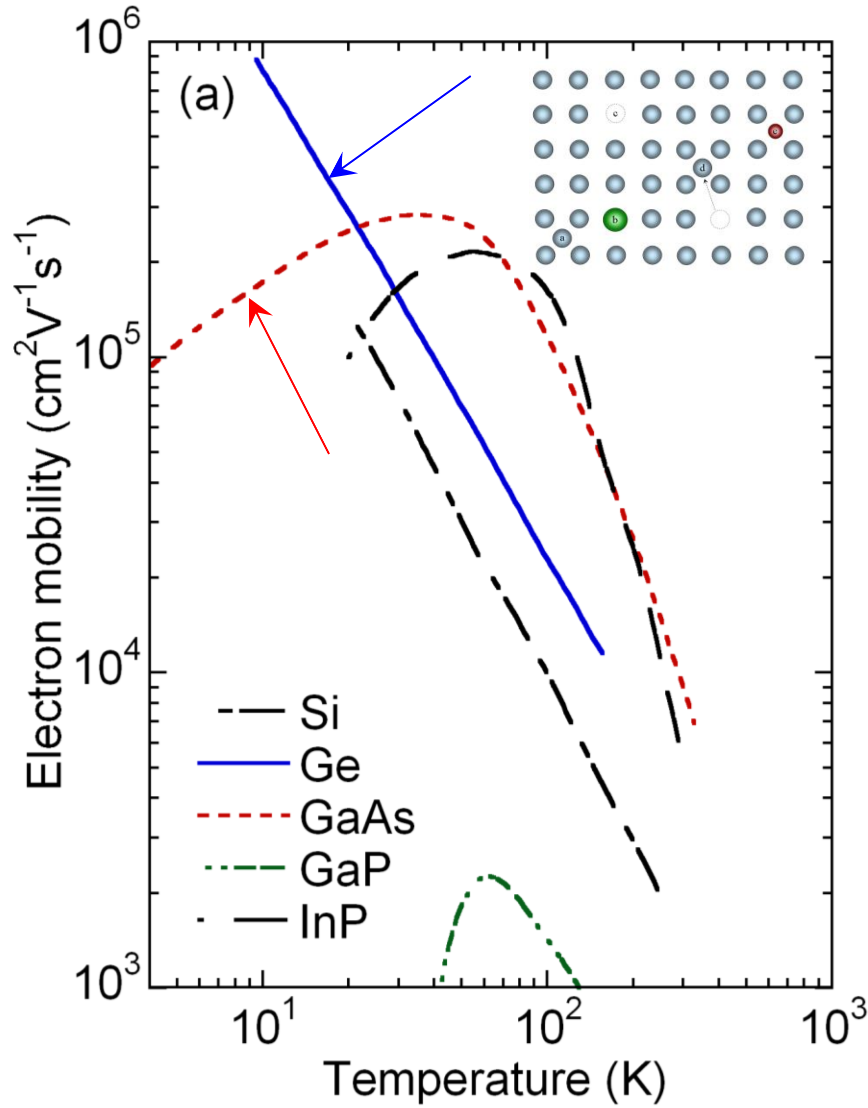

(b)

Hole mobility (cm^{2}V^{-1}s^{-1})

Temperature (K)

Si
Ge
GaAs
GaP
InP

impurity $T^{+3/2}$

lattice $T^{-3/2}$

μ (cm^{2}V^{-1}s^{-1})

10°K 300°K

T(°K)

Effects of inclusions on spectra

ESRF beamline ID15

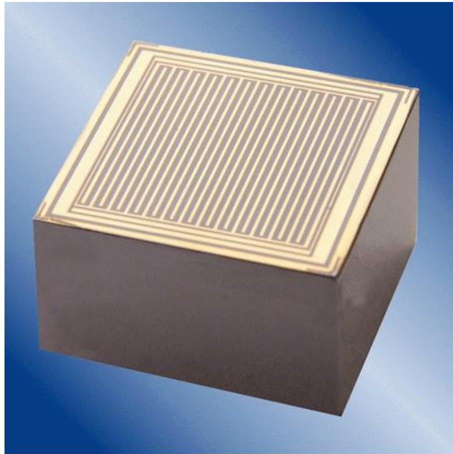

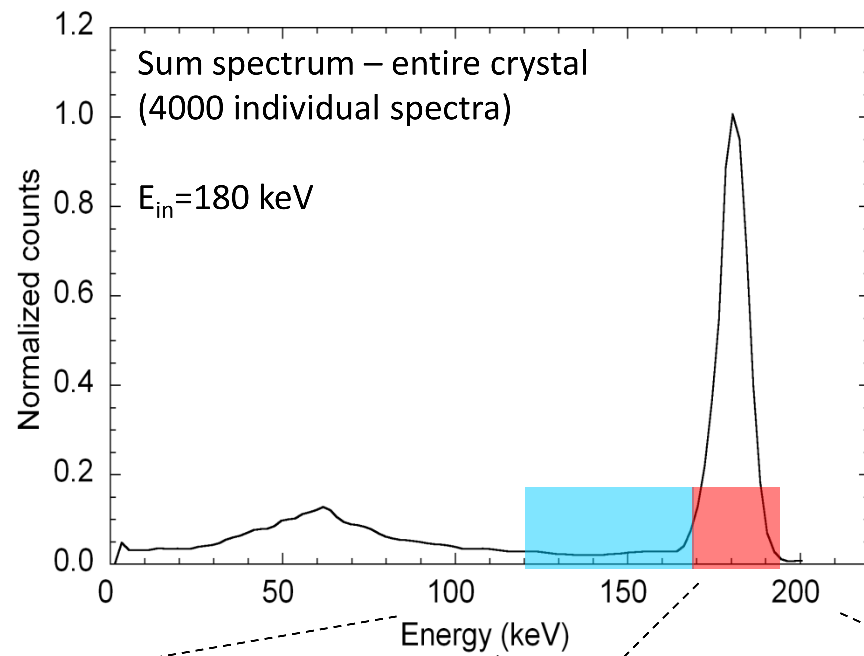

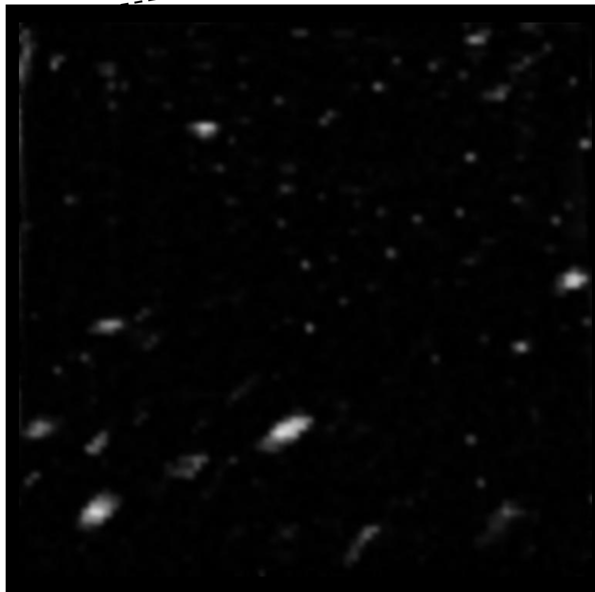

Counts between 120-170 keV

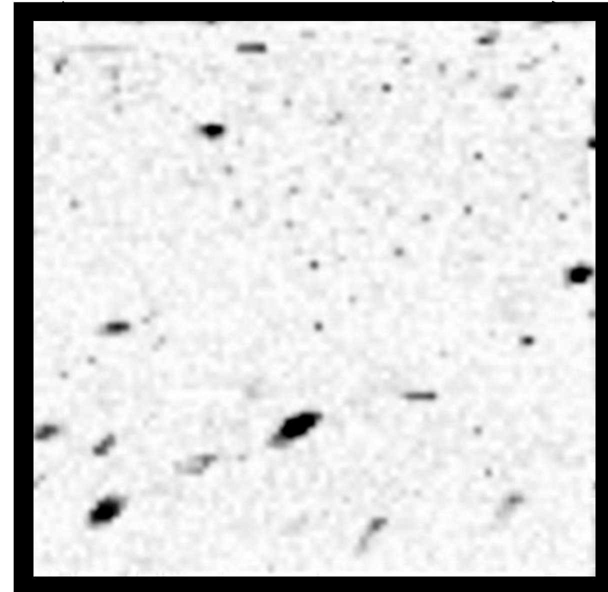

Counts between 170-193 keV

Coplanar grid CZT crystal imperfections

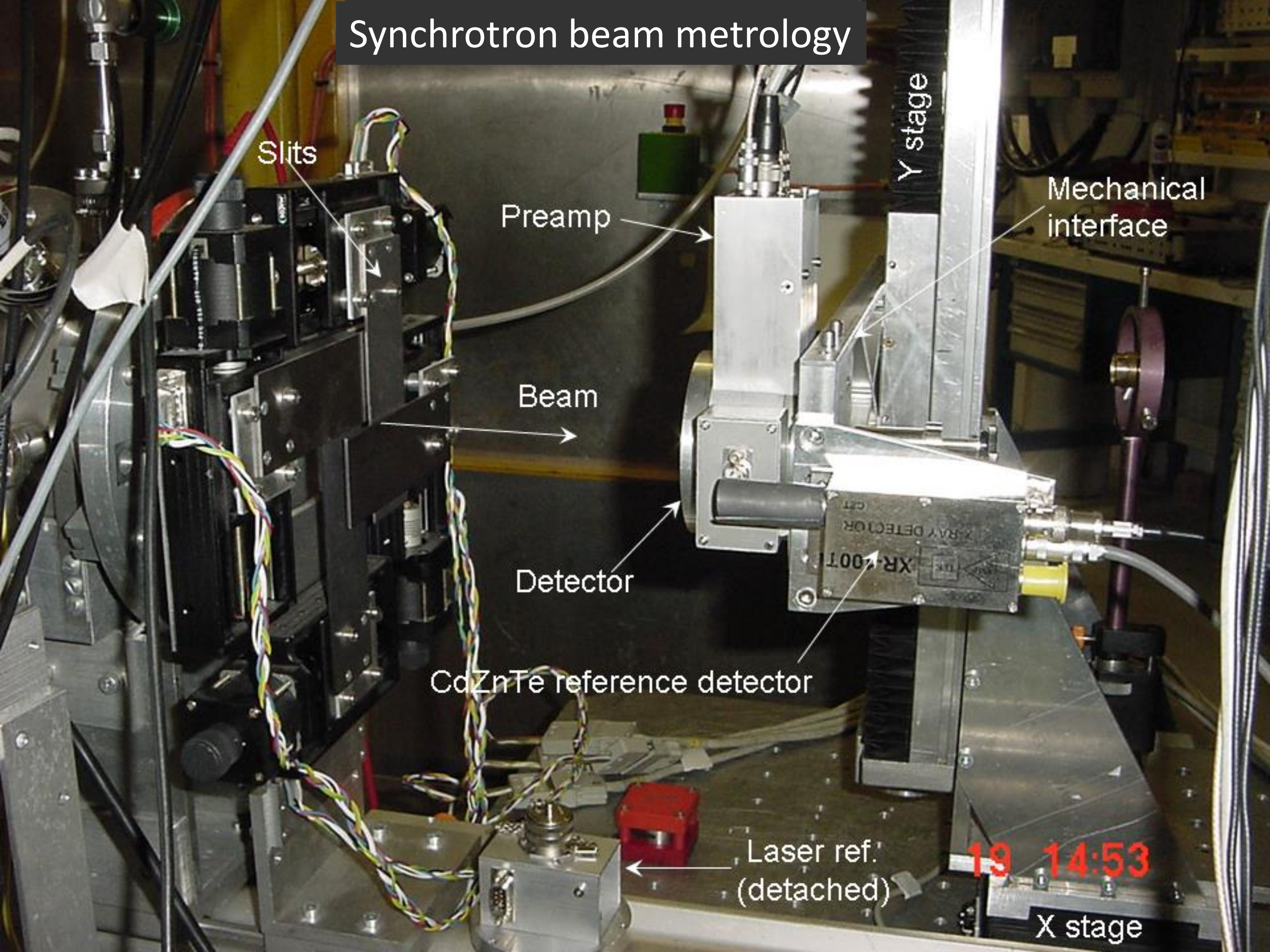
Synchrotron beam metrology
Slits
Preamp
Y stage
Mechanical
interface
Beam
Detector
CdZnTe reference detector
Laser ref.
(detached)
19 14:53
X stage

Crystal defects – precipitates and inclusions

Why do some detectors have worse CCE and resolution than other similar detectors?
The X-ray world with finer spatial resolution

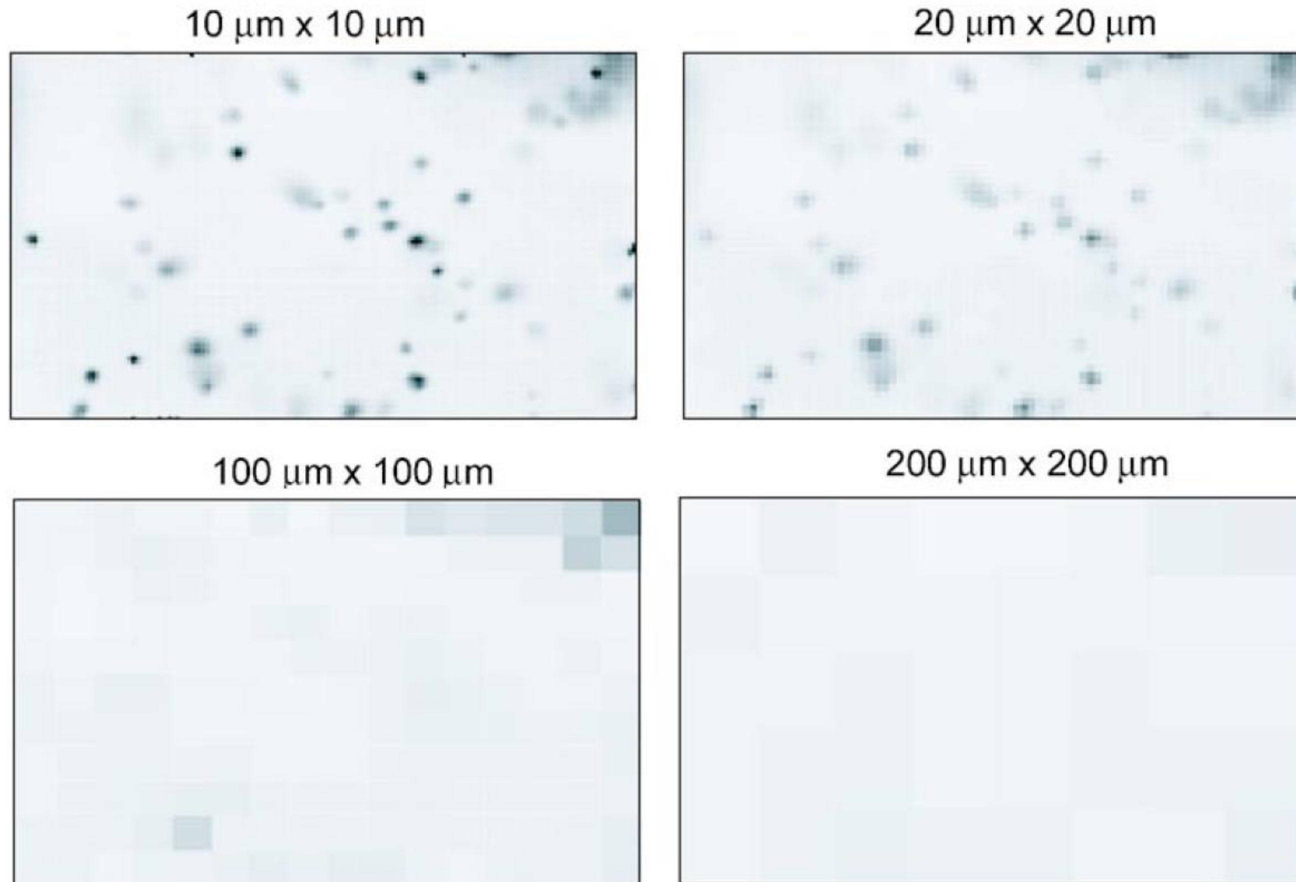

X-ray maps of the same areas of a 1mm thick CdZnTe device at different spatial resolutions

Carini et al., "*Effect of Te precipitates on the performance of CdZnTe (CZT) detectors*," Appl. Phys. Lett., **88** (2006) 143515-1

Precipitates and inclusions - correlations at other wavelengths

Finer spatial resolution

IR micrographs

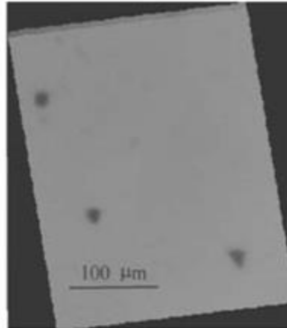

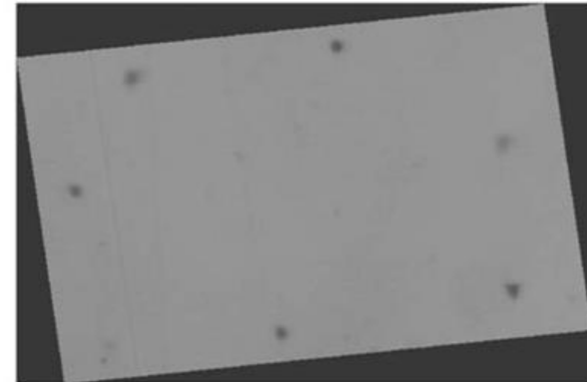

X-ray images

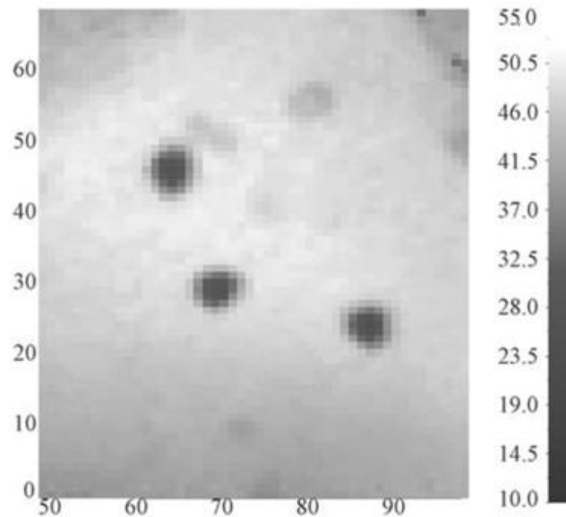

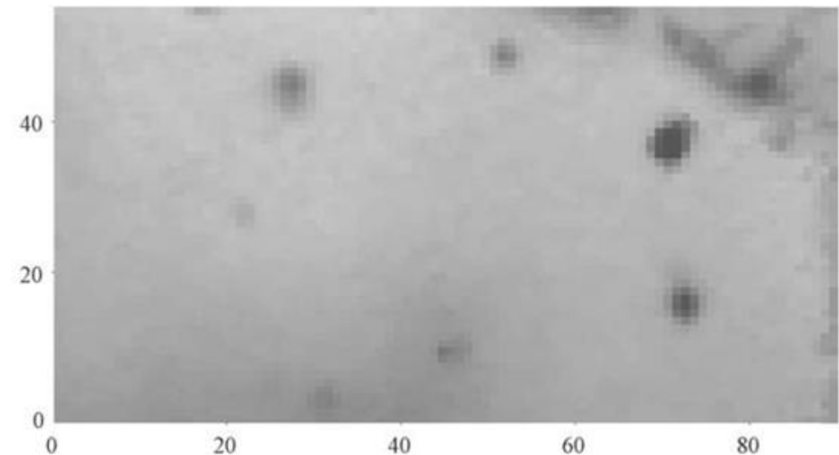

IR and X-ray mages of Te inclusions/precipitates measured in a 1-mm thick CZT crystal. The lower images are X-ray maps when of the crystal when operated as a simple planar detector. The dark spots in this case correspond to a drop in the detector response, demonstrating the link between precipitates and poor device performance. The scans were performed by using a 10×10 μm^2, 85 keV X-ray beam.

Carini, et al., "*Effect of Te precipitates on the performance of CdZnTe (CZT) detectors*," Appl. Phys. Lett., **88** (2006) 143515-1

Defect/performance metrology – IR transmission microscopy

IR system allows "in-depth" images of Te inclusions, collapsed on a single plane from which it is possible to do a 3-D reconstruction of images. Can be used to measure sizes and inclusion concentration.

Example of the crystal with high concentration of Te inclusions. 1.1 x 1.5 x 10 mm^3

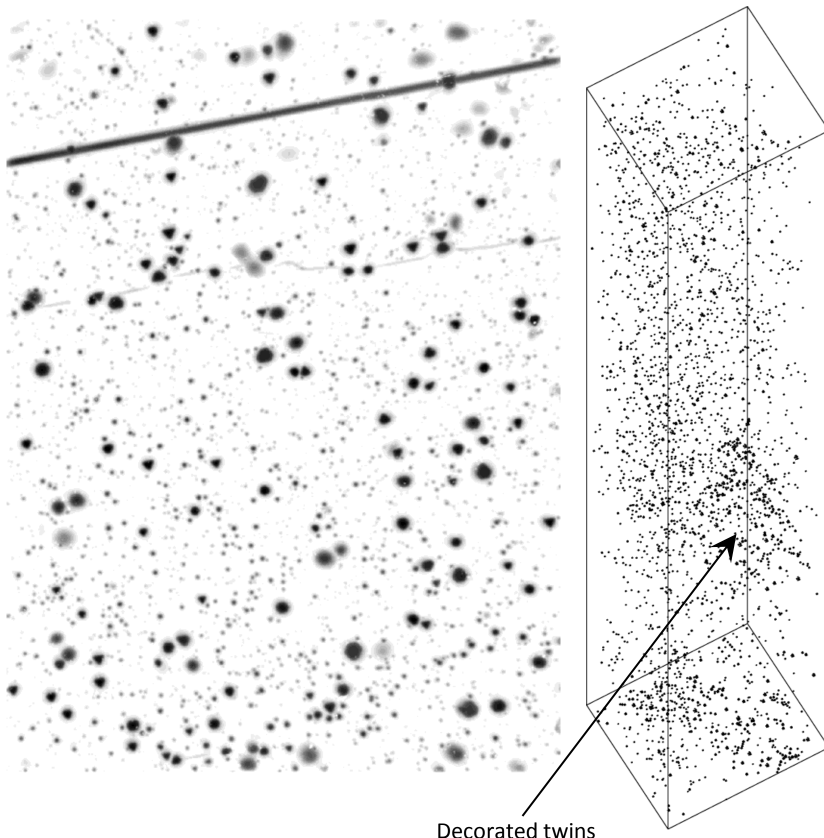

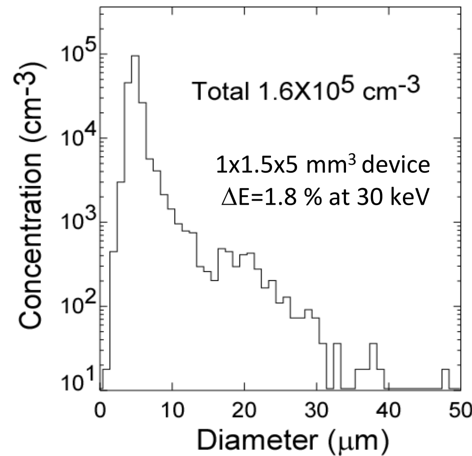

Good detector

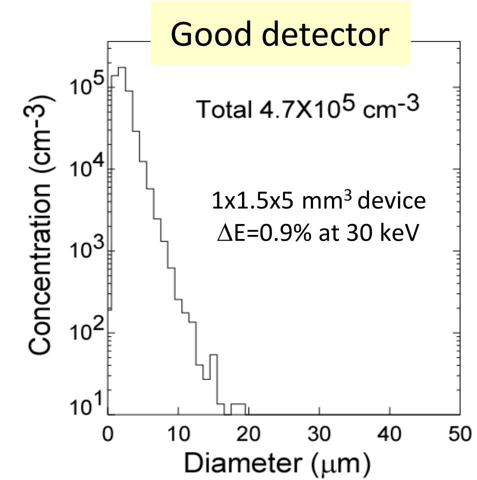

For each inclusion measure x,y,z, and diameter

Plug data into the model to generate X-ray response maps and pulse-height spectra

Currently, the model assumes that Te inclusions are opaque to carriers. It depends on a single adjustable parameter: the ratio between effective and actual size of inclusion

Bolotnikov et al., *Extended Defects in CdZnTe Radiation Detectors*, IEEE Trans Nucl. Sci, 56 (2009) 1775.

Crystal defects – Line defects - dislocations

Edge dislocation

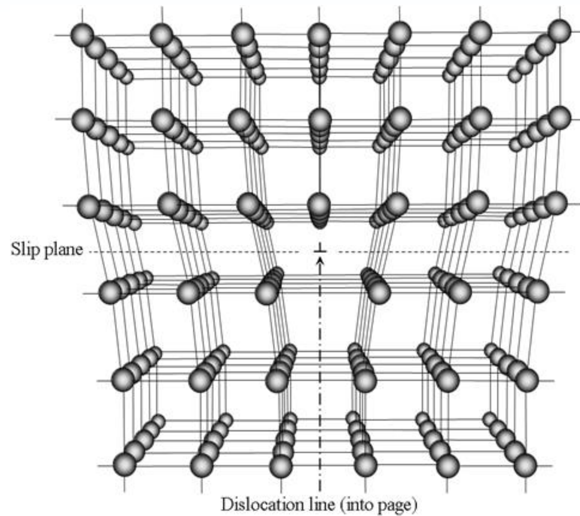

Transmission Electron Microscopy (TEM) image of a large number of dislocations in a quartz crystal.

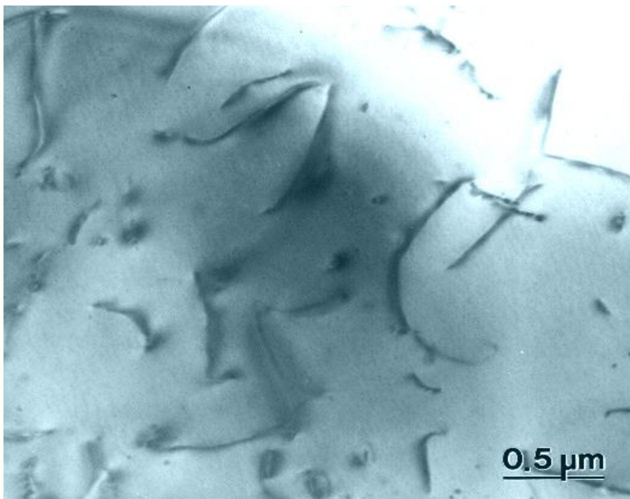

Screw dislocation

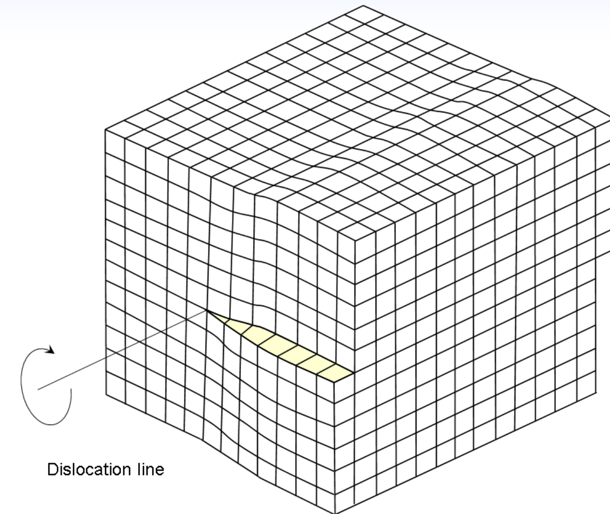

A screw dislocation growth spiral in SiC formed by a shear ripple. The atomic planes perpendicular to it constitute a helicoid, like the thread of a screw.

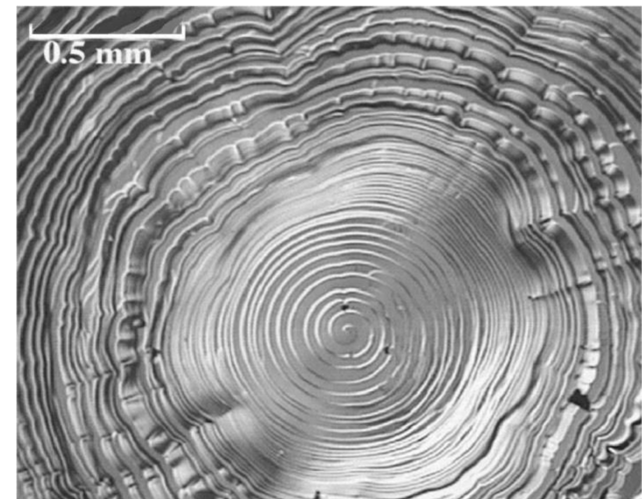

Crystal defects – plane defects

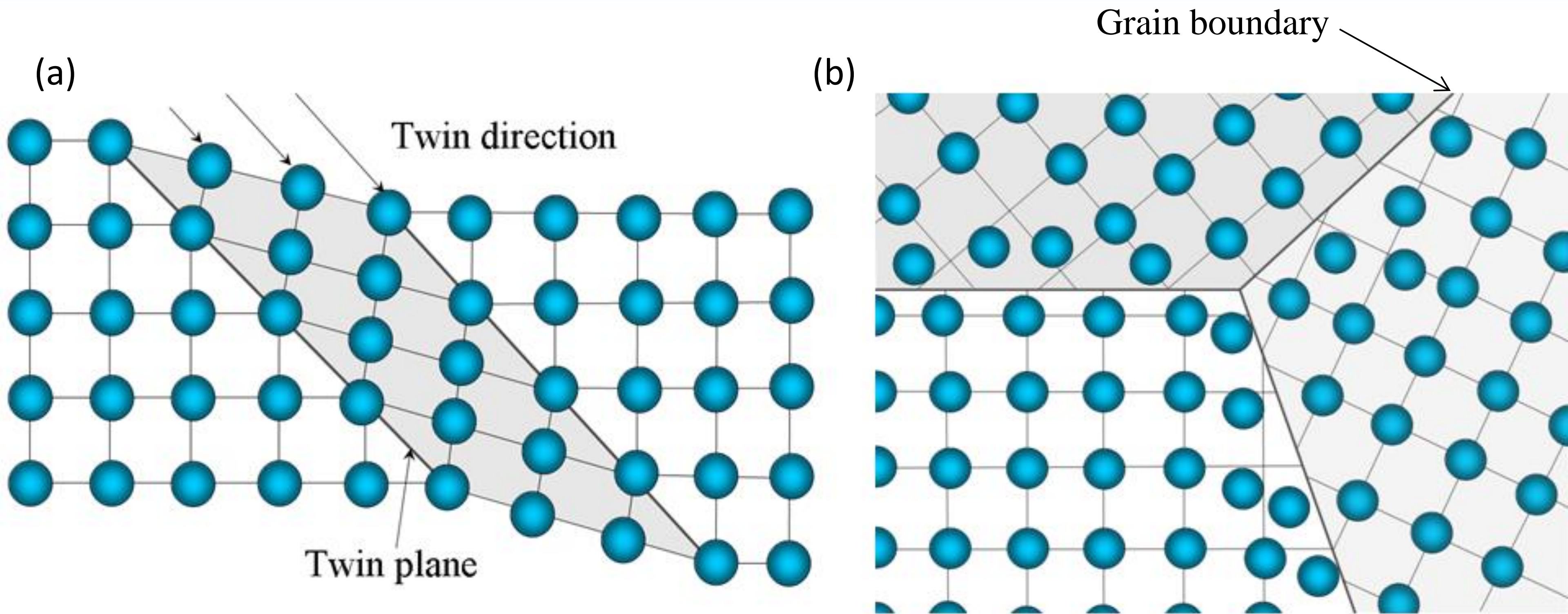

(a) Illustration of a twin region bounded by twin planes or boundaries. Twin boundaries are the most frequently encountered boundaries in many FCC crystals and are in fact a special case of a grain boundary with a high degree of symmetry. (b) grain boundaries between three crystals (grains) of the same phase. The grains differ in mutual orientations.

Plane defects and X-ray performance

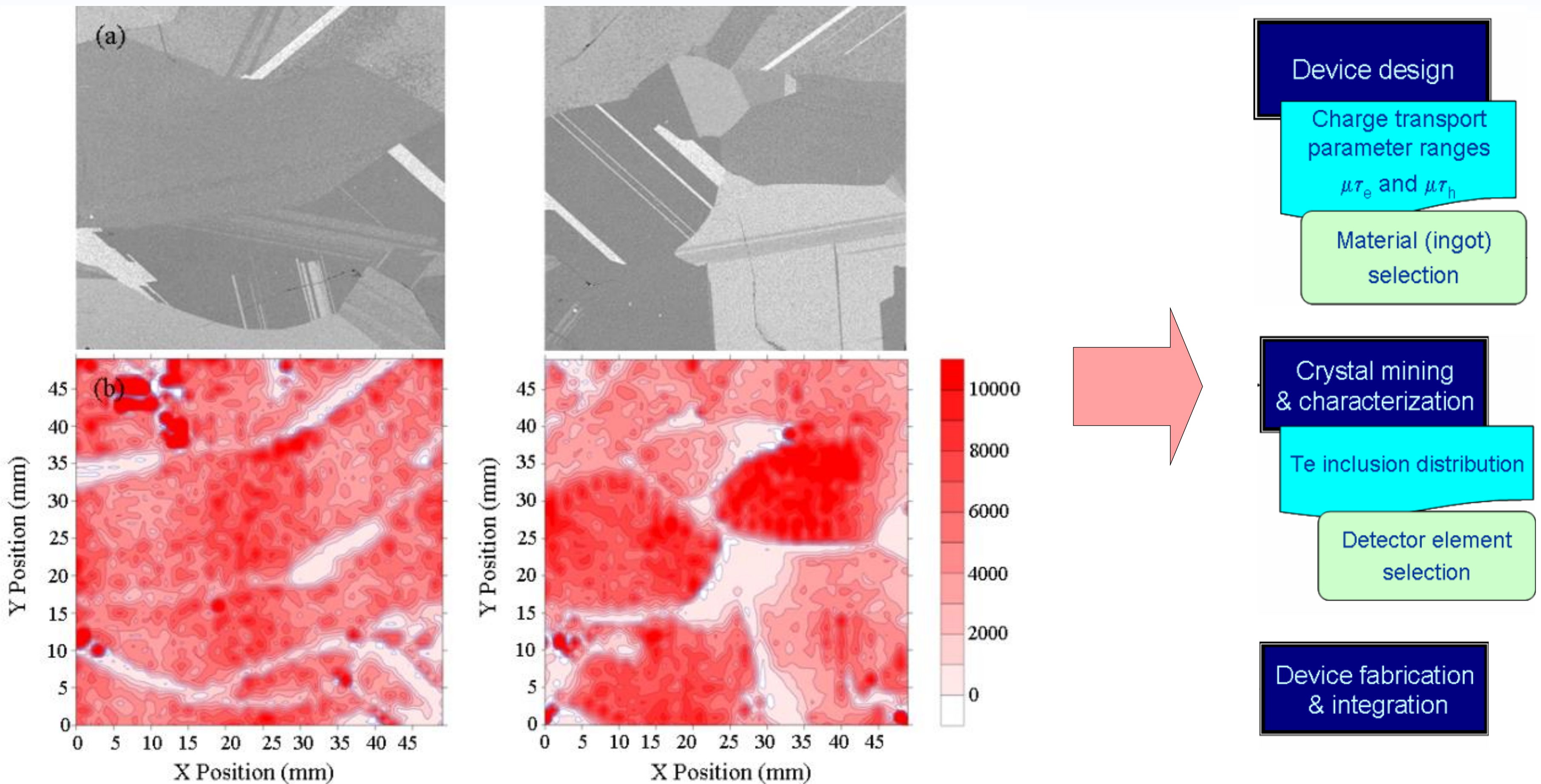

(a) Optical images of two 50 × 50 mm², 3 mm thick slices of a CdZnTe crystal grown by the High Pressure Bridgman method. Numerous grain boundaries and twins are apparent in the image. (b) The crystals count rate response, measured with a ^{57}Co radioactive source is shown in the lower images, illustrating poor charge collection at the grain boundaries. Interestingly, no correlation was found with the numerous twin boundaries observed inside the grains, indicating that twins have a negligible effect on the electric field and charge collection of semi-insulating CdZnTe devices.

Temperature degradation effects

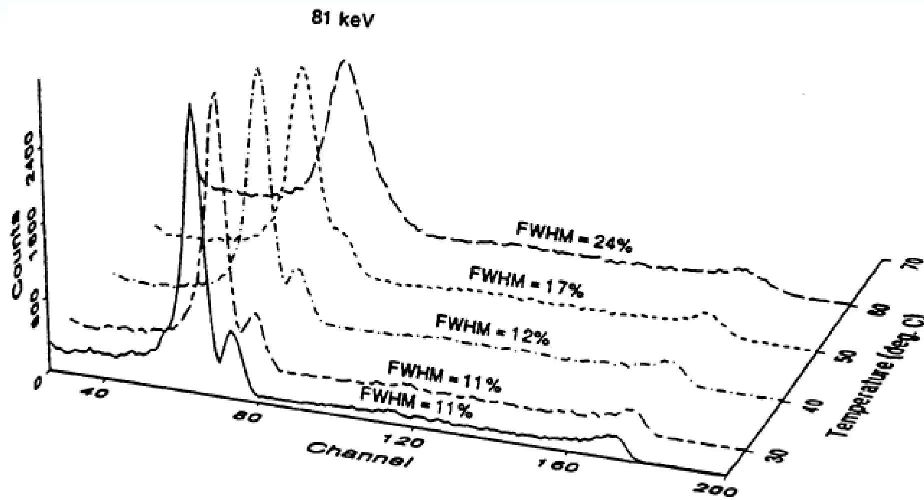

The progressive degradation of spectroscopic performance of a CdZnTe detector with increasing temperature (from Egarievwe, et al., *SPIE*, **2305** (1994) 167).

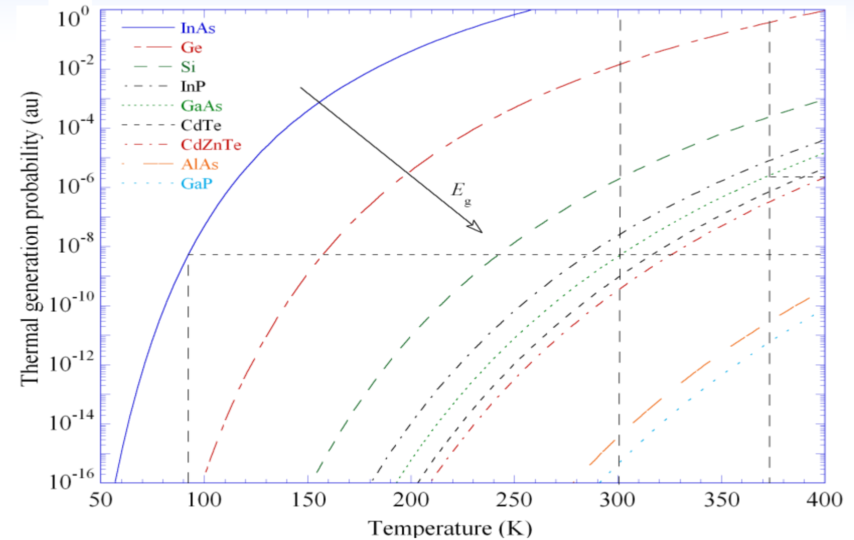

The probability of thermal electron-hole pair generation as a function of temperatures

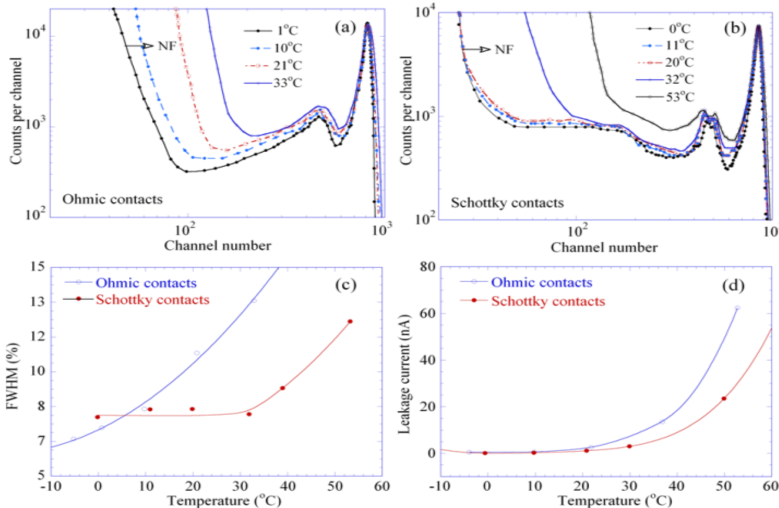

Effects also depend on contacting system

Temperature dependencies

Intrinsic components $P(T) \sim T^{\frac{3}{2}} \exp\left(-\frac{E_g}{2kT}\right)$ $\mu_e \sim 8000\left(\frac{300}{T}\right)^{2.3}$ $\mathrm{cm^2V^{-1}s^{-1}}$

External components – ohmic bulk leakage

$$I(T) \sim T^2 \exp\left(-\frac{E_g(T)}{2kT}\right)$$

with blocking contact leakage

$$I(T) = A^* T^2 \exp\left(-\frac{e\phi_b}{kT}\right)$$

External components – surface leakage

$$I(T) = cT^2 \exp\left(-\frac{\phi_b}{kT}\right)$$

All strong dependencies

Polarization

Time dependent build up of space charge due to mid-level traps (~0.8 eV) $\tau_{ionization} < \tau_{deionization}$

- bias induced - deep acceptor levels (depends on length of time bias applied, not on radiation level (examples, CdTe, HgI_2)
  - ionic conductivity (TlBr, AgCl)
- radiation induced - depends on radiation level and only relevant for high fluxes (examples include CdZnTe)

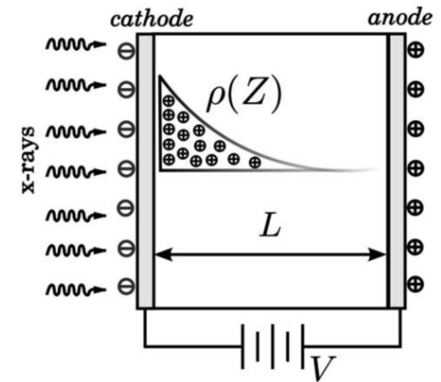

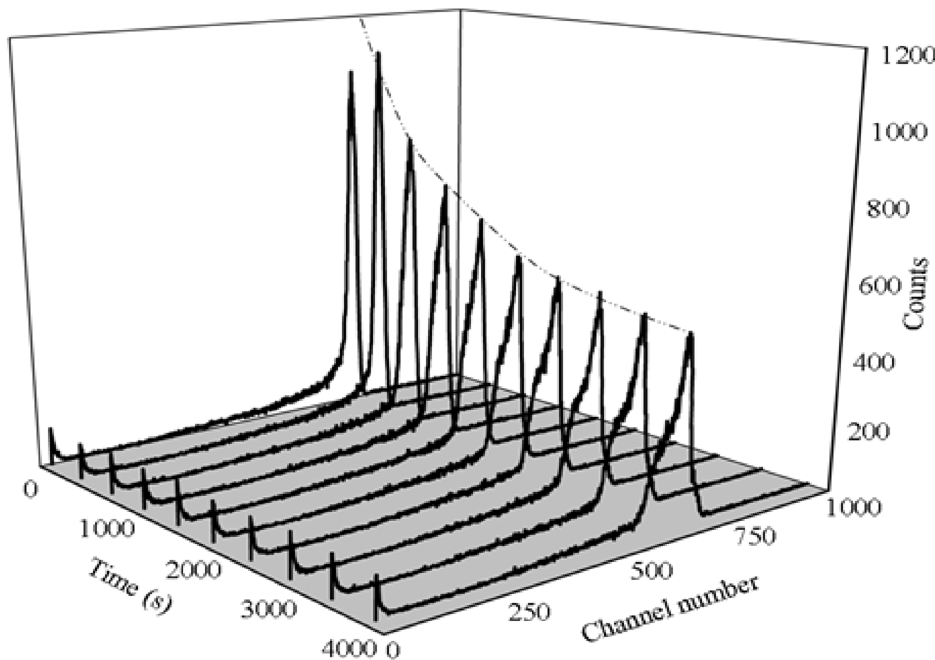

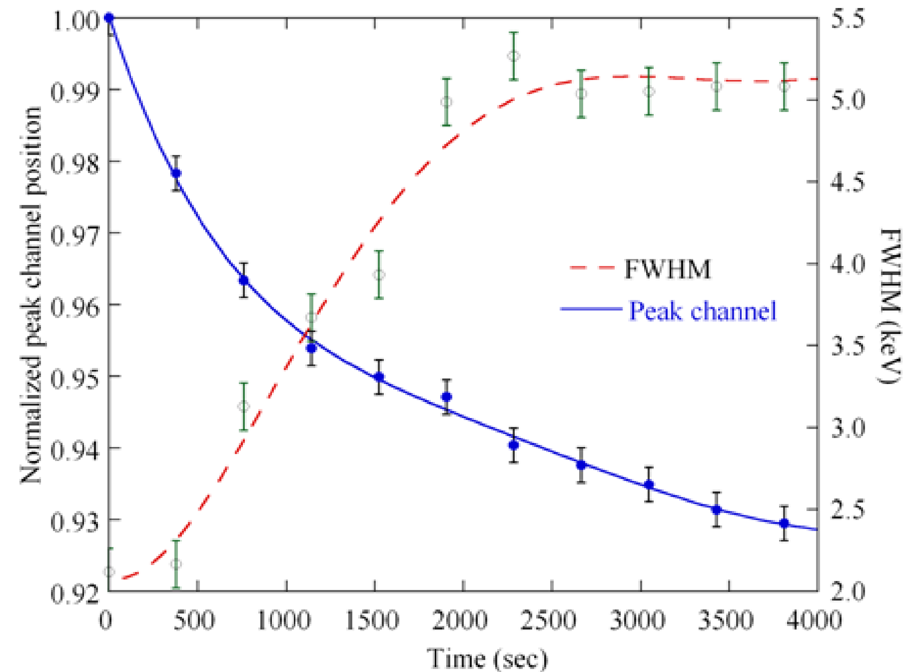

Polarization effects in a 5 × 5 × 2 mm³ TlBr planar detector observed when exposed to a 50mm diameter 60 keV, 1 kHz, synchrotron beam

Radiation effects

a) ionization, in which charged particles ionize the atoms in a device causing an instantaneous release of charge. In bulk materials this charge dissipates by either diffusion or drift in an electric field. However, in structured devices the build-up of localized charge can damage devices - particularly in the vicinity of an interface.

b) displacement, in which a device atoms are literally displaced and removed from their equilibrium positions introducing disorder into the crystal lattice structure. The consequences are the introduction of additional energy levels into the band gap which act as trapping and generation/ recombination centers, altering the semiconductors electronic properties.

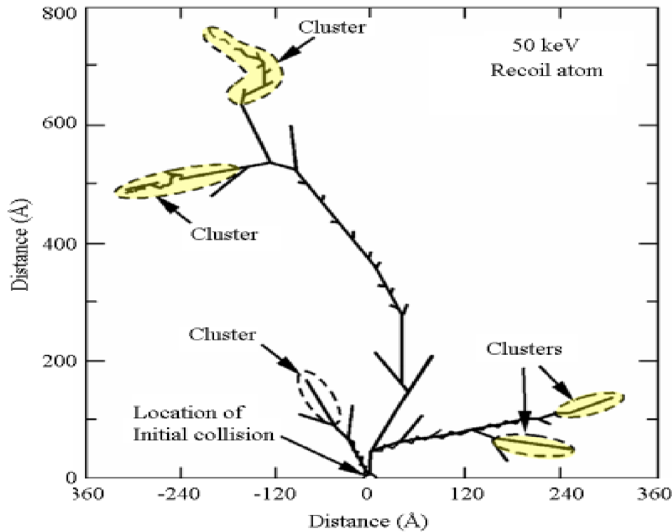

Displacement damage in Si for the case where the energy transferred to the lattice site is more than 10^3 times greater than the displacement threshold energy The displaced atom can initiate a “cascade”, displacing many thousands of atoms.

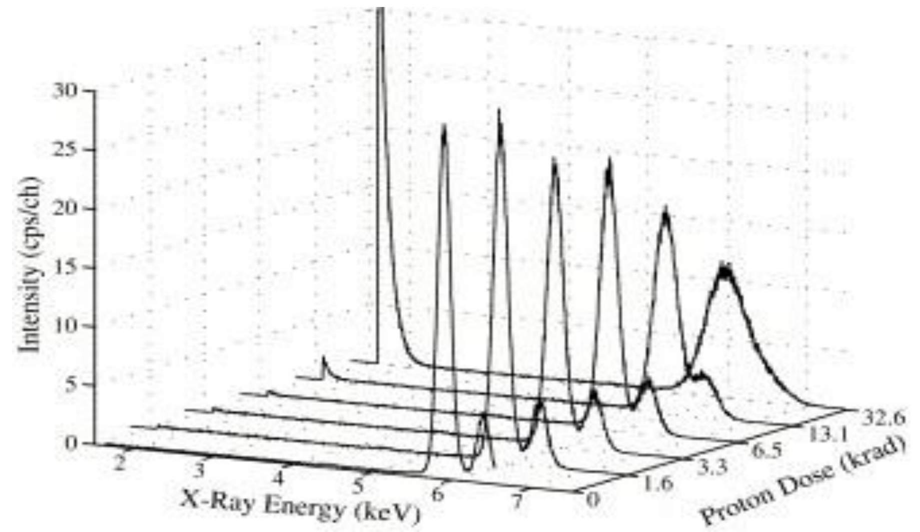

X-ray spectra for the irradiated and non-annealed Si pin-detectors (shaping time 6 μs), after each proton exposure. A severe degradation in the energy resolution is already observed for proton doses of the order of 5–10 $krad_{(Si)}$(Si).

The factors affecting the calculated absorbed dose. For inter-comparison we list the absorbed doses for a proton irradiation of 2.66×10^9 p cm s^{-1}. The data are ranked by the product of the average nuclear charge and atomic density. The last column gives the “Tolerance” index for each of the materials , which does not track the absorbed dose.

Compound	Bandgap eV	Atomic density cm^{-3}	Av. Nucl. Charge	Product cm^{-3}	Absorbed dose krads	Tolerance
CdZnTe	1.57	1.57×10^{22}	109.5	17.15×10^{23}	0.23	5
TlBr	2.68	1.60×10^{22}	53.2	8.52×10^{23}	0.60	3‡
HgI_2	2.13	0.84×10^{22}	92.1	7.81×10^{23}	1.05	1
GaAs	1.43	2.21×10^{22}	32.0	7.08×10^{23}	2.00	2
InP	1.35	1.98×10^{22}	27.1	5.38×10^{23}	1.31	4†
Si	1.12	4.97×10^{22}	5.29	2.63×10^{23}	2.00	6

‡moved from 2nd position to 3rd because of much increased polarization effects.

†moved to 4th because of its very poor initial energy resolution and its electronic and structural similarity to GaAs.

Radiation damage - mitigation techniques

- Cooling
- Annealing
- Electronic

Annealing

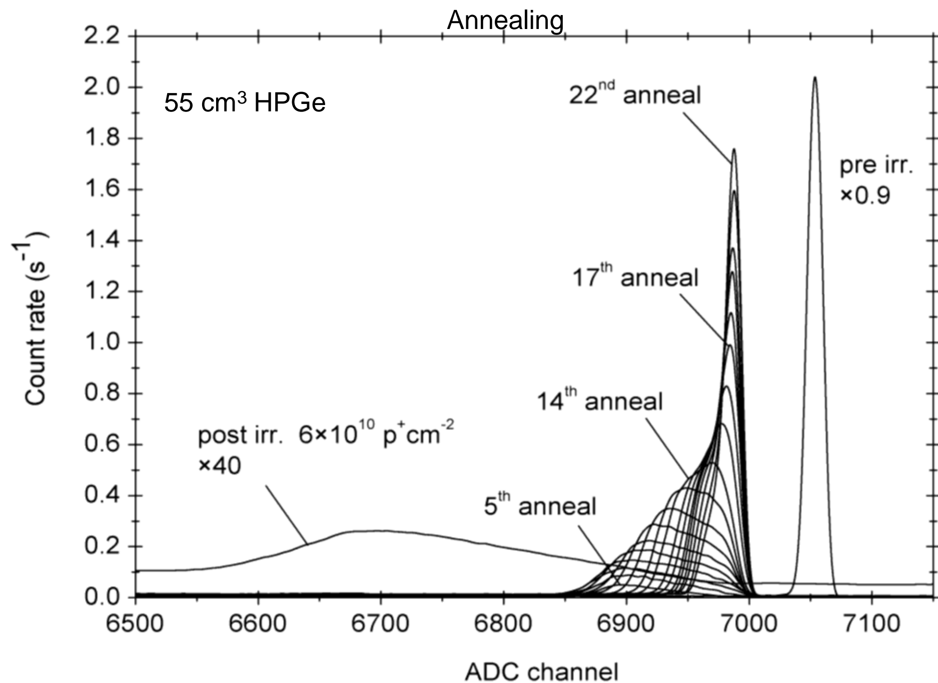

Radiation damage and subsequent annealing in a 55 cm³ HPGe measured at 1332 keV after an irradiation of 6 × 10^{10} protons cm^{-2}. The pre-irradiation peak is offset in channels for clarity. The detector was multiply annealed at 100ºC in block periods of 7 days. The restoration of the detectors performance to with 10% of its initial values took 4.5 months of annealing.

Cooling

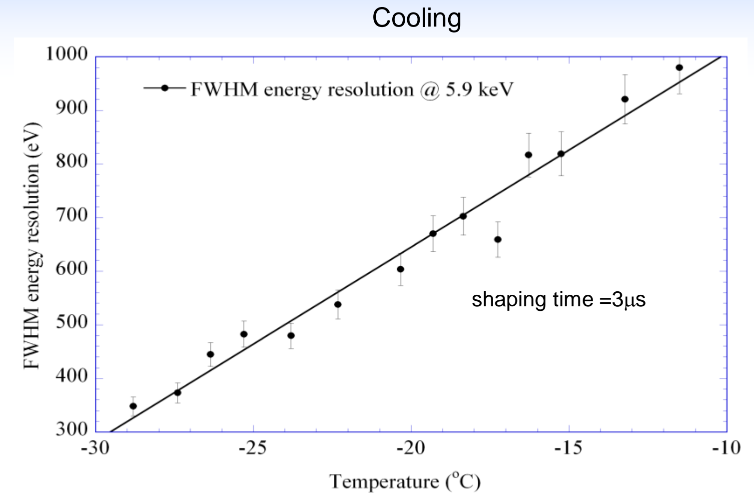

The effect of cooling on spectroscopic performance of a radiation damaged 3 mm² Si PIN diode. The total absorbed non-ionizing dose was 13 rads. The initial undamaged energy resolution measured at a temperature of -20ºC was 280 eV FWHM.

Electronic measures

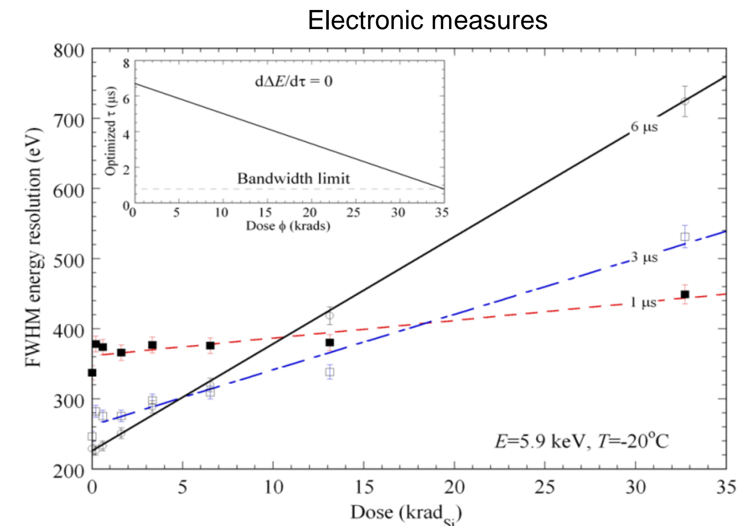

The X-ray energy resolution of a 3 mm², 500 μm thick, Si PIN-detector evaluated for three shaping time constants as a function of proton dose (krads equivalent into Si)

Improving performance - single carrier sensing

- Risetime discrimination
- Hemispherical geometries
- Frisch grid/ ring
- Small pixel effect
- Drift strip
- Ring drift
- Coplanar grid

However, we need a difference of ~ a factor of 10 in the mu-tau products to be effective

Risetime discrimination technique

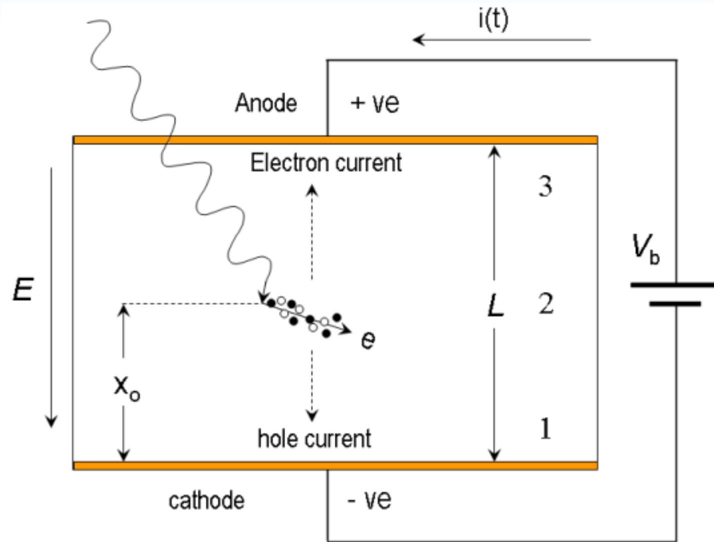

$$t_e = \frac{L}{\mu_e E} \qquad t_h = \frac{L}{\mu_h E}$$

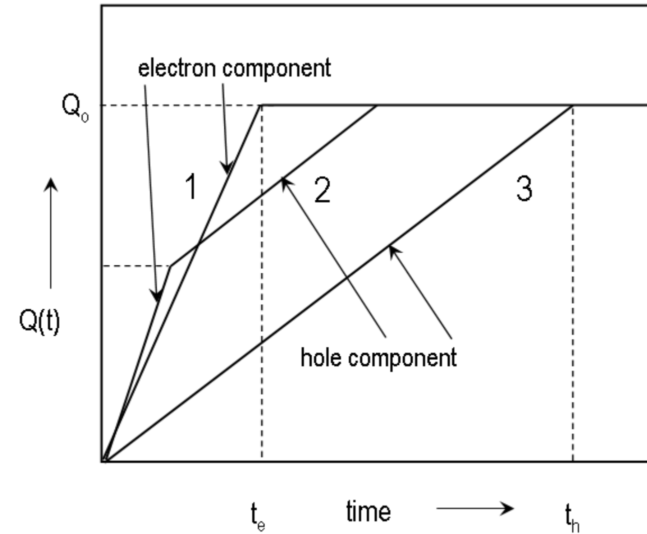

$$i = \frac{dQ}{dt} = q\vec{v} \cdot \vec{E}_w$$

$$I_{eo} = Q_o\left(\frac{\mu_e E}{L}\right) \qquad I_{ho} = Q_o\left(\frac{\mu_h E}{L}\right)$$

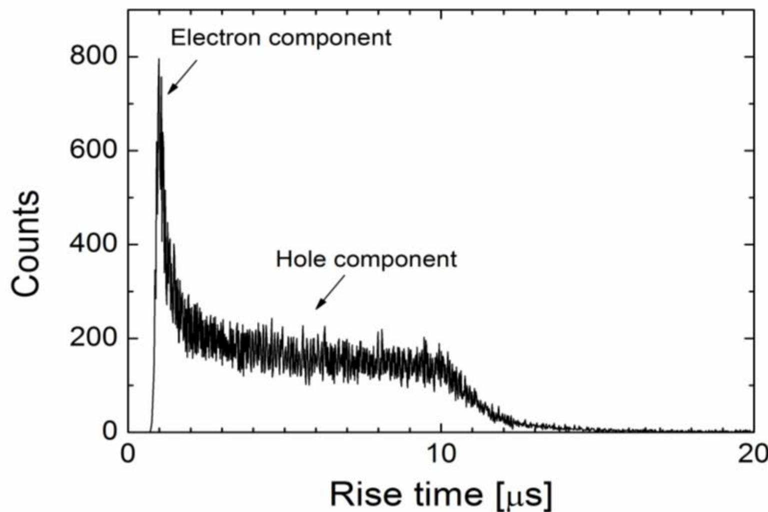

Tada et al., Nucl. Instr. and Meth., Vol. **A638** (2011) 92

When $\mu_e >> \mu_h$ the current pulse induced by the electrons will have a much larger amplitude and shorter duration than that induced by the holes. For interactions in the bulk of the detector, the induced signal will be a composite of electron and hole components whose relative strengths will now depend on the depth of the interaction. In RTD methods, all pulses whose risetime exceeds a pre-set threshold are rejected - in fact, those events that would normally lie in the tail.

Jordanov, Nucl. Instr. and Meth., Vol. **A380** (1996) 353

Risetime discrimination 3 × 3 × 2 mm^3 CdZnTe detector

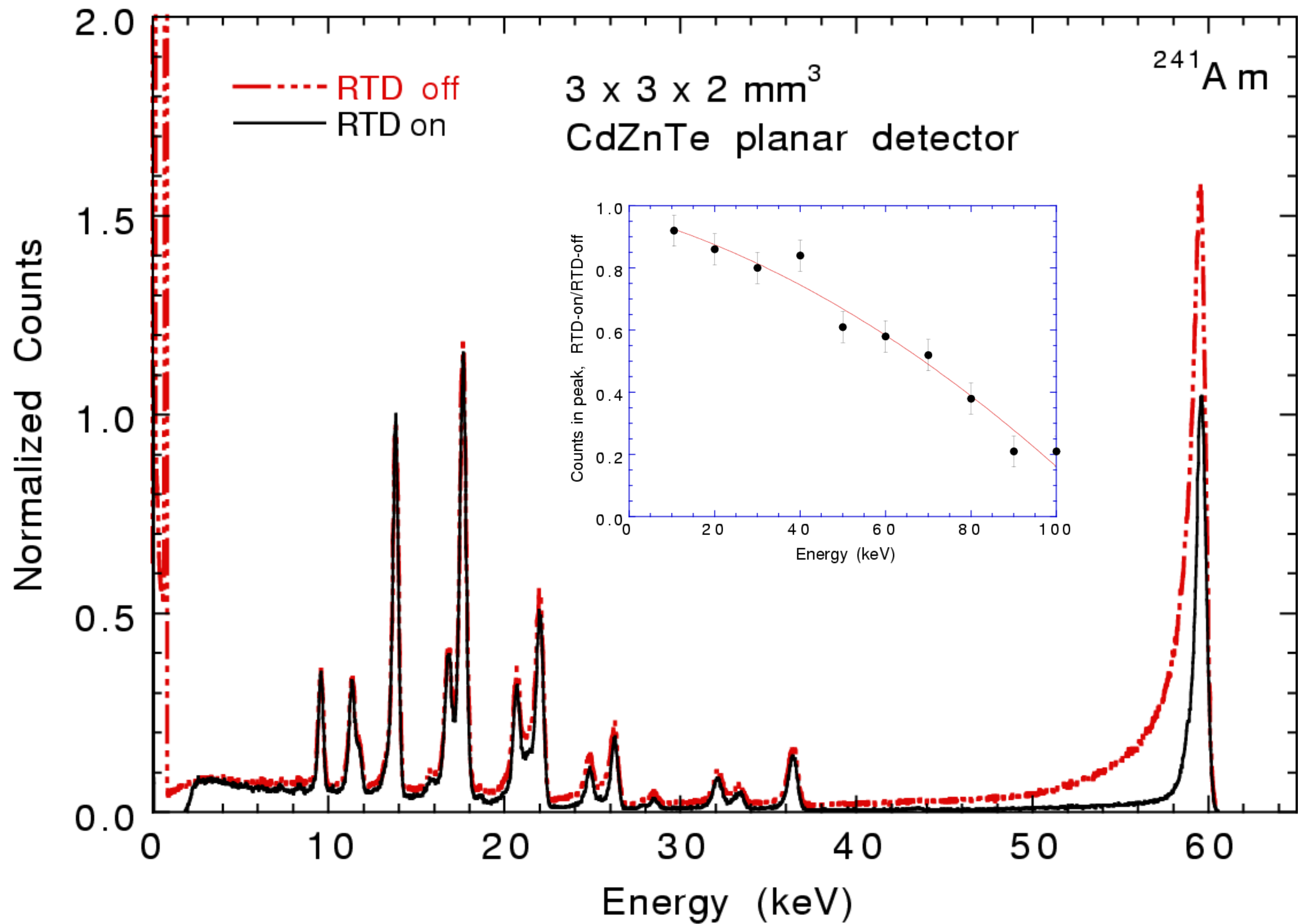

Hemispherical detectors

$$dQ = (q/V)\,E(r)\,dr$$

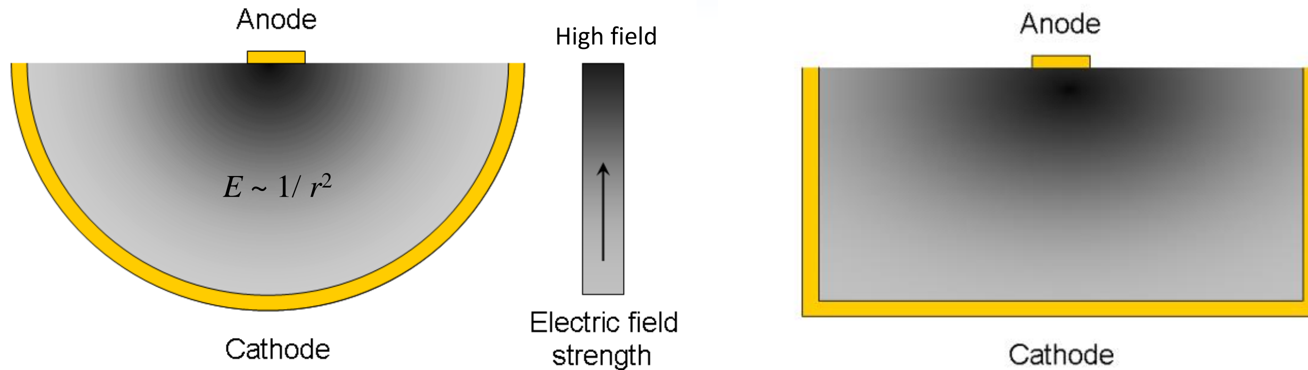

Distribution of the equipotential field lines in hemispherical (left) and pseudo-hemisphere (right) detector geometries.

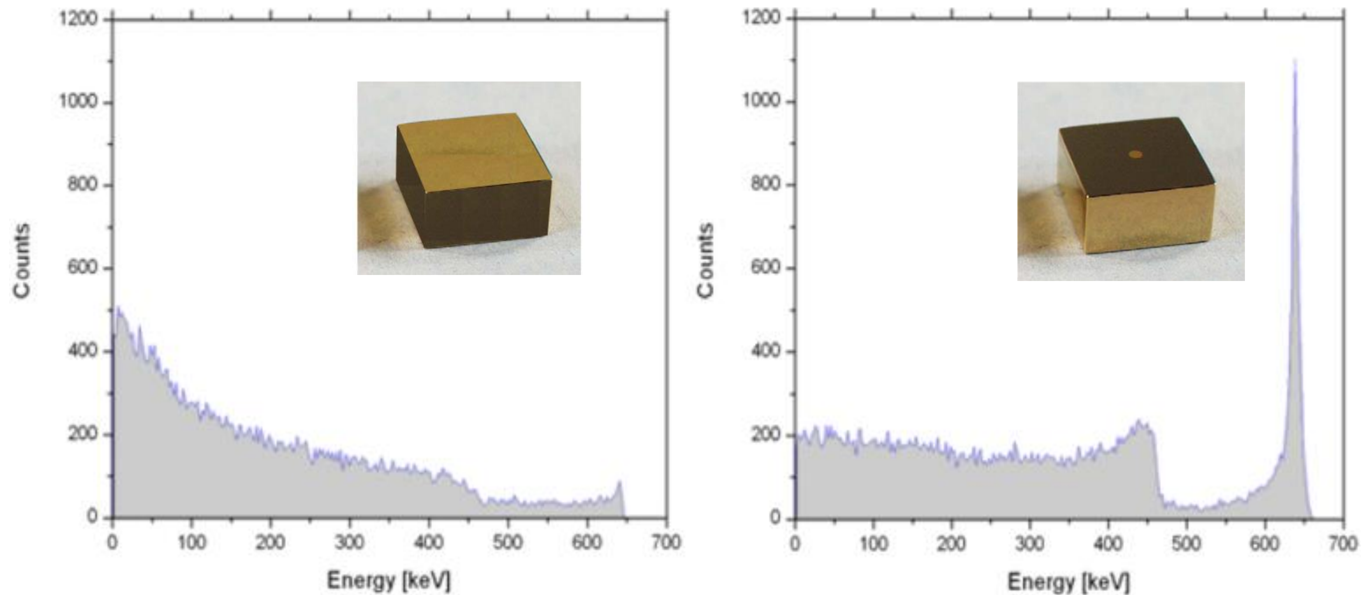

Comparison between the spectroscopic capabilities of a simple planar detector and a quasi hemispherical CZT detector of the same size (10×10×5 mm^3). Left: a simulated ^{137}Cs spectrum for a planar detector. Right: simulated ^{137}Cs spectrum for a quasi-hemispherical detector (Bale and Szeles [13]).

Frisch grid/ring detectors

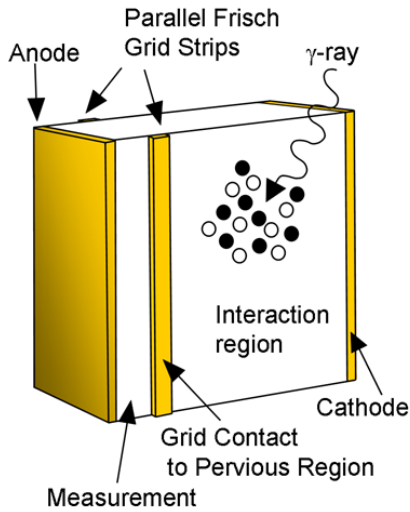

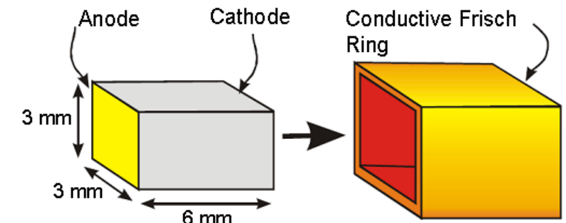

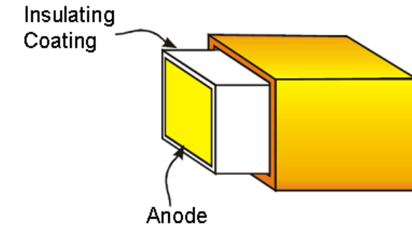

Two implementations of the Frisch-grid concept. Left: two parallel contact strips are fabricated on the sides of the detector between the anode and cathode planes and act as a pseudo-Frisch-grid. Charge carriers are excited in the interaction region and the electrons are drifted through the parallel grids by an applied electric field. Right: schematic of a capacitively coupled Frisch grid detector

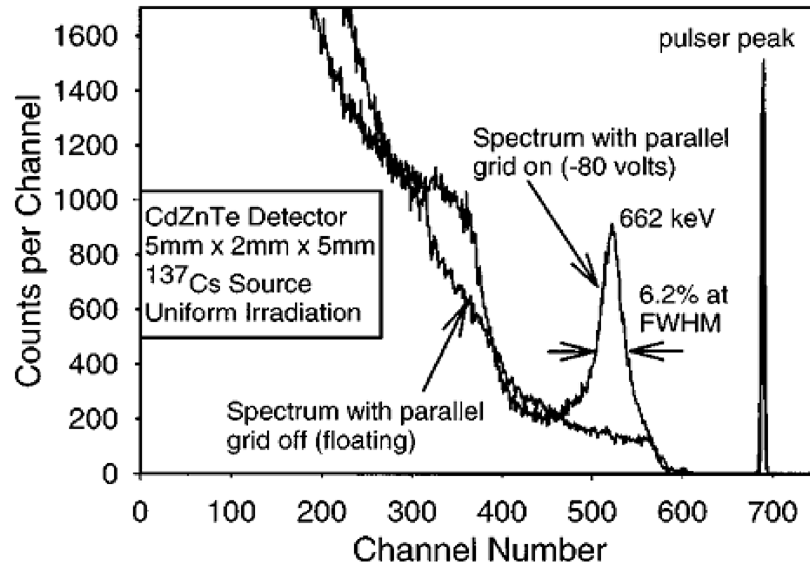

Response of a 5×2×5 mm^3 CZT Frisch grid detector to a ^{137}Cs radioactive source under full area illumination. Spectra are shown with the grid turned off and on. A full energy peak of 6.2% FWHM at 662 keV is achieved with the grid activated (McGregor et al., Appl. Phys. Lett., **65** (1994) 2884).

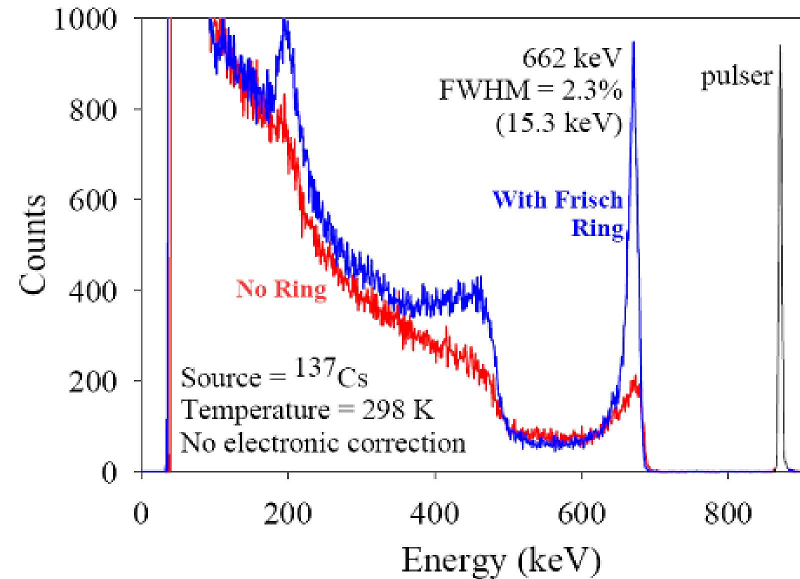

^{137}Cs spectra from a 3×3×6 mm^3 CdZnTe device with a 5 mm insulated capacitively coupled Frisch ring. With the ring connected, the FWHM energy resolution is 2.3% at 662 keV (McNeil et al., Appl. Phys. Lett., **84** (2004) 1988).

Small pixel - near field effect

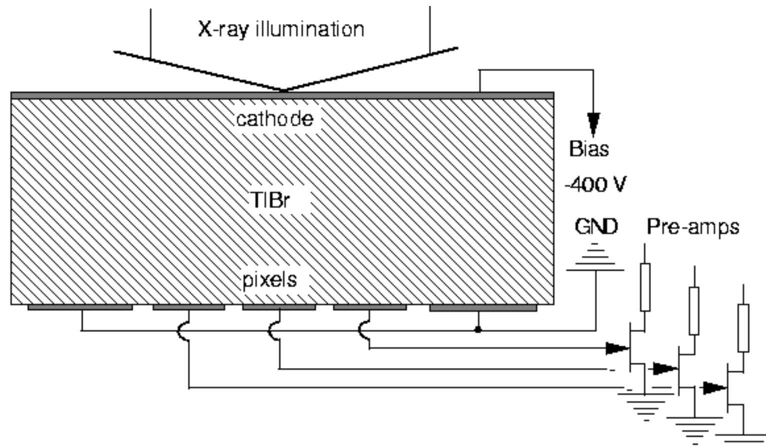

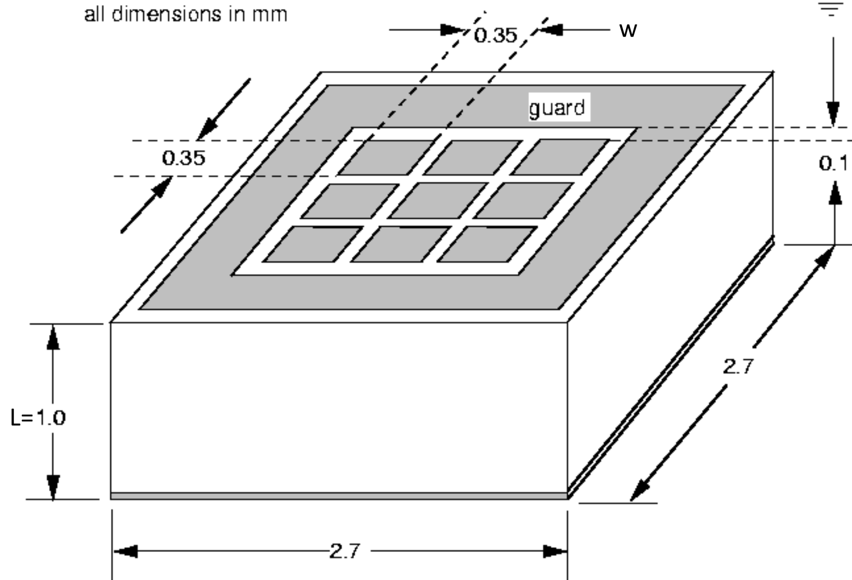

Weighting potential distributions

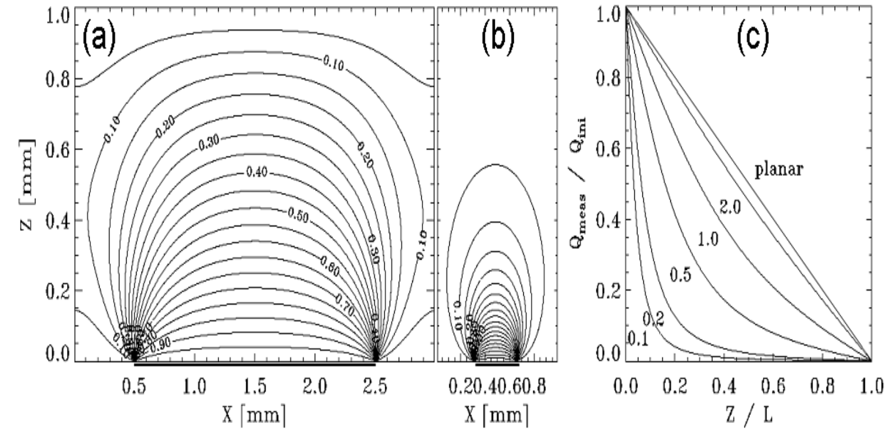

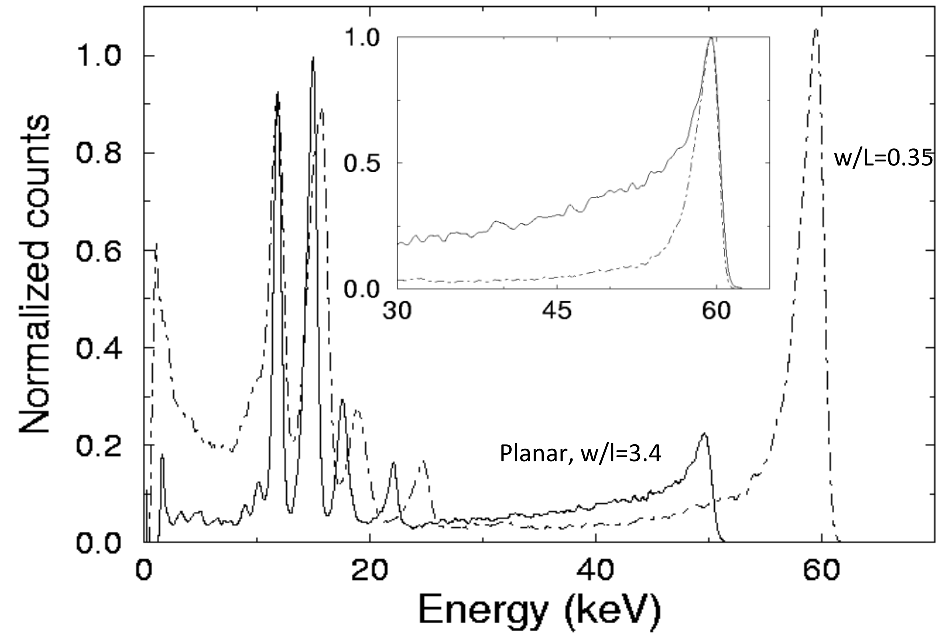

Other schemes

Drift-strip

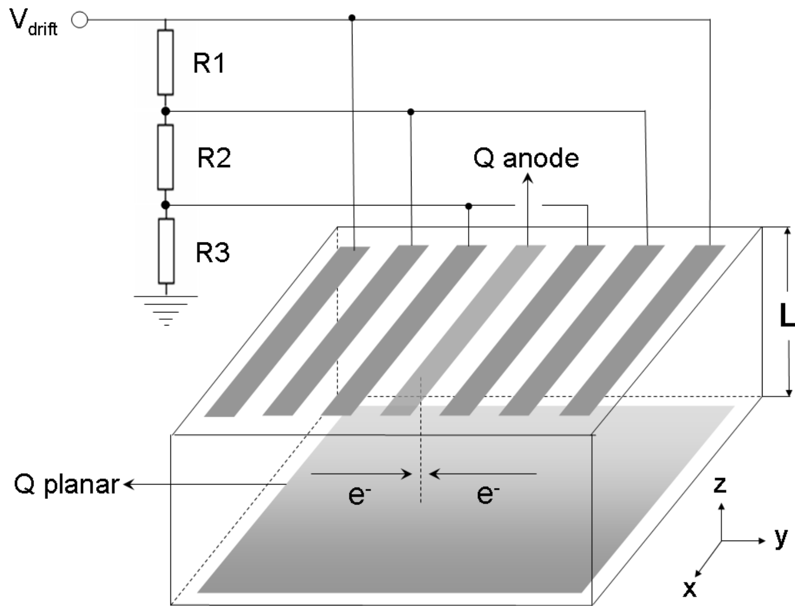

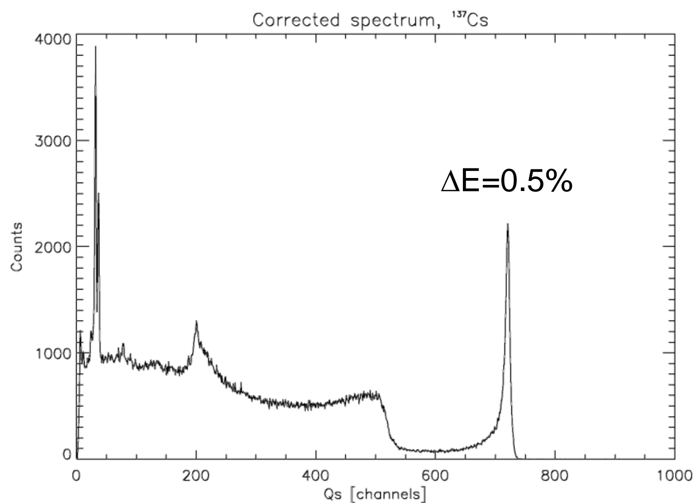

Ring drift

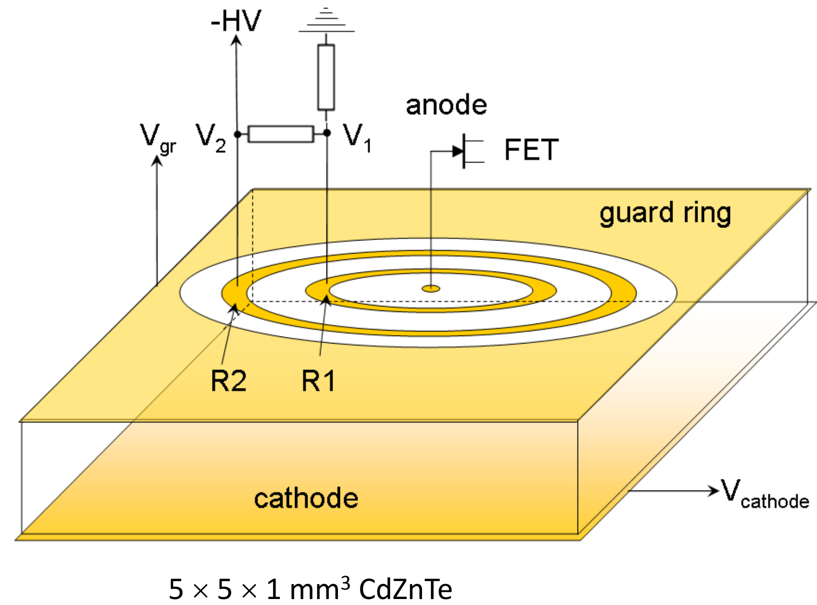

$5 \times 5 \times 1$ mm³ CdZnTe

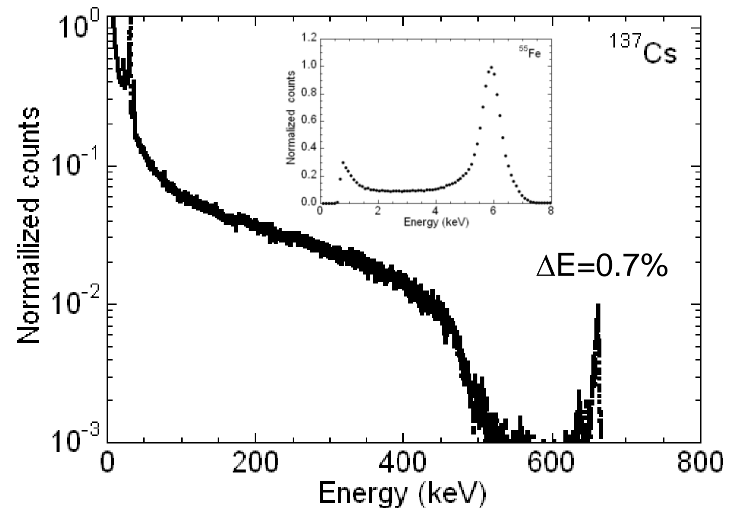

Kuvvetli, et. al., Rad. Phys. and Chem., Vol. **61** (2001) 457.

Owens et al., J. Appl. Phys. Letts., Vol. **102** (2007) 054505-1–054505-9

Coplanar grid technique

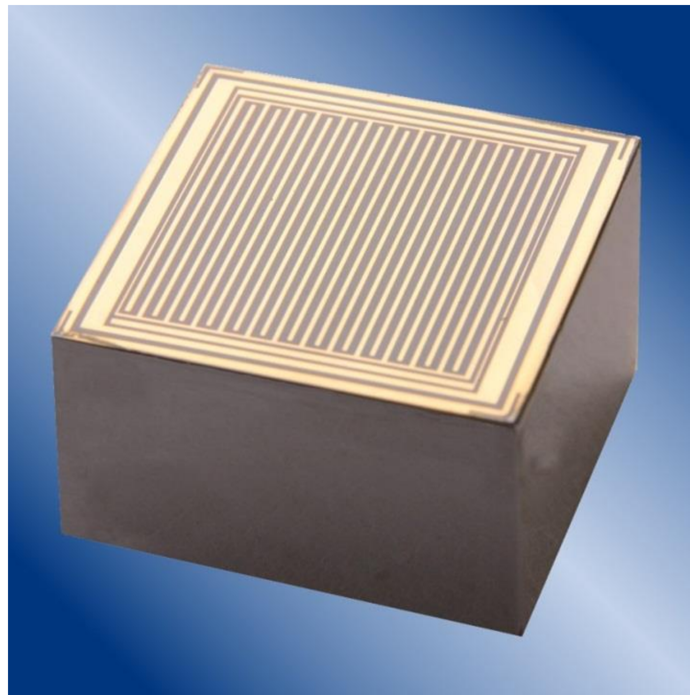

Luke, IEEE Trans. Nuc. Sci., Vol. **NS-42** (1995) pp. 207–213

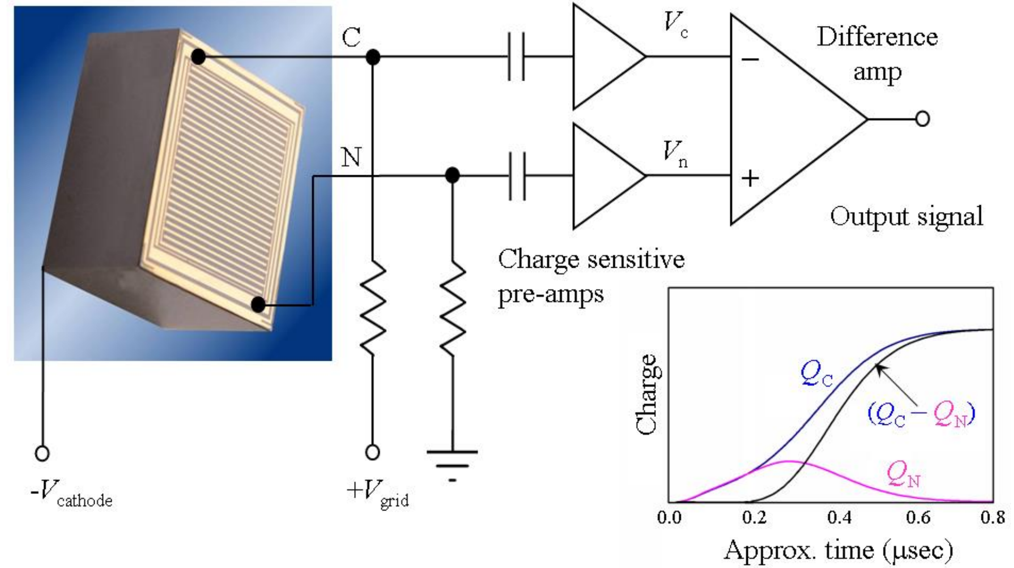

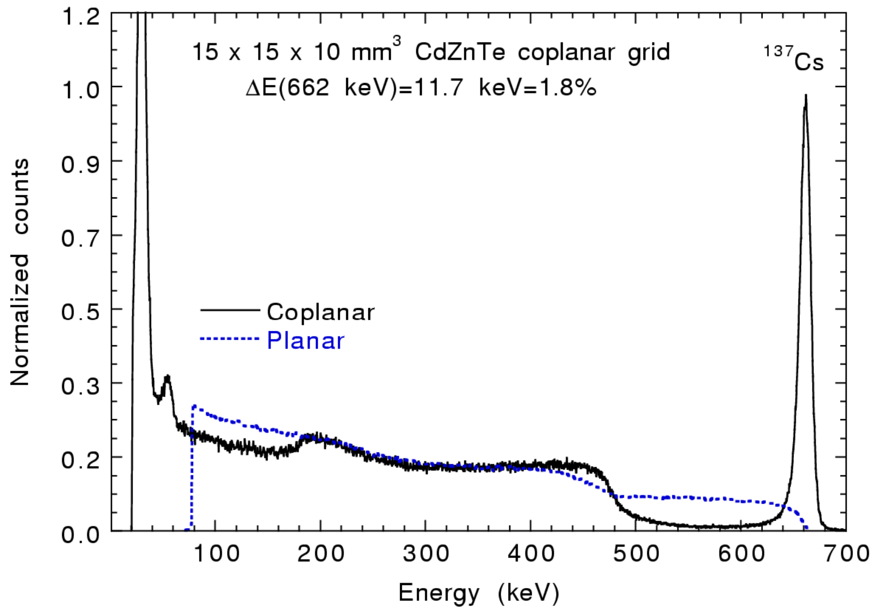

A. Owens, Nucl. Instr. and Meth., Vol. **A563** (2006) 242

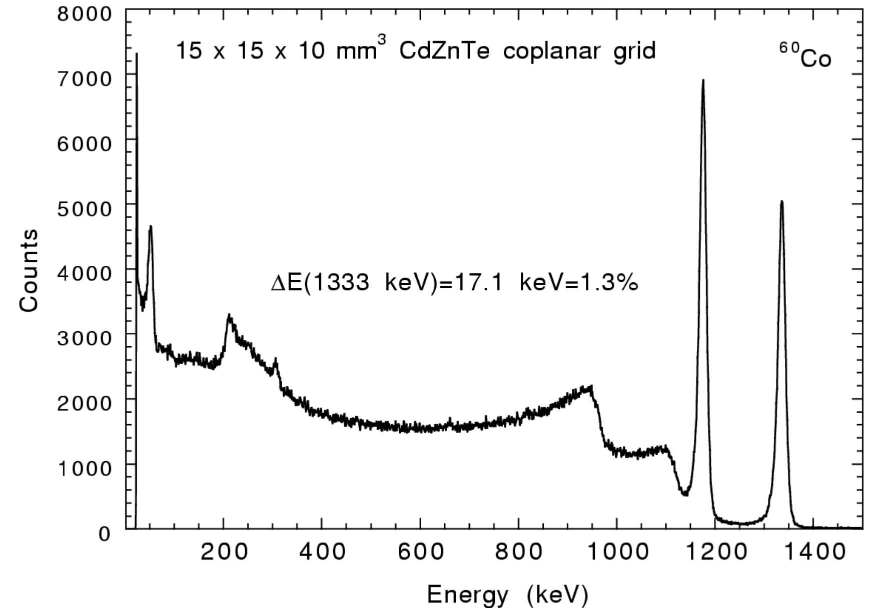

The wish list – towards the ideal detector

Summary of desirable material parameters for the development of the next generation of semiconductor detectors, in the form of a list of the minimum material and/or preferred values. Because of the uncertainty in end applications and compatibility between requirements, some of the recommendations are by necessity subjective.

Parameter	Minimum or recommended value	Reason/Comments
Composition	Binary (or pseudo binary)	To minimize stoichiometry errors.
Structure	Cubic (close packed)	To optimize density.
Density	> 5 g cm^{-3}	To ensure good stopping power.
Growth technique	Epitaxial, FZ	Allows the possibility of integrated electronic structures.
Contact barrier height	< 0.4 eV	To ensure the contacts "look" Ohmic (i.e., with a resistivity $< 10^{-3}\Omega m^2$).
Effective atomic number, Z_{eff}	> 40	For high stopping power.
Resistivity	$> 10^8\ \Omega$ cm	To allow high biases to be applied.
Hardness	> 500 kgf mm^{-2} (Knoop scale)	Chosen to be high enough to allow the use of a range of mechanical processing and bonding technologies.
Bandgap	Indirect	To limit radiative recombination.
Bandgap energy	$1.4 < \varepsilon_g < 2.2$ eV	Lower limit for room temperature operation. Upper limit imposed by mobility losses due to polar lattice scattering.
Static dielectric constant, ε (0)	< 5	To ensure low capacitance.
Ionicity	< 0.3 (Phillips scale)	Ionicity should be low to prevent problems with ionic conductivity and polarization
Majority carrier trapping centre density	$< 5 \times 10^{12}$ cm^{-3}	To ensure good charge collection.
Impurity concentration	$< 10^{15}$ cm^{-3}	Can adversely affect resistivity, mobilities and effective mass.
Mobility electrons	> 500 cm^{2}V^{-1}s^{-1}	Charge induction considerations
Mobility holes	10 or 500 cm^{2}V^{-1}s^{-1}	Lower value if single carrier sensing is used, upper value if not.
Majority carrier lifetime	$> 20\mu$s	To ensure reasonably high mu-tau products
Electron mobility-lifetime ($\mu\tau_e$)	10^{-3} cm^{2}V^{-1}	Minimum value really depends on application, X-rays or γ-rays.
Hole mobility-lifetime ($\mu\tau_h$)	$< 10^{-4}$ or 10^{-3} cm^{2}V^{-1}	($\mu\tau_h$) should be < 0.1 ($\mu\tau_e$) if single carrier sensing is employed.
Majority carrier effective mass	0.1 m_o	To ensure high speed operation.

New directions in detection techniques

- Reduced dimensionality materials

  - Quantum heterostructures
  - Radiation detection with nanosemiconductors (1-D)
  - Radiation detection based on 2-D materials

- Other degrees of freedom

  - Radiation detection based on Spintronics
  - Radiation detection based on Valleytronics

- Biological detection systems and intelligent photonics

Radiation detection with nano-semiconductors

Advantages

- Easy to manufacture
- Fabricate large detectors
- Can be grown by electrodeposition
- Better xtal perfection
- 1D conductors
- Biases can be low

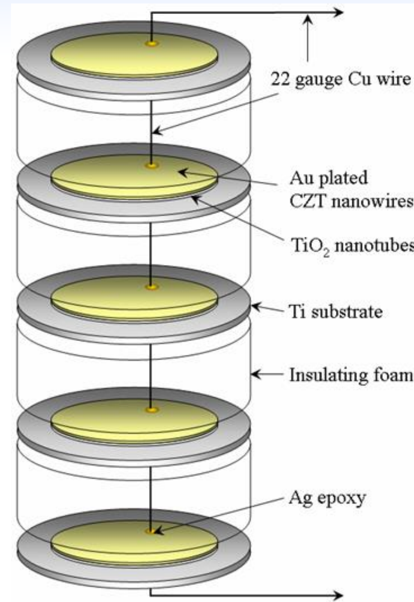

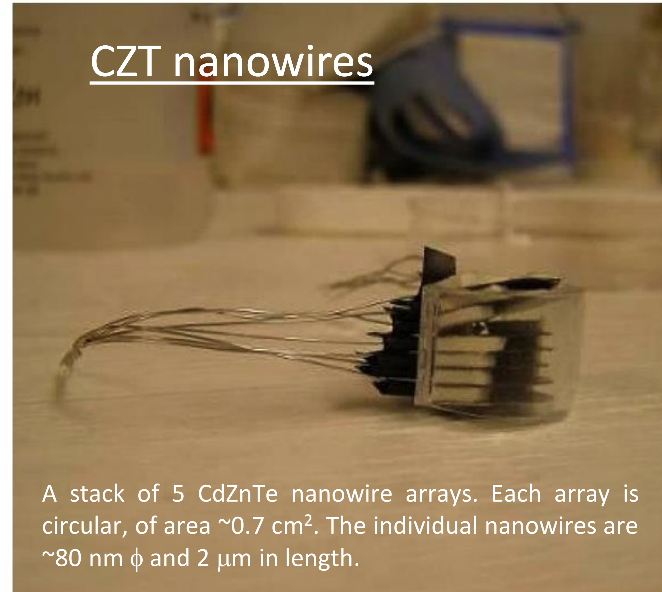

A stack of 5 CdZnTe nanowire arrays. Each array is circular, of area ~0.7 cm^2. The individual nanowires are ~80 nm ϕ and 2 μm in length.

PbSe nanocrystals

Detector 7 mmϕ x 5mm deep

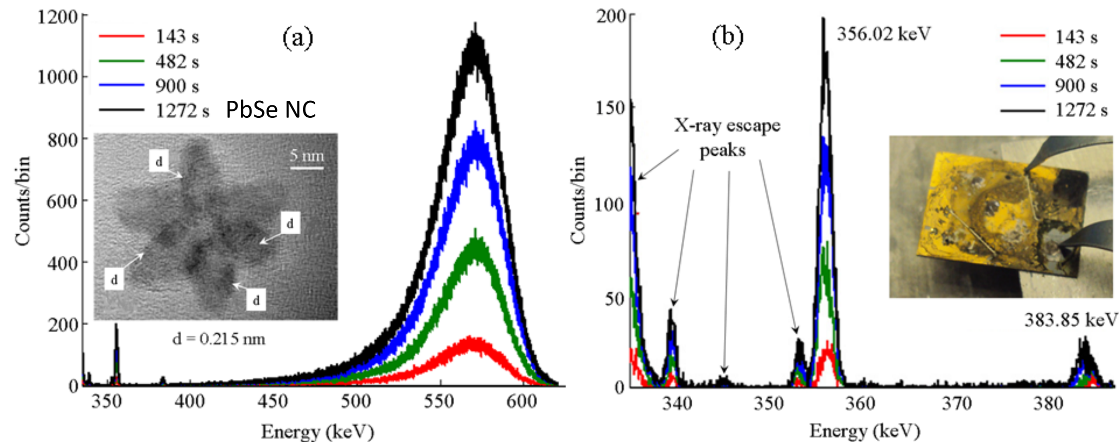

ΔE at 662 keV same as HPGe

Energy-loss spectra measured from a ^{133}Ba and ^{241}Am source. The composite α-particle and γ-ray response is shown in (a) for a 1×1 cm thin (10's of µm) assembly of a conductive polymer and star-shaped PbSe nanoparticles. (b) An expansion of the ^{133}Ba γ-ray spectrum, in which the Pb and Se X-ray escape peaks are also apparent.

Gandhi et al., Proc. SPIE, Vol. **6959** (2008) 695904.

Radiation detection based on 2-D materials

For a 3D periodic crystal structure, the energy bands appear parabolic in *E*, ***k*** space near the conduction band minimum and valance band maximum and can be approximated by the well-known dispersion relationship

$$E(\mathrm{k}) = E_{\mathrm{o}} + \frac{\hbar^2 (\mathrm{k})^2}{2m}$$

Here we see that the allowed energies of the carriers are dependent on their effective masses. However, in the 2D structure of graphene, the energy bands near the conduction band minima and valence band maxima are conical and actually touch at six points in ***k*** space and the effective mass tends to zero – the so called K points. At these points, the dispersion relationship is given by

$$E(\mathrm{k}) = \pm\ \hbar v_{\mathrm{F}} \sqrt{k_{\mathrm{x}}^2 + k_{\mathrm{y}}^2}$$

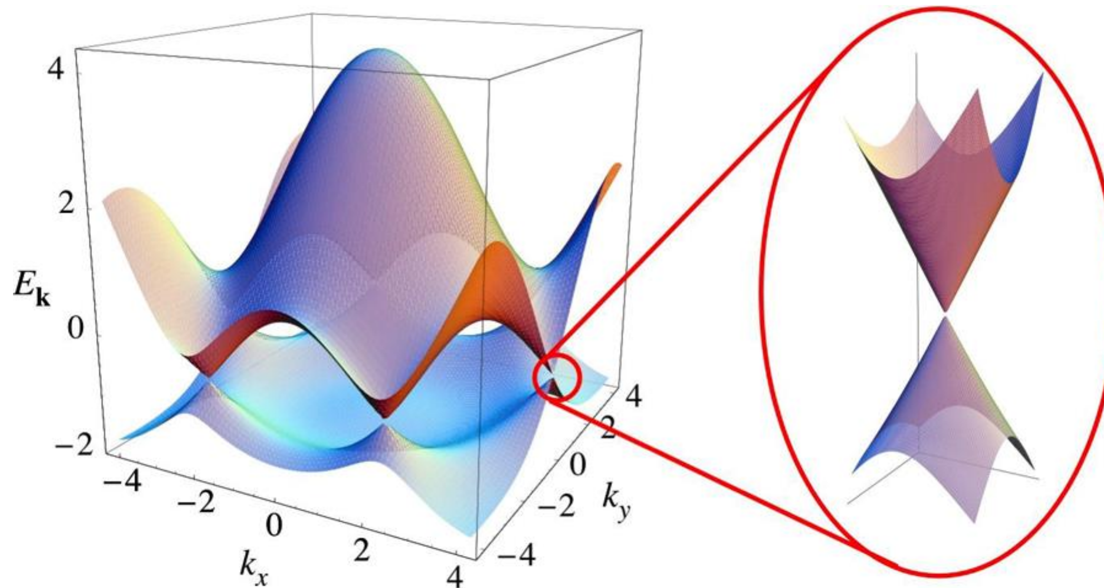

Which has no mass term. What this means is that while in standard semiconductors, the charge carriers can be described as electron waves obeying the Schrödinger effective-mass eqn., graphene electrons move according to the laws of relativistic quantum physics described by the mass-free Dirac eqn. Consequently, graphene has very high electron mobilities at room temperature, with values in excess of 15,000 $cm^2V^{-1}s^{-1}$.

Castro et. al. *Rev. Mod. Phys.*,Vol. **81** (2009) pp. 109–162

Radiation detection based on 2-D materials - graphene

A graphene FET (GFET) radiation detector - principle of operation. (a) A GFET consists of an absorber (undoped semiconductor), with an insulator buffer layer, which serves as a gate dielectric. V_g is the gate voltage applied to the sample. Current is supplied across the graphene sample, and the resistance of the graphene layer determined. In (b), incoming radiation produces ionization within the (intrinsic) semiconductor to create a conducting absorber. The gate voltage now only drops across the insulator. This results in an increased electric field, which is sensed by the graphene and its resistance changes as a result of the change in electric field as shown by the insets in the figure.

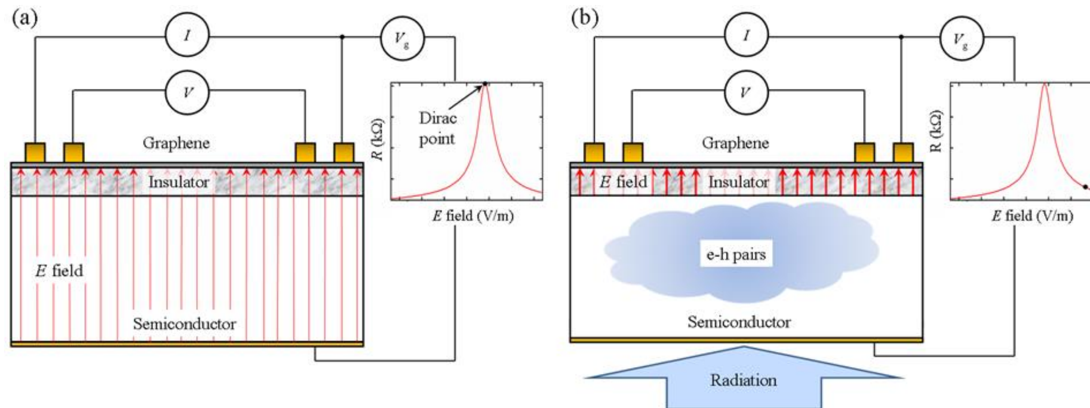

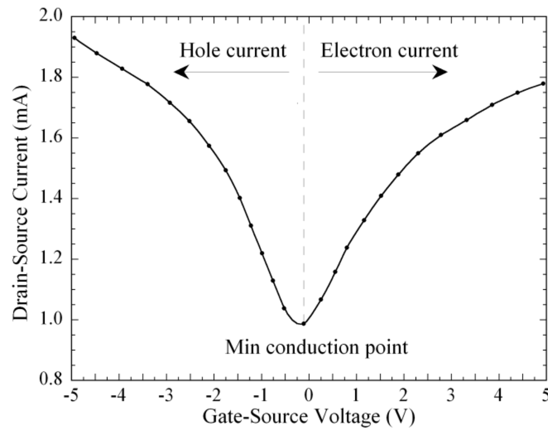

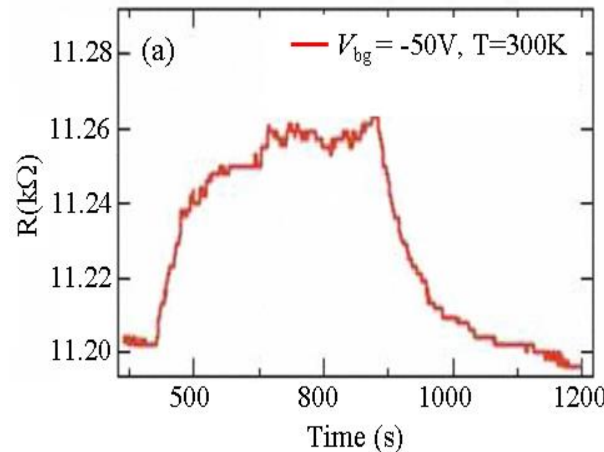

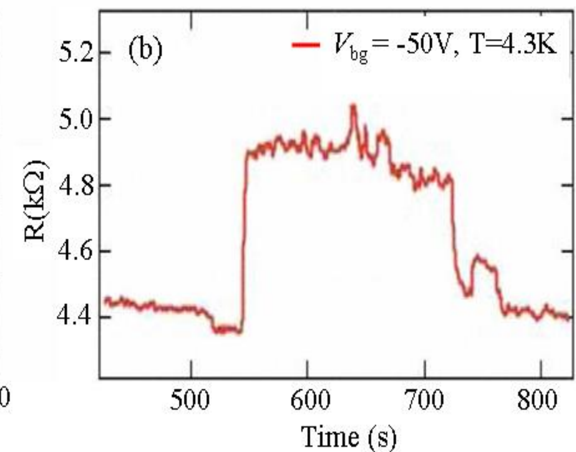

Left. GFET operation showing the variation of the drain-source current with gate source voltage using a thin p-type Si absorber. The curve reflects the Dirac curve and the device can be biased to collect either electrons or holes. (a) and (b). In (a) we show the response of a SiC based GFET to γ-rays and in (b), the response of a GaAs based GFET to X-rays. The initial rise in response corresponds to the point in time when a source is applied and the fall in response to when the radiation source is removed.

A. Patil et al., “Graphene Field Effect Transistor as Radiation Sensor”, *IEEE Nucl. Sci. Symp*. Conf. Rec., (2011) 455.

Tenent

Conventional detection systems only utilize the electrons charge

“The incremental advances in the current semiconductor nuclear detector technology will not be sufficient for developing the next generation of ultra sensitive, cost-effective detectors”

“Such developments will require the utilization of entirely new and transformative approaches”

Gary et al., IEEE Trans Nucl. Sci. conf. record, Vol. (2012) 4152-4155.

Radiation detection based on Spintronics

Conventional radiation detectors rely on a two stage process that depends on how efficiently charge carriers can be generated and how efficiently they can be separated and collected

In a Spintronic detection system the physical generation of charge carriers is not required, nor is the absorption of radiation

It only depends only on how efficiently the spin of the electrons (already present in the semiconductor) is randomised by the incoming radiation

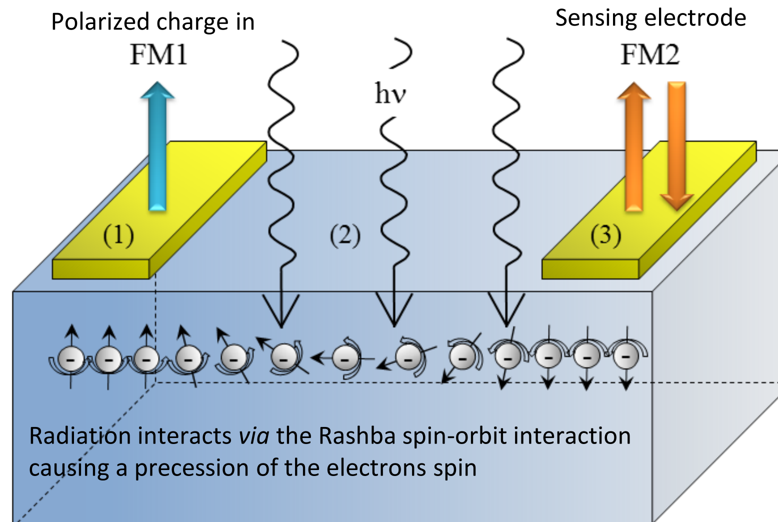

FM is a ferromagnetic metal such as Ni or Fe

Conceptual schematic of a spintronics detector, with two ferromagnetic electrodes deposited on to a semiconductor. Also depicted are the three main steps required for spintronics devices: (1) injection, (2) travel/manipulation and (3) detection. Spin is injected from a polarized source (such as a ferromagnetic metal (*e.g.*, Ni or Fe), FMl) into the active semiconductor region. The polarised electrons then interact with the incident radiation changing the spin of the electrons. The new polarization of the electron is then sensed at the other end of the semiconductor by a second ferromagnetic electrode (FM2).

New degrees of freedom

Conventional detection systems only utilize the electrons charge

Use the more obscure internal degrees of freedom of the electron, for nonvolatile information processing

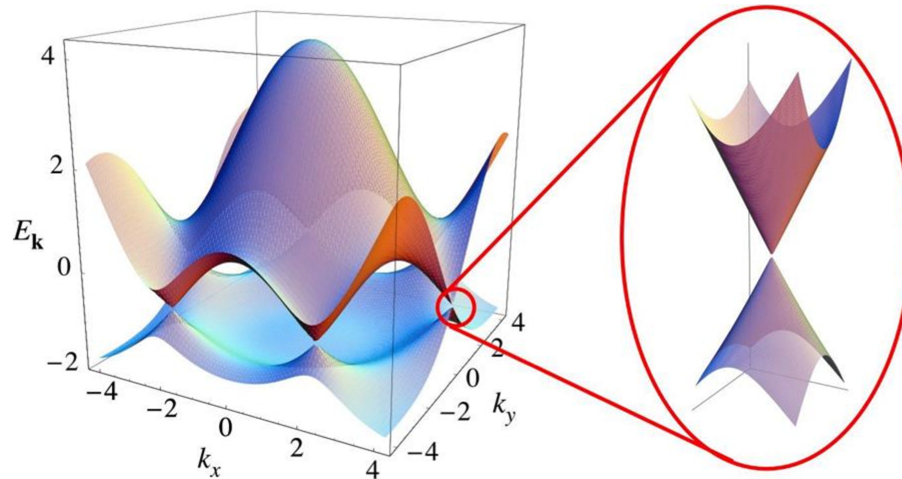

Valleytronics

Like spintronics, valley-based electronics, or valleytronics is another recent development that makes use of the more obscure internal degrees of freedom of the electron, for nonvolatile information processing. It relies on the fact that the conduction bands of some materials have two or more minima at equal energies but at different positions in momentum space. By controlling the number of electrons that occupy a particular valley, it is possible induce a valley "polarization", which can then be used to transmit/process information. This new degree of freedom behaves mathematically in a similar way to the electron spin in that it acts like additional intrinsic angular momentum of the electron. Electrons can be valley polarized by scattering off a line of defects.

[1]a contraction of "spin transport electronics"

Biological detection systems and intelligent photonics

Several recent advances in nano-technology have demonstrated the viability of bio-metallic and bio-semiconductor interfacing, leading to the possibility that future detection systems may be directly interfaced to biological systems (the operator), or alternately, biological systems may be nano-engineered to be detection systems.

* porosity in III-V compounds, particularly, GaAs, GaP and InP leads to the possibility of animal cell:semiconductor interfacing as in the case of nanostructured Si (Bayliss, et al., "The Culture of Mammalian Cells on Nanostructured Silicon", *Advanced Materials*, Vol. **11**, Issue 4 (1999) pp. 318

* The porous semiconductor serves as both the adhesion substrate for Neurons which act as transducers/receivers. Preliminary work has demonstrated that mammalian cells can be cultured on nanostructured Si that remain viable over time - both in terms of respiration and membrane integrity.

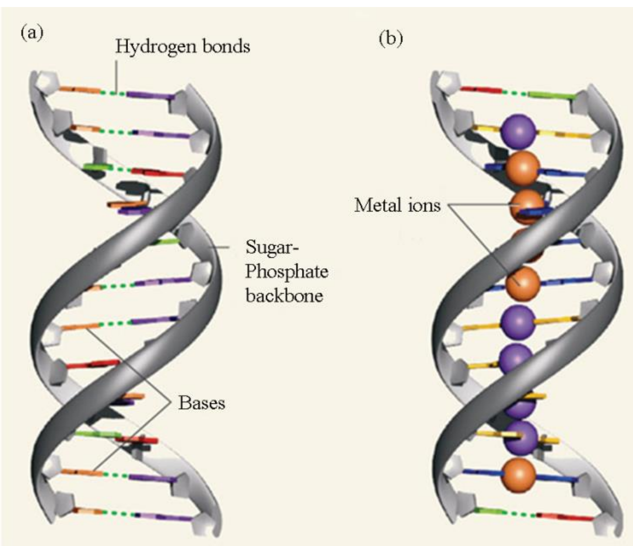

(a) Single strands of DNA consist of a sugar–phosphate backbone decorated with organic bases. A double helix forms when the bases of one strand form hydrogen bonds to complementary bases on another strand. (b), Tanaka *et al.*, *Nature Nanotech*., **1** (2006) 190, have replaced bases in natural DNA with artificial ones that bind specifically to copper ions (Cu2+, purple spheres) or mercury ions (Hg2+, orange spheres)

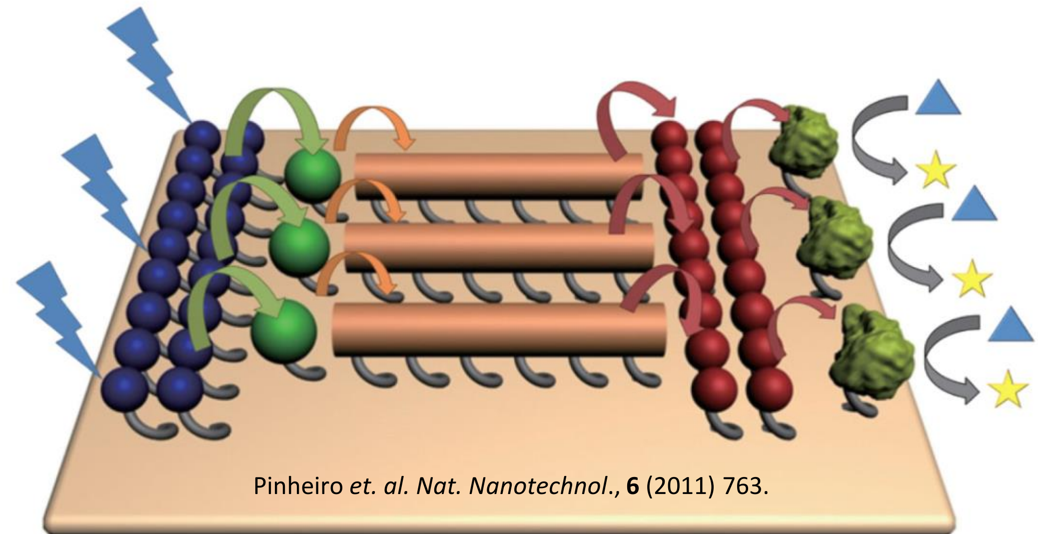

Schematic of a DNA-based machine for energy transfer and photonics. The blue, green and red spheres and orange rods represent photonic components that can serve as light-harvesting and energy-transfer materials. The uneven green spheres represent enzyme or membrane complexes that can be used as final energy or electron acceptors. These act as molecular transducer units, where light is transformed into chemical potential, represented by the transformation of substrate (triangles) or into a higher-energy product (stars).

Matczyszy, Olesiak-Banska "DNA as scaffolding for nano-photonic structures", *J. Nanophotonics*,.**6** (2012) 064505

Conclusion

Need better material – until then use single sensing techniques or explore other degrees of freedom

for more information see

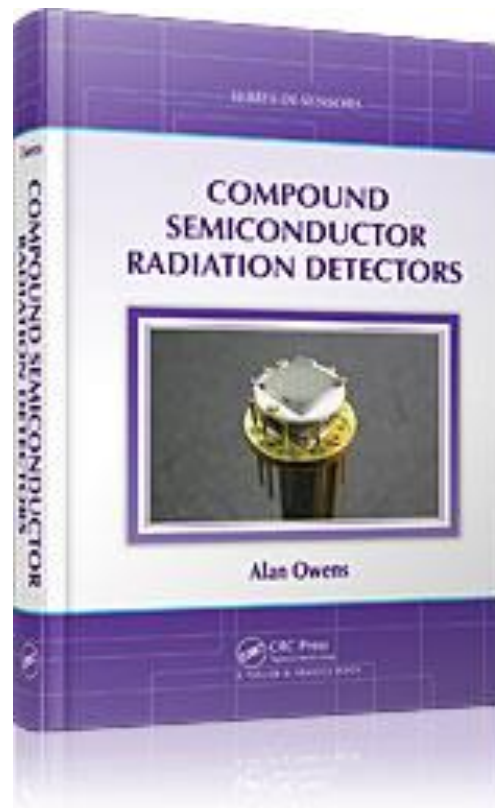

esa

Backup slides

ESA material developments over the last decade

Material	Group/Structure	Application/purpose of activity
InAs	III-V	high resolution soft X-ray imager
InSb	III-V	high resolution soft X-ray imager
GaN	III-V	free standing growth, MMICS, SSPA
GaAs	III-V	soft X-ray imager
B_4C	III-IV	solid state neutron
Ge	IV	system miniaturization
4H-SiC	IV-IV	high temp. X-ray sensor, lateral J-FET
TlBr	III-VII	hard X-ray/ γ-ray, polarization studies
CdZnTe	II-VI	hard X-ray/ γ-ray
CdMnTe	II-VI	CZT alternate
$LaCl_3:Ce^{3+}$	Hex, UCl_3 type	LaBr development vehicle
$LaBr_3:Ce^{3+}$	Hex, UCl_3 type	high resolution γ-ray spectrometer
$LaBr_3:Ce^{3+}$	Hex, UCl_3 type	theoretical studies
$CeBr_3$	Hex, UCl_3 type	low noise γ-ray spectrometer
$SrI_2:Eu^{2+}$	Ortho, oP24	high resolution, low noise γ-ray

Semiconductor crystal structures at the macroscopic level

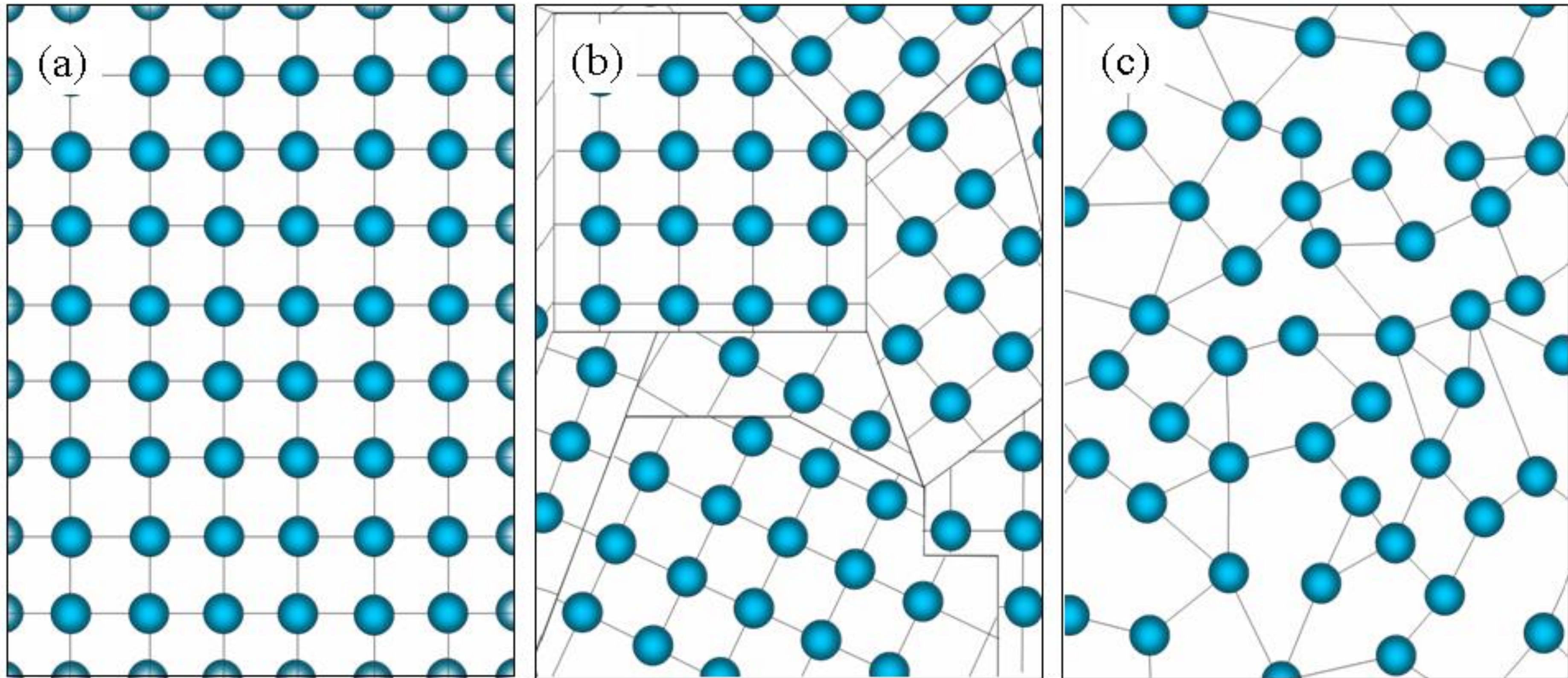

While the majority of semiconductors solidify into regular periodic patterns shown in (a), they can also form polycrystals, shown in (b) that is, a collection of individual grains of crystalline material separated by grain boundaries or (c) amorphous solid solutions in which there is little long range order.

Ternary compounds - phase diagram II-VI materials

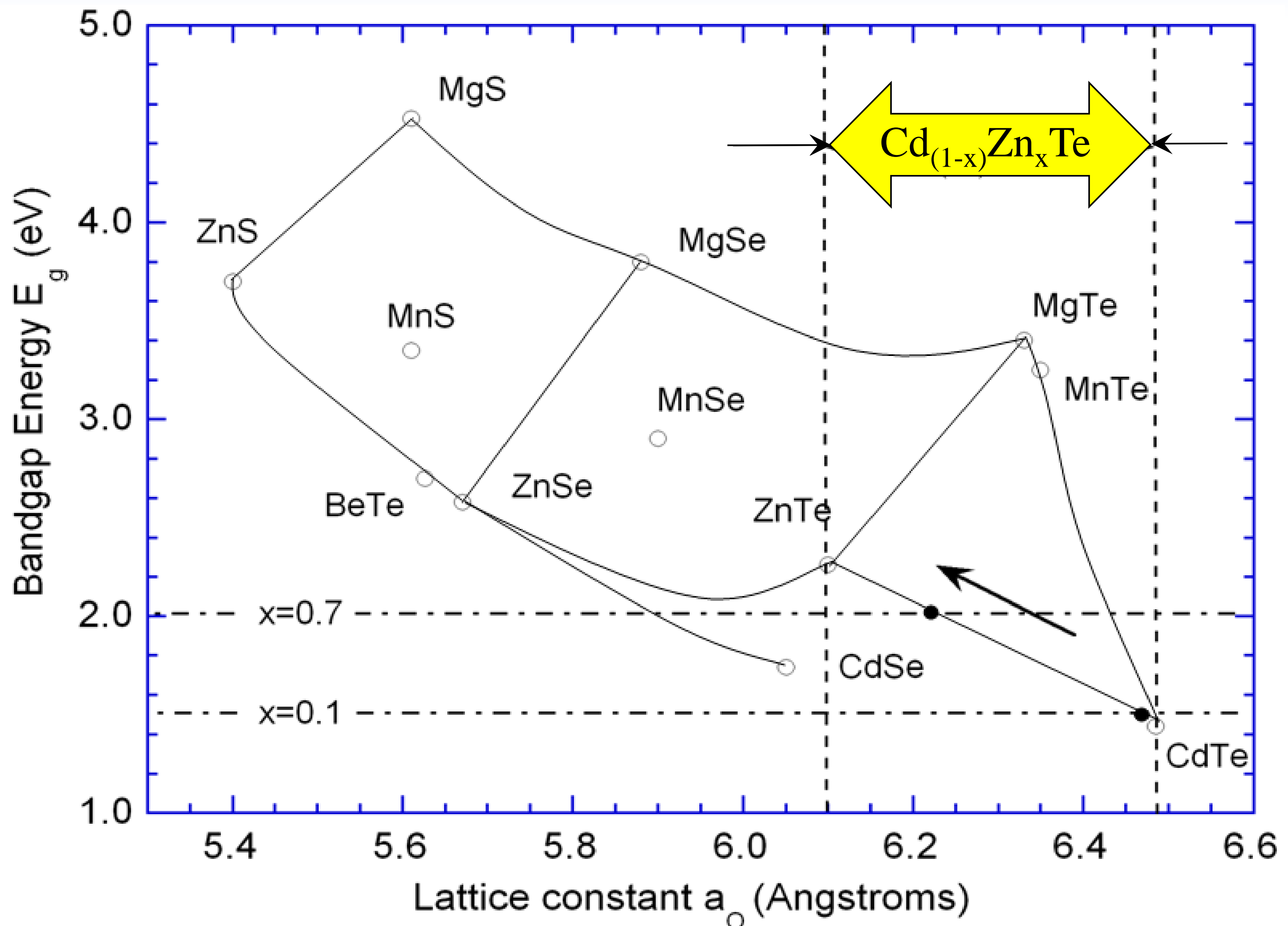

x=0.1 - E_g optimized for operation at ~-30°C; x=0.7 – E_g optimized for room temp. operation

Charge particle energy loss in materials

The quantity dE/dx is often referred to as the stopping power of the material. To a first approximation, energy loss in a material is simply characterized by Z/A.

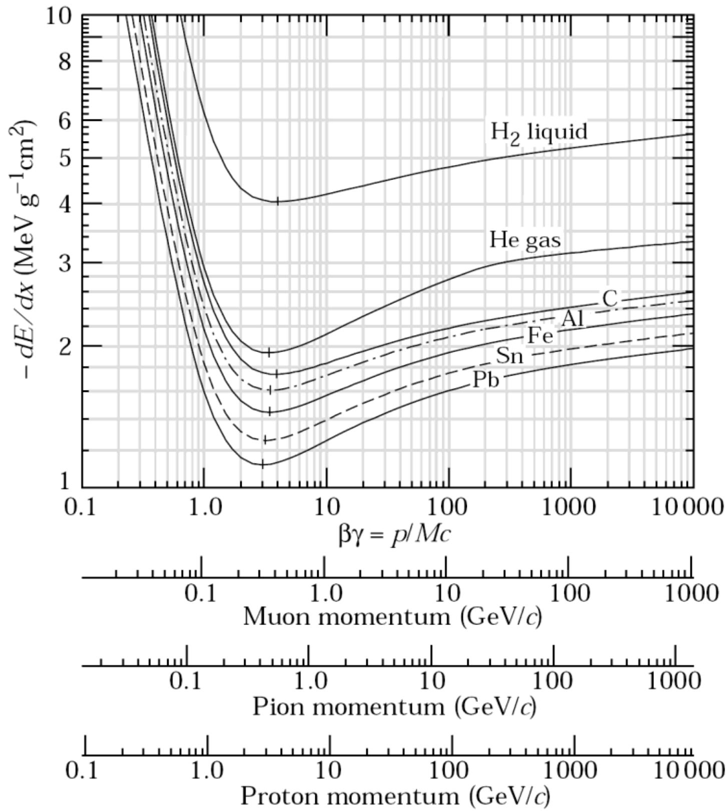

Min occurs near $\gamma \sim 3 \sim 0.02\ z^2$ $\Rightarrow$ MIPS

~2 MeV g^{-1}cm^{-2} light materials & ~1 MeV g^{-1}cm^{2} for heavy materials

The mean energy loss of a charged particle (dE/dx) per unit path length (in MeV g^{-1} cm^{2}) for a range of materials, as derived from the Bethe-Bloch formula.

$$-\left(\frac{dE}{dx}\right) = \frac{4\pi e^4 z^2}{m_o v^2} NZ \left[\ln \frac{2m_o v^2}{I} - \ln\left(1-\beta^2\right) - \beta^2 \right] \quad \text{ergs cm}^{-1}$$

ill-defined experimentally and not useful for describing energy loss by single particles – utility lies in dosimetry, where only bulk deposit is of relevance.

A real detector (limited granularity) cannot measure dE/dx - we measure the energy ΔE deposited in layers of finite thickness Δx

- Repeated measurements sampling from an energy loss distribution.
- For thin absorbers dE/dx is broader than expected showing large fluctuations towards high losses, so called Landau tails.

$$\frac{df}{dx}(x,\Delta) = \int_0^\infty w(E)\left[f(x,\Delta - E) - f(x,\Delta)\right] dE$$

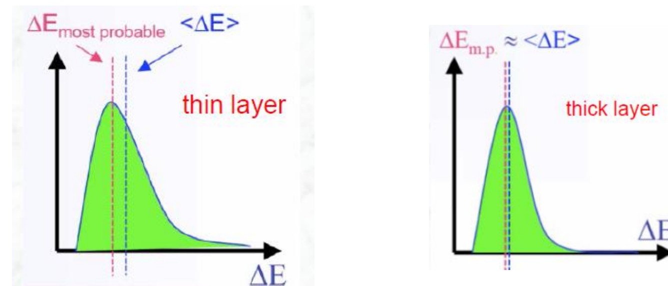

Example: Silicon sensor, 300 µm thick, ΔE_{mip} ~82 keV, ,$<\Delta E>_{landau}$~115 keV

For thick layers and high density materials, the energy loss distribution shows a more Gaussian-like distribution (many collisions - central limit theorem)

Energy loss of secondary electrons – collisional and bremsstrahlung

For electrons, the Bethe-Bloch Eq. needs modified to include radiative losses from Bremsstrahlung as well as small mass collisional losses. Interactions now dominated by elastic collisions with electrons.

$$-\left(\frac{dE}{dx}\right)_{\mathrm{c}} = \frac{2\pi e^4 z^2}{m_o v^2} NZ \left[\ln \frac{2m_o v^2}{2I^2(1-\beta^2)} - (\ln 2)\left(2\sqrt{1-\beta^2} - 1 + \beta^2\right) + \left(1-\beta^2\right) + \frac{1}{8}\left(1-\sqrt{1-\beta^2}\right)^2 \right]^2$$

Radiative losses occur because the electron is constantly scattered and therefore deflected along its trajectory. The deflections cause acceleration and therefore the electron will radiate electromagnetically from any position along the electron trajectory. The energy loss per unit path length in this case is given by

$$-\left(\frac{dE}{dx}\right)_{\mathrm{r}} = \frac{NEZ(Z+1)e^4}{137 m_o^2 c^4} \left[4\ln \frac{2E}{m_o c^2} - \frac{4}{3} \right]$$

These losses are most important for high energies and heavy absorbers. The total electron energy loss is therefore the sum of the collisional and radiative losses

$$\left(\frac{dE}{dx}\right)_{\mathrm{T}} = \left(\frac{dE}{dx}\right)_{\mathrm{c}} + \left(\frac{dE}{dx}\right)_{\mathrm{r}}$$

We can assess the relative importance of these two loss mechanisms in a detector by examining the ratio of the two.

$$\frac{(dE/dx)_r}{(dE/dx)_c} \approx \frac{EZ}{700}$$

For compound semiconductor detectors $(dE/dx)_{coll} > 20\ (dE/dx)_{rad}$

Photon interaction mechanisms

Photoelectric

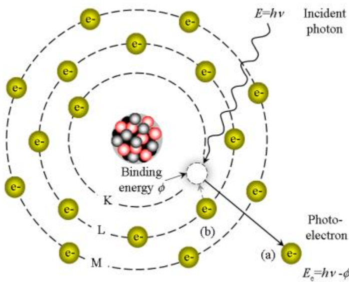

$E_e = h\upsilon - \phi$

$${}_a\tau_K = \sigma_T Z^5 \alpha^4 2^{5/2} \left(\frac{m_o c^2}{E_\gamma} \right)^{7/2}$$ cm² /atom

Coherent and incoherent scattering

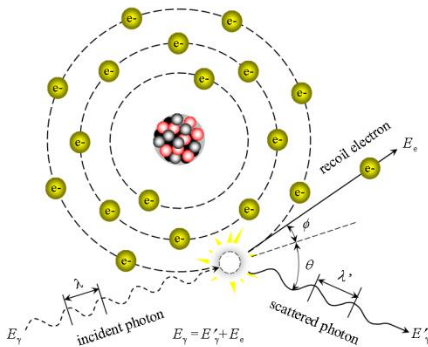

$h\upsilon' = h\upsilon$

$${}_a\sigma_{coh} = const \left(\frac{z}{E_\gamma} \right)^2$$ cm² /atom

$$E_\gamma' = h\upsilon' = \frac{E_\gamma}{1 + (E_\gamma / m_o c^2)(1 - \cos\theta)}$$

$$\sigma_{incoh} = const \left(\frac{Z}{A} \right) \rho \frac{1}{E_\gamma}$$ cm² /atom

Pair production

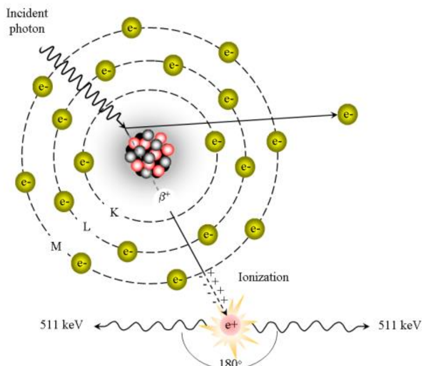

$E_\gamma = (E_- + m_o c^2) + (E_+ + m_o c^2)$

$$\kappa_p = \frac{r_o^2 Z^2}{137} \left[\frac{28 \ln}{9} \left(\frac{2E_\gamma}{m_o c^2} \right) - \frac{218}{27} \right]$$ cm² /atom

$\mu_o = \tau + \sigma_{incoh} + \sigma_{coh} + \kappa$ cm² /atom

μ_o = linear attenuation coefficient

Attenuation and absorption of electromagnetic radiation

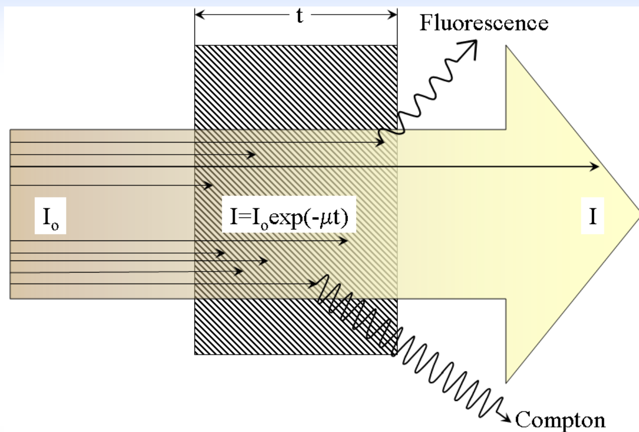

$$dI = -\mu_o I dx$$

$$\mu_o = \tau + \sigma_{incoh} + \sigma_{coh} + \kappa \quad \text{cm}^2\text{/atom}$$

$$I = I_o \exp(-\mu_o x)$$

For compounds $\left(\frac{\mu}{\rho}\right) = \sum_i w_i \left(\frac{\mu_o}{\rho}\right)$ cm^{-1} μ/ρ =mass attenuation coefficient